Derivation of Electron Charge Misidentification Scale Factors with Run 2 and Run 3 Data at the ATLAS Experiment

by:

Damandeep KAUR
Bachelor of Science, CARLETON UNIVERSITY, 2022

A Thesis Submitted in Partial Fulfillment of the
Requirements for the Degree of

MASTER OF SCIENCE

in the Department of Physics and Astronomy

We acknowledge and respect the Lək̓ʷəŋən (Songhees and Xʷsepsəm/Esquimalt) Peoples on whose territory the university stands, and the Lək̓ʷəŋən and W̱SÁNEĆ Peoples whose historical relationships with the land continue to this day.

Derivation of Electron Charge Misidentification Scale Factors with Run 2 and Run 3 Data at the ATLAS Experiment

by:

Damandeep KAUR
Bachelor of Science, CARLETON UNIVERSITY, 2022

SUPERVISORY COMMITTEE

Dr. JUSTIN ALBERT, Supervisor
Department of Physics and Astronomy

Dr. HEATHER RUSSELL, Departmental Member
Department of Physics and Astronomy

Dr. KATHERINE PACHAL, Outside Member
Research Scientist, TRIUMF

ABSTRACT

Electron charge misidentification constitutes a significant background in analyses involving same-sign electron pairs, such as searches for electroweak production of same-sign $W^{\pm}W^{\pm}$ bosons. An estimation of this background is essential for improving signal sensitivity in such processes. This thesis presents the derivation of charge misidentification scale factors using a Deep Neural Network (DNN) based electron identification (ID) in the ATLAS experiment, utilizing proton–proton collision data produced at $\sqrt{s} = 13\,\text{TeV}$ and $\sqrt{s} = 13.6\,\text{TeV}$. A data-driven method based on the $Z \to e^{+}e^{-}$ process is employed to estimate charge flip probabilities in data and Monte Carlo simulation, across different kinematic bins of transverse momentum and pseudorapidity. The DNN-based ID algorithm offers improved discrimination power compared to traditional likelihood-based methods, particularly in complex detector regions. The derived scale factors correct for mismodelling of charge flip rates in Monte Carlo simulations and are parametrized in both one-dimensional and two-dimensional schemes. Closure tests are performed to validate the robustness of the scale factors and their applicability across various physics analyses.

TABLE OF CONTENTS

List of Tables

List of Figures

ACKNOWLEDGEMENTS

I would like to express my deepest gratitude to everyone who has supported me throughout the course of my academic journey. Firstly, I would like to sincerely thank my supervisor, **Dr. Justin Albert**, for his unwavering support and guidance throughout the course of my thesis. I truly appreciate the time and effort you invested in providing insightful feedback and encouraging my academic development. I would also like to thank my supervisory committee member **Dr. Heather Russell**. Your mentorship has been invaluable in shaping my growth as a physicist. I am deeply grateful for the opportunity to learn from your experience, insight, and dedication to research. Your encouragement and thoughtful feedback have consistently motivated me to think critically and work independently.

I would also like to thank **Dr. John McGowan** for your continuous support throughout my work on the analysis. Your technical expertise, patience, and willingness to help troubleshoot problems whether related to code, software frameworks, or data processing were instrumental in keeping my research moving forward. I am especially grateful for your prompt guidance during critical stages of the analysis, and for the clarity and generosity with which you shared your knowledge. My work would not have progressed as smoothly without your contributions.

I want to extend my thanks to *ssWW* analysis team members and Electron ID team members. I would also like to thank my team members and friends, **Adrienne Scott** and **Mitch Kelly**, for your collaboration, encouragement, and many insightful discussions throughout the research.

Finally, I would like to thank my family for giving me all the love and support I could ever ask for. To my husband, **Gurkirat**, your unwavering encouragement, patience, and belief in me have been my foundation throughout this journey. I am deeply grateful for everything you have done to help me reach this point.

DEDICATION

To my mother and my husband, for your unconditional love, constant support and for always believing in me even when I doubted myself.

CHAPTER 1

Introduction

The primary goal of elementary particle physics is to understand the fundamental building blocks of matter and the forces governing their interactions. This understanding is encapsulated in the Standard Model (SM), a theoretical framework that has achieved remarkable success in explaining a wide range of experimental results. However, the SM remains incomplete, as it fails to account for key phenomena such as the existence of dark matter and the unification of the fundamental forces. Therefore, any viable extension must reproduce the SM as its low-energy limit, while providing explanations for phenomena such as dark matter and dark energy. Among the proposed extensions, Supersymmetry (SUSY) stands out as a promising candidate. It introduces a symmetry between bosons and fermions, predicting the existence of a superpartner for each SM particle. Since none of these superpartners have yet been observed, SUSY must be broken in nature, implying that superpartners are significantly heavier than their SM counterparts. One of the main goals of the ATLAS detector at the CERN Large Hadron Collider (LHC) is to search for evidence of supersymmetric particles in accordance with predictions of supersymmetric models.

Another important process to study in ATLAS is the mechanism of electroweak symmetry breaking, through which three of the four electroweak force carriers ($W^{\pm}$ and Z bosons) acquire mass via their interaction with the Higgs field. Vector boson scattering (VBS) is a key process within the Standard Model for probing the electroweak symmetry breaking mechanism. It involves the scattering of two gauge bosons and provides direct sensitivity to the dynamics that give mass to the $W^{\pm}$ and Z bosons via the Higgs field. At the LHC, final states with two vector bosons and two associated jets can arise from both strong and electroweak interactions. Among these, the electroweak production mode is particularly significant, as it includes contributions from VBS processes.

In some physics processes, the precise determination of the lepton charge is not critical; simply identifying the presence of a lepton is sufficient to characterize the decay. However, for other processes, accurate charge identification becomes a powerful tool for distinguishing signal from background. A notable example is in searches for supersymmetric particles that decay into final states containing two same-sign leptons. Another example is a VBS process such as the production of two W bosons with identical electric charge in association with two jets. Due to the presence of same-sign leptons originating from leptonic W-decays, it is possible to misreconstruct one of these leptons with the

wrong charge, which leads to charge misidentification and contaminating the same-sign signal region. However, the reverse situation is not a concern in opposite-sign analyses. True same-sign events are already rare in the SM, and even if a charge misidentification occurs, it would convert a same-sign pair into an opposite-sign one, effectively blending it into a large opposite-sign background. Since the rate of real same-sign events is negligible compared to opposite-sign production, and the charge misidentification probability is itself small, the resulting contamination in opposite-sign regions is statistically insignificant.

Because muons have two independent charge measurements due to the inner detector and the muon spectrometer, charge misidentification is negligible for muons and this thesis focuses exclusively on the study of charge misidentification in electrons. Therefore, electron charge misidentification refers to the incorrect reconstruction of an electron's electric charge during the detector's track reconstruction process. Electrons reconstructed with the wrong charge are referred to as charge-flip electrons. This typically occurs when the electron undergoes bremsstrahlung in the detector material, causing the original track to be poorly measured or replaced with a track from a secondary particle. The main sources of charge-flip electrons are $Z \rightarrow e^+e^- + jets$ and $t\bar{t}$ processes. However, in this thesis, only $Z \rightarrow e^+e^-$ events are used for the study of electron charge misidentification providing a clean signal with a well-defined invariant mass peak of Z boson at around 91 GeV. This allows for very efficient background suppression, making it easy to isolate true opposite-sign pairs. On the other hand, $t\bar{t} \rightarrow (W^+b)(W^-\bar{b}) \rightarrow e^+\nu b + e^-\bar{\nu}\bar{b}$ includes final state with two electrons, two b-jets and two neutrinos which makes it harder to isolate the clean opposite-sign electron pair. Also, without the known invariant mass like Z boson, it is hard to tell if the electron pair was really opposite-sign at truth level. Charge flip electron is the most prominent background for many physics analyses such as in searches of same-sign WW production but this background cannot be removed through event selection alone, and its accurate modeling is essential. While Monte Carlo (MC) simulations provide estimates of the charge flip probability, they often suffer from mismodeling of material interactions, detector resolution, and tracking performance. Therefore, data-driven corrections in the form of charge flip scale factors, which are defined as the ratio of charge flip rates in data to those in simulation, must be applied to simulated events to improve the background estimation.

The primary objective of this thesis is to derive electron charge misidentification scale factors using $Z \rightarrow e^+e^-$ events in the A Toroidal LHC ApparatuS (ATLAS) detector with Run 2 and Run 3 data. The analysis is performed for three electron identification working points: Loose, Medium, and Tight. This provides a comprehensive understanding of charge flip behavior across different selection criteria. In addition to the scale factors, the charge flip rates themselves are also extracted directly from data and simulation. To improve the rejection of charge flip electrons in analyses sensitive to same-sign final states, two complementary methods are employed: a traditional likelihood-based identification combined with the Electron Charge ID Selector (ECIDS) tool, and a newer approach using Deep Neural Network (DNN) identification with additional charge flip rejection. The resulting scale factors are derived using both one-dimensional (1D) and two-dimensional (2D) parameterizations to capture potential correlations between kinematic variables and misidentification rates. Chapter 2 provides an overview of the SM and its theoretical foundation, along with the phenomenology of production of

$Z \to e^+e^-$ in proton–proton collisions. Chapter 3 describes the ATLAS detector setup at the LHC. Chapter 4 describes the datasets used in the analysis, along with the MC simulated event samples employed for comparison with data. Chapter 5 details the reconstruction, identification, isolation, and selection criteria for electron objects, along with other relevant physics objects and trigger requirements used in the analysis. Chapter 6 introduces the concept of electron charge misidentification, outlines its primary sources, and describes the relevant truth-level classification used to study charge flip electrons. Chapter 7 presents the methodology for measuring electron charge misidentification rates and deriving corresponding scale factors, including sideband subtraction, final-state radiation correction, and different parameterizations of the charge flip probability. Chapter 8 presents the results of the charge flip scale factor measurements using various identification and rejection methods, discusses the non-stability of 2D parameterizations, and includes closure tests to validate the methodology. Chapter 9 discusses the suppression of electron charge misidentification and the implications of electron selection criteria in physics analyses. Chapter 10 concludes the thesis by summarizing the results of charge flip scale factors.

CHAPTER 2

Theoretical Background

This chapter provides an overview of the theoretical framework underlying the analysis presented in this thesis. It begins with a summary of the Standard Model (SM) of particle physics, outlining the fundamental interactions and the gauge theories that describe them, including Quantum Electrodynamics (QED), Quantum Chromodynamics (QCD), and the electroweak theory. The mechanism of electroweak symmetry breaking and the role of the Higgs boson are also discussed. Finally, the production of $Z \to e^+e^-$ in proton–proton collisions is reviewed, as it forms the primary process used in the derivation of charge misidentification scale factors.

2.1 The Standard Model

The SM of particle physics is a well-established theoretical framework that describes the fundamental particles and their interactions, excluding gravity. It is a quantum field theory built on the principles of special relativity, gauge invariance, and renormalizability. In the SM, interactions are governed by local gauge invariance and the symmetries of gauge invariance are organized using group theory [1]:

$$SU(3)_C \otimes SU(2)_L \otimes U(1)_Y, \tag{2.1}$$

where each of the three groups roughly correspond to the three fundamental interactions described by the SM: strong, weak, and electromagnetic interactions, respectively. However, gravity remains outside the scope of the SM. Each gauge symmetry is associated with a conserved charge and quantum fields carrying these charges interact accordingly. These fields are categorized by their spin: fermionic fields have half-integer spins (e.g., $1/2, 3/2, ..$), while bosonic fields have integer spins (e.g., 0, 1,..). The SM includes three generations of fermions, each consisting of six quarks and six leptons (along with their antiparticles), distinguished by whether or not they are charged under the strong interaction's $SU(3)_C$ symmetry. While all generations share the same quantum numbers, they differ in mass. An overview of these fundamental particles and the force-mediating bosons is shown in Figure 2.1

The strong interaction, described in the SM by QCD, is governed by the non-Abelian gauge group $SU(3)_C$. It is mediated by eight gluons, which interact with particles carrying colour charge, namely

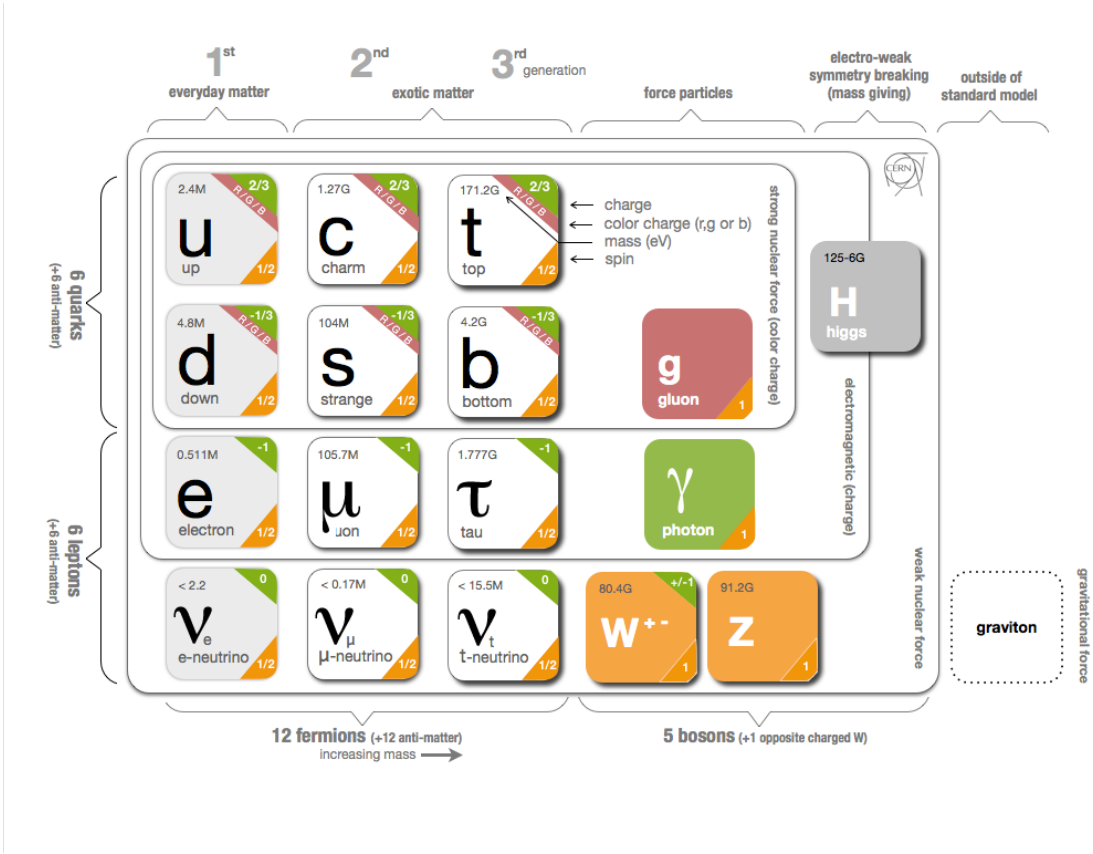

Figure 2.1: Standard Model of Particle Physics. Figure is taken from Ref. [2].

quarks and gluons. Colour charge exists in three types, denoted as red, green, blue, and their corresponding anticolours. Due to the phenomenon of colour confinement, only colour neutral combinations of quarks have been observed experimentally. These manifest as mesons (quark–antiquark pairs) and baryons (three-quark or three-antiquark states), where the net colour is zero. A distinctive feature of the strong interaction is asymptotic freedom, wherein the interaction strength decreases at high energies, allowing quarks and gluons to behave nearly freely. This property enables accurate predictions via perturbative QCD in high-energy regimes.

The SM is formulated using the framework of Quantum Field Theory (QFT), where particles are not seen as point-like objects but rather as excitations of underlying quantum fields that exist at every point in spacetime. Mathematically, the full structure of the SM is encoded in the Lagrangian in the equation 2.2 as a gauge-invariant quantum field theory [3, 4]:

$$\mathcal{L} = -\frac{1}{4}F_{\mu\nu}F^{\mu\nu} + i\bar{\psi}D\psi + \text{h.c.} + \bar{\psi}_i y_{ij}\psi_j\phi + \text{h.c.} + |D_\mu\phi|^2 - V(\phi), \tag{2.2}$$

where the first term, $-\frac{1}{4}F_{\mu\nu}F^{\mu\nu}$, represents the dynamics of the gauge fields and encapsulates the interactions of electromagnetic, weak and strong fundamental forces. The second term, $i\bar{\psi}D\psi + \text{h.c.}$,

describes fermions and their coupling to the Higgs field, enabling matter–force interactions. The third term, $\bar{\psi}_i y_{ij} \psi_j \phi + \text{h.c.}$, is known as the Yukawa interaction [5], couples fermions to the Higgs field, and is responsible for generating fermion masses. The last term, $|D_\mu \phi|^2 - V(\phi)$, governs the Higgs field itself, whose self-interactions and spontaneous symmetry breaking mechanism are necessarily associated with the mass generation of W and Z bosons.

2.1.1 *Overview of Fundamental Interactions*

Nature is governed by four fundamental interactions: gravitational, electromagnetic, weak, and strong forces. Of these, the Standard Model of particle physics incorporates the electromagnetic, weak, and strong interactions, while gravity is not included due to the lack of an experimentally-tested quantum theory of gravitation.

The electromagnetic force acts between electrically-charged particles and is mediated by the photon. It has an infinite range and is well-described by **QED**, a gauge theory based on the $U(1)_Y$ symmetry group. The **weak interaction** is responsible for processes such as beta decay and neutrino interactions. It is mediated by the massive $W^\pm$ and Z^0 bosons, and is short-ranged due to the non-zero masses of these mediators. Together with electromagnetism, it is unified in the **electroweak theory**, governed by the $SU(2)_L \otimes U(1)_Y$ gauge group. The strong interaction binds quarks together inside hadrons and is mediated by gluons. It is described by **QCD**, a gauge theory with an $SU(3)_C$ symmetry. Unlike other forces, the strong interaction exhibits asymptotic freedom at short distances and confinement at long ranges, preventing the isolation of individual quarks.

2.1.2 *Gauge Theory and Quantum Electrodynamics*

Quantum Electrodynamics is the QFT that describes electromagnetic interactions among fundamental particles in the SM. It successfully combines quantum mechanics with special relativity to provide extremely accurate predictions of electromagnetic processes across a wide range of energy scales. In QFT, particles are represented as quantum fields extending throughout spacetime. Their dynamics and interactions are governed by a Lagrangian density, which encodes the full behavior of a system. This approach, which forms the theoretical foundation of all interactions in the SM, is applied here to the electromagnetic case. To describe a freely propagating spin-$\frac{1}{2}$ fermion (such as an electron), we start with the Dirac Lagrangian [3]:

$$\mathcal{L}_{\text{Dirac}} = \bar{\psi}(i\gamma^\mu \partial_\mu - m)\psi, \tag{2.3}$$

where ψ is the fermion field, $\bar{\psi} = \psi^\dagger \gamma^0$ is its Dirac adjoint, γ^μ are the Dirac matrices, and m is the fermion mass. This Lagrangian is invariant under global $U(1)$ transformations, i.e., transformations where the fermion field is multiplied by a constant phase factor:

$$\psi \to e^{i\alpha}\psi, \tag{2.4}$$

with $\alpha \in \mathbb{R}$. However, to incorporate the principles of gauge symmetry and to match classical electrodynamics, we extend this symmetry to a local $U(1)$ gauge invariance, where the phase factor becomes a function of spacetime:

$$\psi(x) \to e^{i\alpha(x)}\psi(x). \tag{2.5}$$

This transformation introduces additional terms in the derivative operator when applied to the fermion field, breaking the invariance of the original Lagrangian. To restore local gauge invariance, we introduce a gauge field A_μ, interpreted as the electromagnetic four-potential. We define a covariant derivative:

$$D_\mu = \partial_\mu + iQA_\mu, \tag{2.6}$$

where Q is the electric charge of the fermion. For the theory to remain invariant under the local transformation, the gauge field must also transform as:

$$A_\mu \to A'_\mu = A_\mu + \partial_\mu \alpha(x). \tag{2.7}$$

This procedure introduces a new interaction term between the fermion and the gauge field: $Q\,\bar{\psi}\gamma^\mu A_\mu \psi$. This term describes the electromagnetic coupling of the fermion to the photon field. The gauge field itself must also have dynamics, which are encoded in the kinetic term built from the electromagnetic field strength tensor:

$$F_{\mu\nu} = \partial_\mu A_\nu - \partial_\nu A_\mu. \tag{2.8}$$

The kinetic term for the photon field is:

$$\mathcal{L}_{\text{kin}} = -\frac{1}{4} F_{\mu\nu}F^{\mu\nu}. \tag{2.9}$$

Putting all components together, the full QED Lagrangian becomes:

$$\mathcal{L}_{\text{QED}} = \bar{\psi}(i\gamma^\mu \partial_\mu - m)\psi + Q\,\bar{\psi}\gamma^\mu A_\mu \psi - \frac{1}{4} F_{\mu\nu}F^{\mu\nu}. \tag{2.10}$$

This Lagrangian describes a massive spin-½ fermion interacting with a massless spin-1 gauge boson (the photon). The equations of motion derived from this Lagrangian reproduce the Dirac equation for fermions and the Maxwell equations for electromagnetic fields, thus providing a quantum field theoretical formulation of classical electrodynamics. In particular, the equation:

$$\partial_\mu F^{\mu\nu} = j^\nu, \tag{2.11}$$

is the Maxwell's equations, describing how the electromagnetic field responds to the presence of a current j^ν, which arises from the motion of charged fermions and is defined as $j^\mu = Q\,\bar{\psi}\gamma^\mu\psi$. Meanwhile, the modified Dirac equation:

$$(i\gamma^\mu \partial_\mu - m)\psi = Q\gamma^\mu A_\mu \psi, \tag{2.12}$$

includes the coupling between the fermion and the electromagnetic potential. This shows how the Dirac spinor field interacts with the electromagnetic gauge field, allowing the exchange of a photon. This photon exchange is what mediates the electromagnetic force between charged particles in QED.

2.1.3 *Quantum Chromodynamics*

The strong interaction, which binds quarks together inside hadrons, is described in the SM by QCD—a QFT founded on the principle of local gauge invariance under the non-Abelian gauge group $SU(3)_C$ [6], where "$_C$" denotes colour charge. Quarks, which carry colour charge, come in three types of colour: red, green, and blue. The dynamics of non-interacting (free) quark colour fields are described by a Lagrangian analogous to the Dirac Lagrangian:

$$\mathcal{L}_{\text{Dirac},C} = \sum_{j=1}^{3} \bar{q}_j (i\gamma^\mu \partial_\mu - m) q_j, \tag{2.13}$$

where q_j denotes the quark field of colour j, and the sum runs over the three colour states. To incorporate interactions, QCD requires local gauge invariance under $SU(3)_C$, implemented through the transformation:

$$q_j \rightarrow e^{i\alpha(x)\cdot \mathbf{T}} q_{j'}, \tag{2.14}$$

where $\alpha(x)$ is a set of eight real-valued functions of spacetime, and $\mathbf{T} = T^a$ (with a = 1,2,...8) are the generators of the $SU(3)$ group. $SU(3)$ group is non-abelian because the generators do not commute ($[T^a, T^b] \neq 0$). To maintain gauge invariance, eight massless gluon fields G^α_μ are introduced, and the partial derivative is promoted to a covariant derivative:

$$D_\mu = \partial_\mu + i g_s \frac{\lambda^a}{2} G^a_\mu, \tag{2.15}$$

where g_s is the strong coupling constant, and λ^a are the Gell-Mann matrices, serving as the $SU(3)$ generators in the fundamental representation. The gluon fields themselves must also transform under $SU(3)$ as:

$$G^a_\mu \rightarrow G'^a_\mu = G^a_\mu - \frac{1}{g_s}\partial_\mu \alpha^a(x) - f^{abc}\alpha^b(x) G^c_\mu, \tag{2.16}$$

where $f^{abc}$are the structure constants of $SU(3)$. These terms give rise to self-interactions between gluons, a feature unique to non-Abelian gauge theories. The complete QCD Lagrangian combines the kinetic, interaction, and gluon field terms:

$$\mathcal{L}_{\text{QCD}} = \sum_{j=1}^{3} \bar{q}_j (i\gamma^\mu \partial_\mu - m) q_j - g_s \left(\bar{q}_j \gamma^\mu \frac{\lambda^a}{2} q_j\right) G^a_\mu - \frac{1}{4} G^a_{\mu\nu} G^{\mu\nu}_a, \tag{2.17}$$

where the gluon field strength tensor is given by:

$$G^a_{\mu\nu} = \partial_\mu G^a_\nu - \partial_\nu G^a_\mu - g_s f^{abc} G^b_\mu G^c_\nu. \tag{2.18}$$

This non-Abelian structure allows gluons to interact with each other, unlike photons in QED, leading to phenomena such as colour confinement and asymptotic freedom, which are key characteristics of the strong force.

2.1.4 *Unification of Electromagnetic and Weak Forces*

In the SM, the electromagnetic and weak forces are unified under a single theoretical framework known as the Electroweak (EWK) theory, which is based on a gauge symmetry described by the group:

$$SU(2)_L \otimes U(1)_Y. \tag{2.19}$$

Here, $SU(2)_L$ corresponds to weak isospin and acts on left-handed fermions, while $U(1)_Y$ represents weak hypercharge [7, 8] and acts on both left- and right-handed fermions. The theory introduces four gauge bosons associated with these symmetries. Fermions are described according to their chirality: left-handed components are projected using $P_L = \frac{1}{2}(1 - \gamma^5)$ and right-handed components use $P_R = \frac{1}{2}(1 + \gamma^5)$.

The $SU(2)_L$ gauge bosons $W^1_\mu, W^2_\mu, W^3_\mu$ couple only to left-handed doublets with weak isospin $I = 1/2$, while the $U(1)_Y$ boson B_μ couples to all fermions based on their hypercharge Y. The electric charge Q is related to weak isospin I_3 and hypercharge Y by:

$$Q = I_3 + \frac{Y}{2}. \tag{2.20}$$

The hypercharge involves right- and left-handed particles, therefore the Lagrangian density is invariant under $U(1)$. In this case the field transforms as:

$$\psi_{L,R} \to U(1)\,\psi_{L,R} = e^{i\alpha(x)Y/2}\psi_{L,R}. \tag{2.21}$$

On the other hand, isospin symmetry only applies to left-handed particles, therefore the Lagrangian is invariant under $SU(2)$ transformations. The field transforms as:

$$\psi_L \to SU(2)\,\psi_L = e^{i\beta^a(x)\tau^a/2}\psi_L, \tag{2.22}$$

with $\tau^a/2$ being the $SU(2)$ generators, with $a = 1, 2, 3$.

To obtain the physical gauge bosons, the four original fields associated with the electroweak symmetry group are combined into specific linear combinations. These combinations result in the emergence of:

(a) The photon field A_μ, which mediates the electromagnetic interaction:

$$A_\mu = \sin\theta_W\, W^3_\mu + \cos\theta_W\, B_\mu. \tag{2.23}$$

(b) The neutral Z boson field Z_μ, responsible for neutral weak interactions:

$$Z_\mu = \cos\theta_W \, W_\mu^3 - \sin\theta_W \, B_\mu. \tag{2.24}$$

(c) The charged W boson fields $W_{12}^\pm$, mediating charged current weak interactions:

$$W_{12}^\pm = \frac{1}{\sqrt{2}} \left(W_\mu^1 \mp i W_\mu^2 \right). \tag{2.25}$$

Here, θ_W is known as the Weinberg angle or weak mixing angle.

The dynamics of the electroweak interaction are described by the electroweak Lagrangian, which governs the behavior of the gauge and fermion fields. For a fermionic field ψ, the Lagrangian density takes the form:

$$\mathcal{L}_{\text{EWK}} = -\frac{1}{4} W_{\mu\nu}^a W^{a,\mu\nu} - \frac{1}{4} B_{\mu\nu} B^{\mu\nu} + i \, \bar{\psi} \gamma^\mu D_\mu \psi, \tag{2.26}$$

where the index $a = 1, 2, 3$ corresponds to the three gauge fields of $SU(2)_L$. $W_{\mu\nu}^a$ and $B_{\mu\nu}$ are the field strength tensors, encapsulating the dynamics of the non-Abelian and Abelian gauge fields, respectively. These are defined as:

$$B_{\mu\nu} = \partial_\mu B_\nu - \partial_\nu B_\mu, \tag{2.27}$$

$$W_{\mu\nu}^a = \partial_\mu W_\nu^a - \partial_\nu W_\mu^a - i g_W \, \epsilon^{abc} \{ W_\nu^b, W_\mu^c \}. \tag{2.28}$$

The covariant derivative D_μ, which ensures gauge invariance under both $SU(2)_L$ and $U(1)_Y$ transformations, is given by:

$$D_\mu = \partial_\mu + i g W_\mu^a I^a + i \frac{g'}{2} B_\mu Y, \tag{2.29}$$

where g and g' are the coupling constants for the $SU(2)_L$ and $U(1)_Y$ groups, respectively. The weak mixing angle θ_W is related to the coupling constants by:

$$\sin(\theta_W) = \frac{g'}{\sqrt{g^2 + g'^2}}, \tag{2.30}$$

$$\cos(\theta_W) = \frac{g}{\sqrt{g^2 + g'^2}}. \tag{2.31}$$

Despite the success of the EWK theory in unifying the electromagnetic and weak forces, the gauge symmetry $SU(2)_L \otimes U(1)_Y$ prohibits the inclusion of explicit mass terms for the gauge bosons $W^\pm$ and Z. However, these particles are experimentally observed to be massive, indicating that the gauge symmetry must be broken in a controlled way. The resolution to this inconsistency lies in the mechanism of electroweak spontaneous symmetry breaking [9], achieved via the introduction of the Higgs field, which allows the $W^\pm$ and Z bosons to acquire mass while preserving the overall gauge invariance of the theory. This mechanism and its implications will be discussed in the next section.

2.1.5 *Electroweak Symmetry Breaking and the Higgs Mechanism*

The Brout-Englert-Higgs mechanism [10] provides the theoretical foundation for mass generation in the Standard Model by introducing a complex scalar field ϕ, which transforms as a doublet under $SU(2)_L$. This field interacts with the gauge bosons and allows for the acquisition of mass by particles carrying non-zero weak hypercharge, all while maintaining gauge invariance. It causes the spontaneous symmetry breaking of the electroweak symmetry:

$$SU(2)_L \otimes U(1)_Y \longrightarrow U(1)_{\mathrm{EM}}. \tag{2.32}$$

This mechanism ensures that the electromagnetic gauge symmetry remains unbroken, preserving the massless nature of the photon which means the photon remains massless, while the $W^{\pm}$ and Z bosons gain mass. The Higgs field is introduced as a doublet with isospin $I = 1/2$, third component $I_3 = -1/2$, and hypercharge $Y = 1$:

$$\phi(x) = \begin{pmatrix} \phi^+(x) \\ \phi^0(x) \end{pmatrix}. \tag{2.33}$$

Both ϕ^+ and ϕ^0 are complex scalar fields.

The Lagrangian for the Higgs field is:

$$\mathcal{L}_H = (D_\mu \phi)^\dagger (D^\mu \phi) + V(\phi). \tag{2.34}$$

The scalar potential is shown in Figure 2.2 and takes the form:

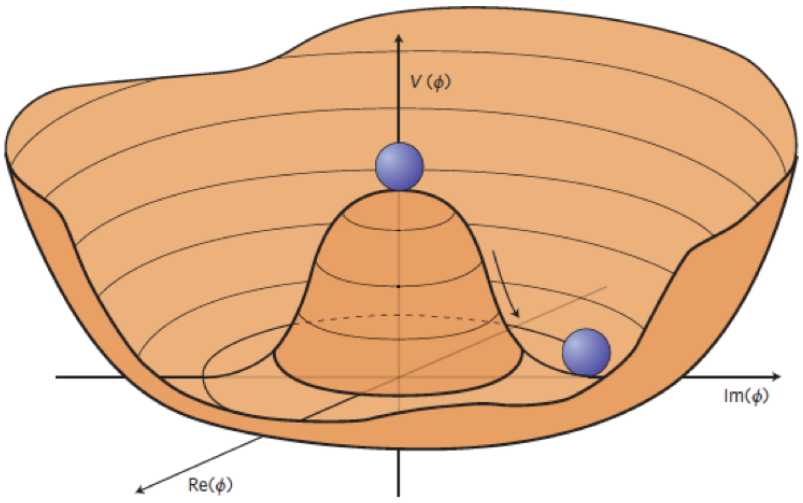

Figure 2.2: A Mexican hat potential that leads to spontaneous symmetry breaking. Figure is taken from Ref. [11].

$$V(\phi) = -\mu^2(\phi^\dagger\phi) + \lambda(\phi^\dagger\phi)^2. \tag{2.35}$$

The condition $\lambda > 0$ ensures the potential is bounded from below. For $\mu^2 < 0$, the potential develops a degenerate minimum at a non-zero value of ϕ, resulting in spontaneous symmetry breaking. The minimum of the potential defines the Vacuum Expectation Value (VEV):

$$\langle\phi\rangle = \frac{1}{\sqrt{2}}\begin{pmatrix}0\\ v\end{pmatrix}, \quad v = \sqrt{\frac{\mu^2}{\lambda}}. \tag{2.36}$$

The VEV v can be evaluated using the relation:

$$\frac{G_F}{\sqrt{2}} = \frac{g^2}{8m_W^2} \quad \Rightarrow \quad v = \frac{2m_W}{g} = \left(\sqrt{2}G_F\right)^{-1/2}. \tag{2.37}$$

After gauge fixing, three of the four degrees of freedom in ϕ are absorbed as the longitudinal components of the $W^\pm$ and Z bosons. The remaining degree of freedom corresponds to the physical Higgs boson $h(x)$, and the field can be written as:

$$\phi(x) = \frac{1}{\sqrt{2}}\begin{pmatrix}0\\ v + h(x)\end{pmatrix}. \tag{2.38}$$

Substituting this into the Lagrangian yields the mass terms for the electroweak gauge bosons:

$$m_W = \frac{gv}{2}, \tag{2.39}$$

$$m_Z = \frac{v}{2}\sqrt{g^2 + g'^2}, \tag{2.40}$$

$$m_\gamma = 0. \tag{2.41}$$

This framework not only provides a mechanism for gauge boson mass generation but also ensures the preservation of gauge invariance, unitarity, and renormalizability of the electroweak theory. The Higgs boson, which was theoretically predicted long before its experimental discovery [12, 13], is central to this mechanism [14] and constitutes a cornerstone of the SM.

2.2 $Z^0 \to e^+e^-$ production in proton–proton collisions

In proton–proton collisions at high energies, such as those occurring at the LHC, the production of Z bosons followed by their decay into lepton-antilepton pairs ($Z \to l^+l^-$) provides a clean and well-understood signature. This is commonly known as Drell–Yan process. The name comes from Sidney Drell and Tung-Mow Yan who first introduced the process in 1970 [15]. The annihilation of a quark-antiquark pair leads to a production of the Z boson, which decays into a lepton pair of opposite

charges:

$$\bar{q}q \rightarrow \gamma^*/Z \rightarrow \ell^+\ell^- \tag{2.42}$$

The process is shown in Figure 2.3. In the Drell–Yan process, lepton pair production at LHC is me-

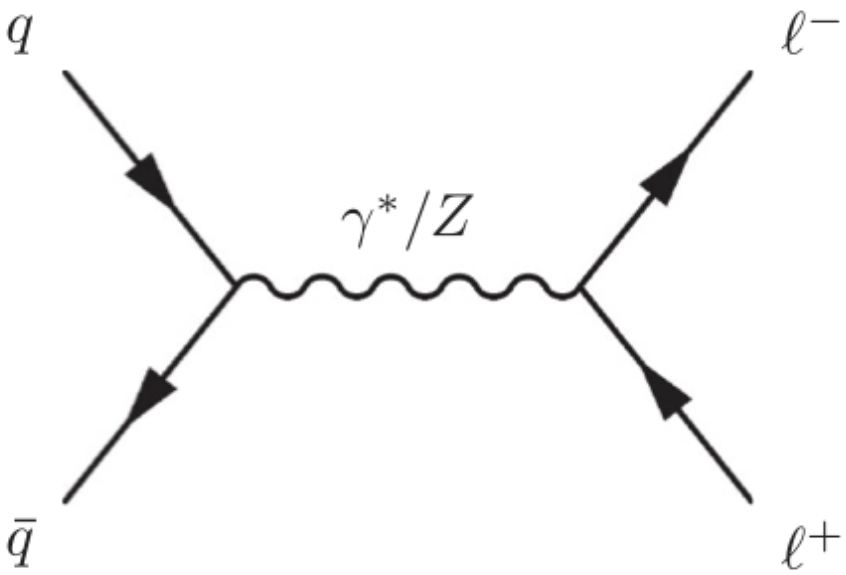

Figure 2.3: A diagram describing a SM Drell–Yan process.

diated by either a virtual photon (γ^*) or a neutral weak boson (Z). When the invariant mass of the lepton pair M_{ll} is significantly lower than the mass of the Z boson (M_Z), the production is predominantly governed by the virtual photon channel. However, as M_{ll} approaches M_Z, the contribution from the Z boson becomes resonantly enhanced, and its interference with the photon-mediated channel becomes significant. In this mass range, the process is dominated by Z boson production, making the Drell–Yan mechanism the primary mode of Z boson generation at the LHC [16].

The production of dileptons via γ^*/Z exchange is referred to as Neutral Current (NC) Drell–Yan [17], due to the electrically neutral nature of the mediating bosons. In parallel, the Charged Current (CC) Drell–Yan process [18] involves the annihilation of a quark–antiquark pair into a charged weak boson ($W^\pm$), which subsequently decays into a lepton and its associated neutrino:

$$W^- \rightarrow \ell^- \bar{\nu}, \quad W^+ \rightarrow \ell^+ \nu \tag{2.43}$$

As mentioned earlier, the Drell–Yan process involves the annihilation of a quark and an antiquark into a neutral boson, which then decays into a lepton pair. In proton–proton collisions, these quarks and antiquarks are not the whole proton, rather originate from the internal structure of the protons — a structure described by the so-called parton sea. This sea consists of dynamically generated quarks,

antiquarks, and gluons, each carrying a small fraction of the proton's total momentum. These momentum fractions are denoted as x_q and $x_{\bar{q}}$ for the quark and antiquark, respectively.

The effective center-of-mass energy available for the partonic interaction is significantly less than the total energy of the colliding protons and is given by:

$$\hat{s} = x_q \, x_{\bar{q}} \, s, \tag{2.44}$$

where s is the total proton–proton center-of-mass energy, and $\hat{s}$ is the center-of-mass energy of the partonic subprocess. At leading order (LO), neglecting additional QCD corrections [19], the cross section for the partonic process $q\bar{q} \to Z^0$ is given by:

$$\sigma(q\bar{q} \to Z^0) = \frac{8\pi G_F}{\sqrt{2}} M_Z^2 (g_V^2 + g_A^2) \, \delta(\hat{s} - M_Z^2). \tag{2.45}$$

Here, G_F is the Fermi constant, and g_V, g_A are the vector and axial-vector couplings of the quark to the Z boson. The delta function enforces that the Z boson is produced on-shell, i.e., at its physical mass.

To compute the total cross section for Z boson production in proton–proton collisions, one must incorporate the Parton Distribution Functions (PDFs). These functions, denoted $f_q(x)$, describe the probability density of finding a parton (quark, antiquark, or gluon) with a given momentum fraction x inside the proton. The total hadronic cross section for Z production is obtained by integrating over all possible parton momentum fractions and summing over all quark flavors:

$$\sigma_{\text{tot}}(\hat{s})(pp \to Z^0) = \int dx_1 \, dx_2 \, \hat{\sigma}_Z(\hat{s}) \sum_q \left[f_q(x_1) f_{\bar{q}}(x_2) + f_{\bar{q}}(x_1) f_q(x_2) \right]. \tag{2.46}$$

This formulation reflects the probabilistic nature of the parton model and ensures that all relevant contributions to the Z boson production are properly accounted for. From Particle Data group (PDG) [20], the mass of Z boson is $m_Z = 91.1880 \pm 0.0020$ GeV and total decay width is $\Gamma_Z = 2.4955 \pm 0.0023$ GeV. The branching ratio of Z boson in different decay modes are given in Table 2.1:

Decay Mode	$\frac{\Gamma_i}{\Gamma}$ (%)
e^+e^-	3.3632 ± 0.0042
$\mu^+\mu^-$	3.3662 ± 0.0066
$\tau^+\tau^-$	3.396 ± 0.0083
invisible	20.00 ± 0.055
hadrons	69.911 ± 0.056

Table 2.1: Branching fractions of various Z^0 boson decay modes.

The decay channel $Z^0 \to e^+e^-$ is particularly advantageous due to the clear identification of high-energy electrons in the detector and the excellent resolution of the dielectron invariant mass, which peaks sharply at the Z boson mass. This channel is extensively used for electron reconstruction and identification efficiency studies, as well as for deriving scale factors and validating detector performance. Moreover, since the two final-state electrons are expected to have opposite charges, this pro-

cess serves as a powerful tool in studying charge misidentification (or "charge flip") probabilities. Any observed same-sign *ee* pairs can be attributed to detector effects, enabling data-driven estimations of charge flip rates.

CHAPTER 3

The LHC and the ATLAS Detector

The ATLAS Collaboration is a global scientific effort dedicated to advancing our understanding of particle physics through experimental investigations of proton–proton collisions at the Large Hadron Collider (LHC), situated at CERN (Conseil Européen pour la Recherche Nucléaire) in Geneva, Switzerland. This collaboration brings together approximately 6000 members and 3000 scientific authors from more than 170 institutions across 40 countries worldwide [21]. This chapter provides an overview of the LHC, including its operational infrastructure and key performance specifications. It also offers a detailed description of the ATLAS detector, highlighting its components and their roles in high-energy particle measurements.

3.1 The Large Hadron Collider

CERN was established in 1954 in Geneva, Switzerland, and is home to the world's most powerful particle accelerator—the LHC. Following the decommissioning of the Large Electron-Positron (LEP) collider [22] in 2001, construction of the LHC commenced using the same underground tunnel, which was reconfigured to accommodate its new design consisting of eight arcs and eight straight sections [23]. Located approximately 100 meters underground, the LHC is a 26.7 kilometer long circular accelerator designed to collide hadrons, such as protons or heavy ions, at unprecedented center-of-mass energies and collision rates. The LHC began operations in 2008, with the first proton–proton collisions recorded shortly thereafter. By 2010, the collider had ramped up to a collision energy of 7 TeV, marking the beginning of its main physics program. A moderate energy increase to 8 TeV occurred by 2012. In 2015, the LHC entered a new era of high-energy physics with collisions at 13 TeV, and most recently, in 2022, the collision energy was further raised to 13.6 TeV, expanding the potential for new discoveries beyond the Standard Model.

In high-energy collider experiments such as those conducted at the LHC, a primary objective is to quantify the frequency at which specific physical processes occur. The event production rate, denoted as

$$\dot{N} = \frac{dN}{dt} = L \cdot \sigma, \tag{3.1}$$

gives the number of events happening per unit time. This rate depends on two key quantities: σ, the cross section of the process, quantifies the probability of the process occurring in a single collision and L, the instantaneous luminosity, which characterizes how many particles are colliding per unit area per unit time. Certain physical processes occur with extremely low probability, corresponding to very small production cross sections. In order to collect a statistically meaningful sample of such rare events, an enormous number of proton–proton collisions must be produced. Since the cross section σ is determined by the underlying physics and cannot be altered experimentally, the only viable approach to increasing the event rate $\dot{N}$ is by enhancing the instantaneous luminosity L. Thus, by integrating the rate over time, we get the total no. of events over a period of time:

$$N = \sigma \cdot \int L(t)\, dt \equiv \mathcal{L} \cdot \sigma, \tag{3.2}$$

where $\mathcal{L}$ is the integrated luminosity measured in units of inverse barn and is often measured in inverse femtobarn.

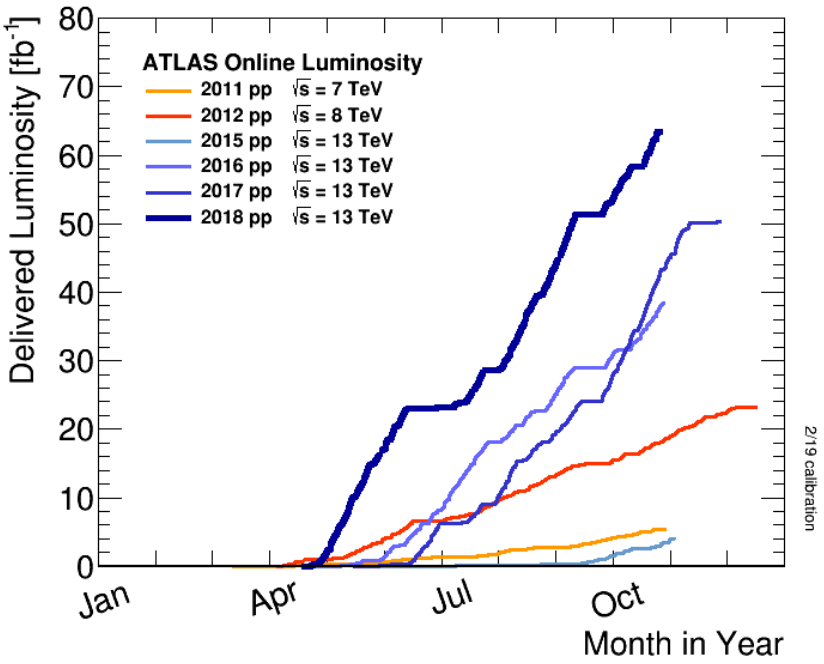

Figure 3.1: Cumulative luminosity versus day delivered to ATLAS during stable beams and for high energy proton–proton collisions. Plot is taken from Ref. [24].

The operational periods between major upgrades to the accelerator and detectors are referred to as Runs. Originally designed to achieve particle collisions at center-of-mass energies up to $\sqrt{s} = 14$ TeV with an instantaneous luminosity of $L = 10^{34}\,\mathrm{m}^{-2}\,\mathrm{s}^{-1}$, the LHC has gradually increased both its energy and luminosity capabilities over time [25]. The progression of the cumulative integrated luminosity delivered by the LHC during Run 1 and Run 2 is illustrated in Figure 3.1. Notably, during Run

2, the LHC demonstrated outstanding performance, with a significant enhancement in instantaneous luminosity observed from 2016 to 2018, as indicated by the blue curves in Figure 3.1. Figure 3.2 shows the all data recorded by ATLAS during stable beams, the integrated luminosity and the mean μ value. The mean number of interactions per crossing corresponds to the mean of the poisson distribution of the number of interactions per crossing calculated for each bunch. It is calculated from the instantaneous per bunch luminosity as $\mu = L_{\text{bunch}} \times \sigma_{\text{inel}} / f_r$ where L_{bunch} is the per bunch instantaneous luminosity, σ_{inel} is the inelastic cross section which we take to be 80 mb for 13 TeV collisions, and f_r is the LHC revolution frequency [24].

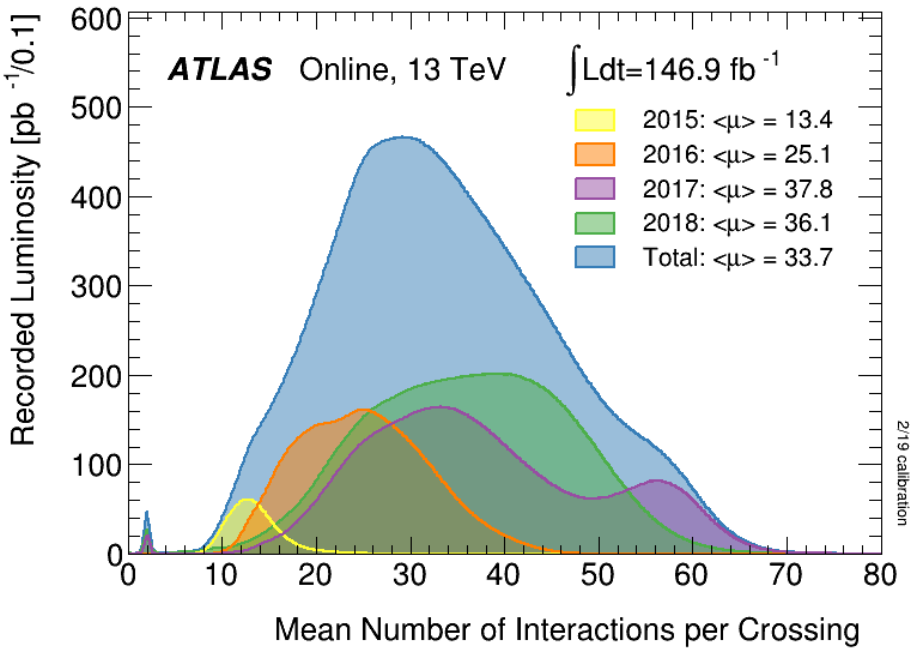

Figure 3.2: Luminosity summary plot. Luminosity-weighted distribution of the mean number of interactions per crossing for the 2015 – 2018 pp collision data at 13 TeV centre-of-mass energy. Plot is taken from Ref. [24]

The LHC achieves proton–proton collisions at center-of-mass energies up to 13.6 TeV, facilitated by a series of pre-accelerators that incrementally increase proton energies. A significant enhancement to this injector chain was the commissioning of Linear Accelerator 4 (Linac4) [26] in 2020, replacing the older Linac2 [27]. Unlike its predecessor, Linac4 accelerates negatively charged hydrogen ions (H^-) [28] to 160 MeV. These ions are then injected into the Proton Synchrotron Booster (PSB) [29], where they pass through a thin carbon foil that strips away the electrons, resulting in bare protons. Following the PSB, protons are accelerated to 2 GeV and transferred to the Proton Synchrotron (PS), which boosts their energy to 26 GeV. Subsequently, the Super Proton Synchrotron (SPS) increases the proton energy to 450 GeV before injection into the LHC ring. The pre-acceleration facilities of the LHC are presented in Figure 3.3.

The LHC employs 16 superconducting Radio Frequency (RF) cavities, organized into four cry-

omodules, to accelerate protons from an injection energy of 450 GeV to a collision energy of 6.5 TeV. Each cavity operates at 400 MHz and provides an accelerating voltage of 2 MV, resulting in a total of 16 MV per beam per revolution. The cavities are maintained at a superconducting state by cooling them to 4.5 K using cryogenic systems. The field in an RF cavity is made to oscillate (switch direction) at a given frequency, so timing the arrival of particles is important. In the LHC, each RF cavity is tuned to oscillate at 400 MHz. When the beam has reached the required energy, an ideally timed proton with exactly the right energy will not be accelerated. By contrast, protons with slightly different energies arriving earlier or later will be accelerated or decelerated so that they stay close to the desired energy. In this way, the particle beam is sorted into packs of protons called "bunches". Thousands of magnets of different varieties and sizes are used to direct the beams around the accelerator. These include 1232 dipole magnets, 15 meters in length, which bend the beams, and 392 quadrupole magnets, each 5–7 meters long, which focus the beams [30]. The LHC have four detectors at four primary interaction points, each designed to explore different aspects of particle physics. **ATLAS** and **CMS** are general-purpose detectors located at opposite sides of the LHC ring. They investigate a wide range of physics phenomena, including the search for the Higgs boson and potential new particles. **ALICE** is specialized in studying heavy-ion collisions. **LHCb** is focused on the study of b-hadrons. In the following section, we will describe the various components of the ATLAS detector.

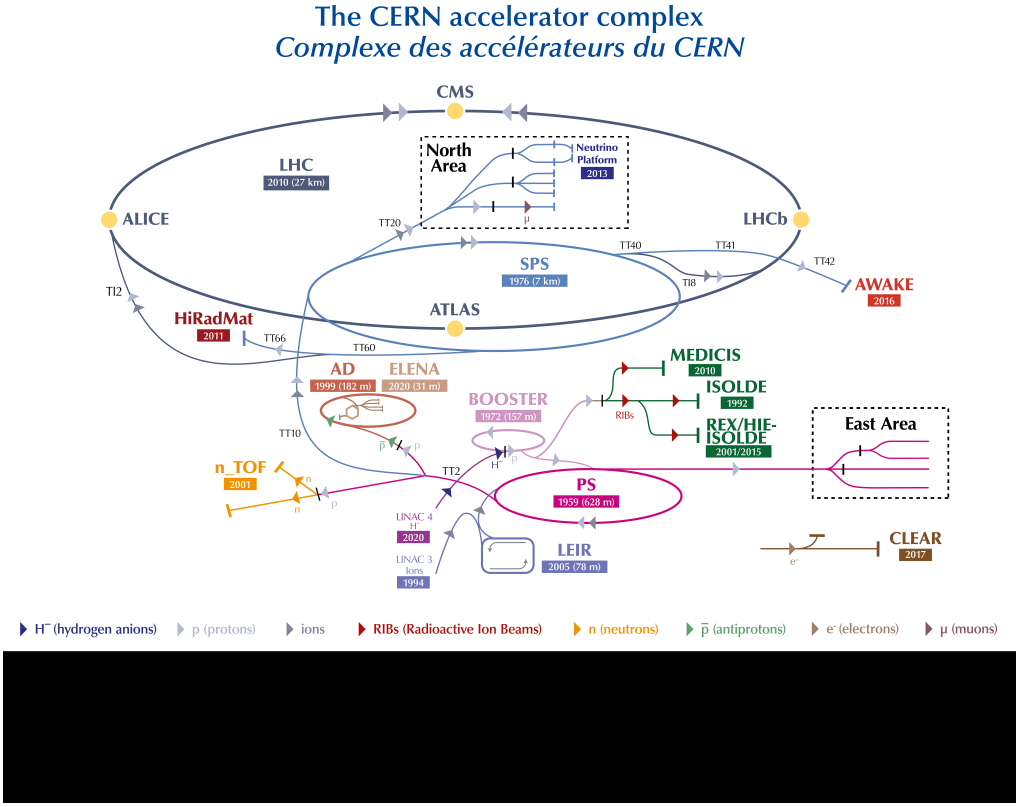

Figure 3.3: The CERN accelerator complex. Figure is taken from Ref. [31].

3.2 The ATLAS Detector

The ATLAS (A Toroidal LHC ApparatuS) experiment [32] at LHC is a general-purpose particle detector designed for high-precision measurements and the exploration of new physics phenomena in high-luminosity environments. A labelled cut-away view is presented in the Figure 3.4. The main components of the detector are **the inner detector (ID)**, electromagnetic and hadronic **calorimeters** and **muon spectrometer**, which are explained in the following sections.

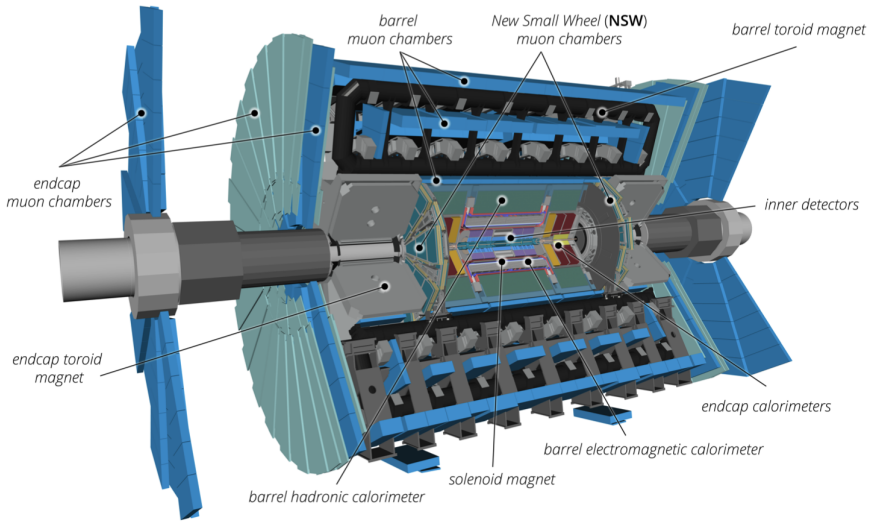

Figure 3.4: Cut-away view of the ATLAS detector indicating the locations of the larger detector sub-systems. Plot is taken from Ref. [33].

3.2.1 *Geometry and Coordinate System*

The ATLAS detector employs a right-handed coordinate system to accurately describe particle trajectories resulting from proton–proton collisions. In this system x-axis points from the interaction point toward the center of the LHC ring, y-axis is directed vertically upward and z-axis is aligned along the beam pipe, following the direction of the proton beams. The origin of this coordinate system is defined at the nominal interaction point, which is determined for each event. Considering standard cylindrical coordinate system, *polar angle* θ is the angle between a particle's trajectory and the beam axis (z-axis) and *azimuthal angle* ϕ is measured around the beam axis in the transverse (x-y) plane, starting from the x-axis.

To effectively describe particle kinematics, especially in the context of hadron colliders, two related quantities are commonly used: *pseudorapidity* and *transverse momentum*. Transverse momentum (p_T) refers to the component of a particle's momentum that is perpendicular to the beam axis. Pseudorapidity (η) describes the angle of a particle relative to the beam axis. It can be written in terms of the

polar angle θ as:

$$\eta = -\ln \tan\left(\frac{\theta}{2}\right). \tag{3.3}$$

Particles with $|\eta| < 2.5$ are considered to be in the central region of the detector. These particles are emitted at larger angles relative to the beam axis and are typically detected in the barrel section of the detector whereas, particles with $|\eta| > 2.5$ are emitted at smaller angles, closer to the beam axis, and are detected in the endcap or forward sections of the detector.

The separation between two objects in the detector is commonly expressed in terms of their angular distance in the (η-ϕ) plane, defined by

$$\Delta R = \sqrt{(\Delta\eta)^2 + (\Delta\phi)^2}, \tag{3.4}$$

and transverse energy (E_T) quantifies the energy of a particle relative to its motion in the plane perpendicular to the beam direction.

3.2.2 *The Inner Detector*

The Inner Detector (ID) [34] is a crucial component of the ATLAS experiment, designed to precisely track charged particles produced in high-energy proton–proton collisions. Situated closest to the beam axis, the ID operates within a 2 Tesla magnetic field generated by a central solenoid, enabling the measurement of particle trajectories, momenta, and charges. The ID comprises three primary sub-detectors, each contributing to the overall tracking performance: **pixel detector**, **semi-conductor tracker** and **Transition Radiation Tracker (TRT)**. The three sub-detectors of the ID are presented in 3.5.

The ATLAS pixel detector is the innermost component of the ATLAS ID, designed to provide high-resolution tracking of charged particles. The pixel detector comprises four concentric barrel layers and two end-cap disks on each side, covering a radial distance from approximately 45.5 mm to 242 mm [35]. Each barrel layer is populated with silicon pixel modules, with the innermost layer, known as the Insertable B-Layer (IBL), installed at a radius of 33 mm during the first long shutdown before Run 2 [36]. The addition of the IBL improved the detector's resolution, particularly for low p_T particles, which are more susceptible to multiple scattering effects. This enhancement is crucial for applications such as jet tagging and b-quark identification. The pixel detector operates by applying a reverse-biased voltage across a silicon sensor, creating a depletion region. When a charged particle traverses this region, it generates electron-hole pairs. These charge carriers are collected by the pixel electrodes, producing a measurable signal. The amount of charge collected correlates with the energy deposited by the particle, while the specific pixel that registers the signal indicates the particle's position. Each pixel module consists of a silicon sensor segmented into pixels measuring $50 \times 400\ \mu m^2$ in the outer layers and $50 \times 250\ \mu m^2$ in the IBL.

The Semi-Conductor Tracker (SCT), is the middle layer of the ID, covers the radial region from 255 mm to 549 mm [37] and comprises of four and two layers of silicon microstrip sensors in the

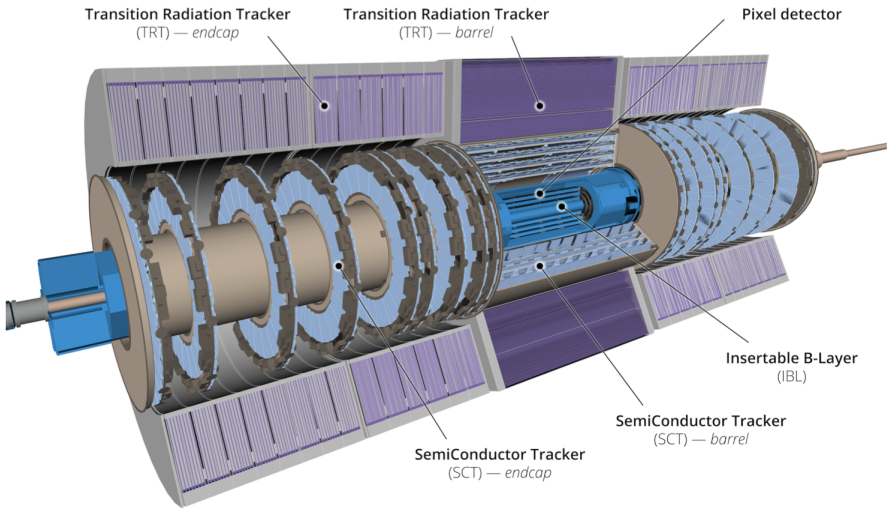

Figure 3.5: Cut-away view of the ATLAS ID. It is designed to enable precise reconstruction of charged-particle trajectories. It provides full azimuthal coverage (ϕ) and operates within a pseudorapidity range of $|\eta| < 2.5$. The ID is composed of three subsystems: the innermost layer is a silicon pixel detector, which is surrounded by a silicon microstrip tracker. Enclosing these is the Transition Radiation Tracker (TRT), a straw-tube detector that offers continuous tracking while also enabling particle identification through the detection of transition radiation. Figure is taken from Ref. [33].

barrel and end-cap regions respectively. Further, these sensors are organized in modules where each module is made up of two planes of silicon sensors glued back to back with a baseboard material in the middle. In total, the SCT contains approximately 6.3 million readout channels and usually provides eight measurements per track. The spatial resolution achieved by the SCT is about 17 μm in the transverse (r–ϕ) direction and 580 μm along the z-axis.

The TRT is the outermost component of the ATLAS ID, designed to provide both precise tracking of charged particles and effective electron identification. It covers the radial distance from 554 mm to 1082 mm [38] and composed of several layers of gaseous straw tubes. The TRT enables radially extended track reconstruction up to $|\eta| = 2.0$. The TRT also provides electron identification information based on the fraction of hits above a higher energy-deposit threshold corresponding to transition radiation.

3.2.3 Calorimeters

The ATLAS calorimeter system is designed to measure the energies and positions of charged and neutral particles that undergo electromagnetic or strong interactions. They are designed to absorb most of the particles coming from a collision, forcing them to deposit all of their energy and stop within the detector [39]. It employs a sampling calorimeter approach, wherein layers of dense absorber materials are interleaved with active media that detect and measure the energy deposited by incoming particles [33]. ATLAS has two types of calorimeters: Electromagnetic Calorimeters (ECAL) which measure the energy of particles such as electrons and photons and Hadronic Calorimeters (HCAL)

which measure the energy of strongly-interacting particles, primarily hadrons. The calorimeters are highlighted in Figure 3.6.

The ECAL employs a sampling calorimeter design, utilizing layers of lead as the passive absorber material and Liquid Argon (LAr) as the active medium. It is divided into three main sections: the barrel and two endcaps. The barrel covers the central region up to $|\eta| < 1.475$, while the endcaps extend the coverage to $|\eta| < 3.2$ [40]. This extensive coverage ensures the detection of particles emitted at various angles relative to the beam axis. The calorimeter's structure features an accordion-shaped geometry, which ensures full azimuthal coverage without gaps, enhancing the uniformity of the detector response. When a high-energy electron or photon enters the calorimeter, it initiates an electromagnetic shower, producing secondary particles that ionize the LAr. The resulting ionization electrons drift under an applied electric field towards the readout electrodes, generating signals proportional to the energy of the incident particle.

The HCAL is structured into three main sections: the tile calorimeter, the hadronic endcap calorimeters, and the forward calorimeters. The tile calorimeter covers the central region ($|\eta| < 1.7$) using steel absorbers and plastic scintillators. When hadrons pass through they interact with the steel, producing secondary particles that excite the scintillators. The resulting light is captured by wavelength-shifting fibers and directed to photomultiplier tubes (PMTs) for signal processing. Hadronic endcap calorimeters extend coverage to $1.5 < |\eta| < 3.2$, utilizing liquid argon as the active medium and copper plates as absorbers. The forward calorimeters cover the high pseudorapidity range of $3.1 < |\eta| < 4.9$. They consist of three modules: the first is optimized for electromagnetic interactions using copper absorbers, while the subsequent two are tailored for hadronic interactions with tungsten absorbers. All modules employ liquid argon as the active medium, ensuring resilience in the high-radiation environment characteristic of the forward regions.

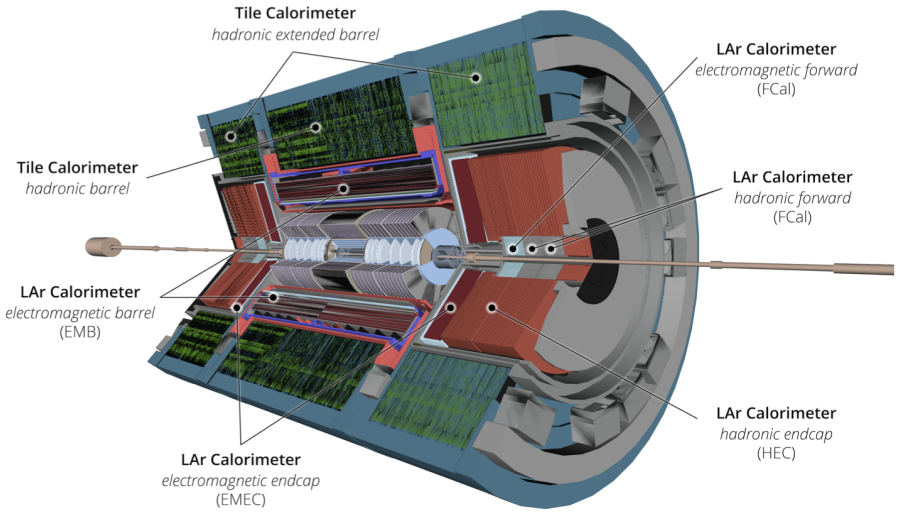

Figure 3.6: Cut-away view of the ATLAS calorimeter system. It measures the energies and positions of charged and neutral particles. Figure is taken from Ref. [33].

3.2.4 *Muon Spectrometer*

The Muon Spectrometer (MS) [41] is the outermost layer of the ATLAS detector. Its purpose is to detect muons, which are more massive than electrons, typically penetrate deeper into the detector with minimal energy loss. It is designed specifically to reconstruct muon trajectories over long distances after they pass through the inner detectors and the calorimeters. The system covers a wide pseudorapidity range, up to $|\eta| < 2.7$. The main working principle is the magnetic deflection of muons using large superconducting air-core toroid magnets. Over the range $|\eta|$<1.4, magnetic bending is provided by the large barrel toroid. For 1.6 < $|\eta|$<2.7, muon tracks are bent by two smaller endcap toroid magnets inserted into both ends of the barrel toroid. In between these two regions, 1.4 < $|\eta|$<1.6, magnetic deflection is provided by a combination of barrel and endcap fields [33]. The MS comprises a set of three sub-detectors: Monitored Drift Tubes (MDT) [42], Resistive Plate Chambers (RPC) [43] and Thin Gap Chambers (TGC) shown in Figure 3.7.

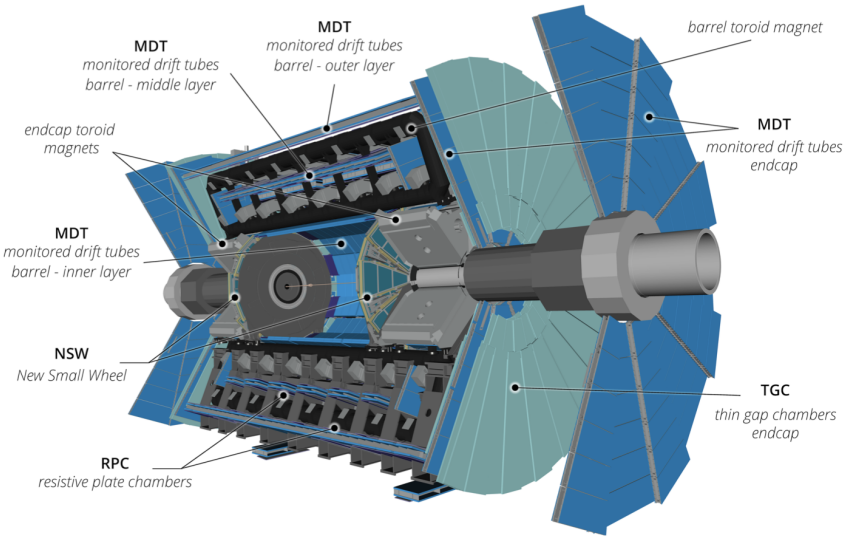

Figure 3.7: Cut-away view of the ATLAS muon system. It detects charged particles exiting the barrel and endcap calorimeters. Figure is taken from Ref. [33].

To cope with the high particle flux, the spectrometer was designed with detectors that offer high rate capability, fine spatial granularity, strong radiation resistance, and long-term stability. The barrel detectors have multilayer MDT chambers across all three stations for precise tracking in the bending plane. Additionally, the middle and outer barrel stations include RPCs for triggering and for determining the azimuthal coordinate. The middle and outer endcap wheels also provide continued coverage. The extended endcap rings add a third measurement station for the range 1.05 < $|\eta|$ < 1.3, which the outer wheels do not cover. While the outer wheels use MDTs exclusively, the middle wheels combine MDTs with TGCs for both precision and trigger measurements. The inner endcap wheels, or "small wheels," have been completely replaced in the Phase-I upgrade by the New Small Wheels (NSWs) [44],

located between the calorimeters and the endcap toroids. Covering the range $1.3 < |\eta| < 2.7$, the NSWs employ small-strip TGCs and micromegas detectors, both fast enough for Level-1 triggers and precise in both bending and azimuthal measurements. This upgrade enhances the low p_T muon resolution at trigger level and improves background rejection, enabling lower p_T thresholds and preserving physics acceptance while controlling the trigger rate.

3.2.5 *Trigger and Data Acquisition*

In ATLAS experiment, billions of proton–proton collisions occur every second. However, only a tiny fraction of these collisions are potentially interesting for physics analysis such as Higgs production. The rest are either uninteresting or contain common physics processes. Since it is impossible to record every collision due to limitations in data storage and processing power, a trigger system is used to filter and select only the relevant events. It is based on two-level trigger system: Level-1 (L1) trigger which is a hardware-based system built from custom-designed electronics that operate extremely fast and High-Level Trigger (HLT) is a software-based system, runs on a farm of commercial computers [45]. Data Acquisition System (DAQ), works together with the trigger system, responsible for moving data from detector electronics to the computing/storage systems and transfers data only for those events that the trigger accepts. A complete diagram of the Trigger and Data Acquisition (TDAQ) System [46] is shown in Figure 3.8.

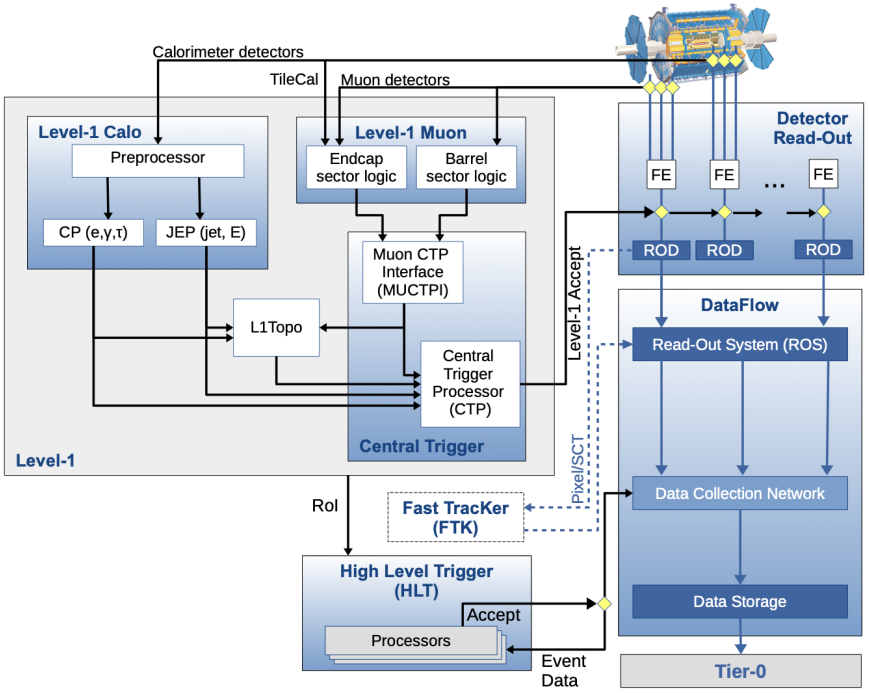

Figure 3.8: Schematic overview of the trigger and DAQ system in ATLAS for Run 2. Figure is taken from Ref. [45].

The L1 trigger processes detector data at the full 40 MHz collision rate, to quickly identify physics objects like high-p_T muons, electrons, photons, jets, and hadronic tau decays. It also estimates missing transverse energy (E_T^{miss}) from invisible particles like neutrinos. These objects are compared against predefined conditions in the L1 trigger menu. Events passing the L1 criteria are reduced to a rate of 100 kHz. Events accepted by the L1 trigger are passed to the HLT, which applies advanced software-based selection algorithms [47]. These are focused on specific regions of interest (RoIs) in the detector, reducing computational load by ignoring irrelevant areas. Within the RoIs, the HLT uses full detector granularity to make refined decisions, ultimately reducing the event rate from 100 kHz to 1 kHz on average within a processing time of about 200 ms during Run 2. Selected events are then saved for offline analysis [48]. The event processing time in Run 3 is larger due to widespread use of full-detector HLT track reconstruction for hadronic signatures. The HLT reduces the event rate from 100 kHz after the L1 selection to approximately 3 kHz [49].

When an event passes the ATLAS trigger system (including both L1 and HLT), it is recorded in a format called RAW data. These RAW events are not all written to the same output, rather they are organized into inclusive "streams" to manage data handling, storage, and downstream processing. Inclusive means that an event can be assigned to more than one stream. Each trigger chain is assigned to a single stream which ensures that the stream includes all events relevant to a given trigger. In Run 2, there is one primary physics stream `physics_main`, which includes the majority of physics triggered events, spanning all major object categories. There are also other special purpose streams like `Minbias` and `physics_Late`; however, only `physics_main` is used in this thesis. The next step is the reconstruction of the data and the standard output format of the reconstruction is called Analysis Object Data (AOD) containing physics objects and some lower-level information, such as particle flow objects and a limited amount of calorimeter cell information. For the purposes of physics analysis, the AOD is further reduced to a more compact format known as the Derived Analysis Object Data (DAOD). For this thesis, the DAOD_PHYS format is used, which is a new common format for physics analysis.

CHAPTER 4

Datasets and Simulated-Event Samples

4.1 Datasets

This thesis use the full pp collision dataset recorded by ATLAS between 2015 and 2018 with the LHC operating at a center-of-mass energy of $\sqrt{s} = 13\ TeV$. In this period, the LHC delivered colliding beams with a peak instantaneous luminosity up to $L = 2.1 \times 10^{34}\,\mathrm{cm}^{-2}\,\mathrm{s}^{-1}$, and an average number of pp interactions per bunch crossing $\langle\mu\rangle$ of 13, 25, 38, and 34 for 2015, 2016, 2017, and 2018 data, respectively. After applying beam, detector, and data-quality criteria the total integrated luminosity of the data is $140\ fb^{-1}$ [25]. Data recorded in 2022 and 2023 at a center-of-mass energy of $\sqrt{s} = 13.6\ TeV$ with bunch spacing of 25 ns is also used. The recorded integrated luminosity in 2022 was 35.7 fb^{-1} and in 2023 was 29.9 fb^{-1} [24]. The list of datasets used in this thesis are presented in Table 4.1.

Table 4.1: Integrated luminosity and dataset list for each data-taking year during Run 2 and Run 3.

Year	Int. Lumi. (fb^{-1})	Dataset
2015	3.9	`data15_13TeV.periodAllYear.physics_Main.PhysCont.DAOD_PHYS.grp15_v01_p6479`
2016	35.6	`data16_13TeV.periodAllYear.physics_Main.PhysCont.DAOD_PHYS.grp16_v01_p6479`
2017	46.9	`data17_13TeV.periodAllYear.physics_Main.PhysCont.DAOD_PHYS.grp17_v01_p6479`
2018	60.6	`data18_13TeV.periodAllYear.physics_Main.PhysCont.DAOD_PHYS.grp18_v01_p6479`
2022	35.7	`data22_13p6TeV.periodAllYear.physics_Main.PhysCont.DAOD_PHYS.grp22_v02_p6479`
2023	29.9	`data23_13p6TeV.periodAllYear.physics_Main.PhysCont.DAOD_PHYS.grp23_v02_p6479`

The naming of the datasets follows the convention as:

$$\underbrace{\texttt{data15\_13TeV}}_{\text{Project tag}} \cdot \underbrace{\texttt{periodAllYear}}_{\text{Data period}} \cdot \underbrace{\texttt{physics\_Main}}_{\text{Stream type}} \cdot \underbrace{\texttt{PhysCont.DAOD\_PHYS}}_{\text{Data format type}} \cdot \underbrace{\texttt{grp15\_v01\_6479,}}_{\text{Production tags}}$$

where project tag represents that data is taken in 2015 with p–p collision at $\sqrt{s} = 13\ TeV$, data period (`AllYear`) covers the data in whole year 2015, and `PhysCont.DAOD_PHYS` represents the collection of data in a container in DAOD_PHYS format. Each processing step changes the data type and adds the ATLAS Metadata Interface (AMI) production tag used which describes the configuration of each step.

4.2 Monte Carlo Simulation

Monte Carlo (MC) simulations are computational tools that play a central role in high energy physics experiments. They are used to emulate the outcomes of particle collisions as they would be observed by a detector, based on underlying theoretical models. These simulations incorporate both the fundamental physics processes governing particle interactions and the detailed response of the experimental apparatus. This includes modeling aspects such as parton-level interactions, hadronization, and decay chains, as well as the geometry, material composition, and signal readout mechanisms of the detector.

There are several steps involved in the MC production. The process starts with event generation, followed by the simulation of the detector response. This is succeeded by the digitization phase, which mimics the detector's electronic readout, and concludes with the reconstruction of the simulated signals into high-level physics objects.

Event generation, which creates the sets of particle four-momenta, is the first step in MC production chain. A crucial function of the event generator is the modeling of prompt decays of intermediate particles, such as the Z and W bosons. Furthermore, the generator determines which particles are considered "stable" for the purposes of detector simulation. In this context, stability refers to particles with lifetimes long enough to traverse part or all of the detector volume before decaying. These stable particles are essential for experimental observations, as they deposit measurable energy or leave detectable tracks in the various sub detectors. Pythia [50] and Herwig [51] are the examples of general purpose MC event generators capable of simulating high-energy collisions involving protons, electrons, photons, or heavy ions. Other event generators include Sherpa [52, 53], MadGraph [54], MC@NLO [55], POWHEG [56]. For this thesis, Sherpa is used to integrate matrix element calculations with parton showers, hadronization, and decays, making it suitable for both inclusive and exclusive final state modeling.

The subsequent phase in the MC simulation workflow is the **detector simulation**, which models how the generated particles interact with the physical components of the detector. This simulation can be carried out in two ways. In a fast simulation, a simplified parametric approach is adopted to model the calorimeter shower, where the detector response to particles is approximated using smearing functions based on expected resolutions. In contrast, full simulation employs a detailed particle transport algorithm, in which the trajectory and interactions of each particle with the detector materials are modeled with high precision, including electromagnetic and hadronic processes. Interactions that occur within active components of the detector result in the production of hits, which correspond to localized energy deposits or ionization signals.

After the detector simulation has generated hits resulting from particle interactions with the detector elements, these hits must be further processed to emulate the output that would be produced by the real detector's readout electronics. This stage is referred to as **digitization**. Digitization mimics the electronic response of the detector. It includes effects like signal collection, pulse shaping, and electronic readout. Each sub-detector has its own specific digitization model. Regardless of sub-detector type, digitization must also account for electronic noise, channel masking and event pileup. The output of this step is Raw Data Object (RDO) files, which look like raw data from the real detector.

The **reconstruction** phase transforms the digitized output into physics objects suitable for analysis. This stage involves algorithms for local pattern recognition, track and vertex reconstruction, calorimeter clustering, and the identification of composite objects such as jets, electrons, and muons. The reconstruction procedure is largely identical for both real and simulated data, ensuring consistency in the analysis. The primary distinction is the availability of truth information in simulated samples. During event generation, this includes the complete interaction history and the list of generated particles. During detector simulation, it extends to include truth-level trajectories and decay information for select particles. As part of the digitization step, Simulated Data Objects (SDOs) are generated to link detector hits to the corresponding truth-level particles. This allows a detailed understanding of the energy deposition by individual simulated particles in calorimeters.

MC simulations in Drell–Yan $\rightarrow e^+e^- + jets$ are used for the derivation of electron charge misidentified probabilities and scale factors in this thesis. The generated signal and background events were processed through the full ATLAS detector simulation based on GEANT4 [57]. The list of MC samples used in the thesis is given in the Table 4.2. Dedicated MC campaigns are developed to accurately emulate the detector conditions corresponding to different periods of data collection. These campaigns are labeled as *mc20a*, *mc20d*, *mc20e*, *mc23a*, and *mc23d*, corresponding to the 2015–2016, 2017, 2018, 2022, and 2023 data-taking periods, respectively.

Table 4.2: List of MC samples used in the analysis.

MC campaign	MC sample
mc20a	mc20_13TeV.700320.Sh_2211_Zee_maxHTpTV2_BFilter.deriv.DAOD_PHYS.e8351_s3681_r13167_p6490
	mc20_13TeV.700321.Sh_2211_Zee_maxHTpTV2_CFilterBVeto.deriv.DAOD_PHYS.e8351_s3681_r13167_p6490
	mc20_13TeV.700322.Sh_2211_Zee_maxHTpTV2_CVetoBVeto.deriv.DAOD_PHYS.e8351_s3681_r13167_p6490
mc20d	mc20_13TeV.700320.Sh_2211_Zee_maxHTpTV2_BFilter.deriv.DAOD_PHYS.e8351_s3681_r13144_p6490
	mc20_13TeV.700321.Sh_2211_Zee_maxHTpTV2_CFilterBVeto.deriv.DAOD_PHYS.e8351_s3681_r13144_p6490
	mc20_13TeV.700322.Sh_2211_Zee_maxHTpTV2_CVetoBVeto.deriv.DAOD_PHYS.e8351_s3681_r13144_p6490
mc20e	mc20_13TeV.700320.Sh_2211_Zee_maxHTpTV2_BFilter.deriv.DAOD_PHYS.e8351_s3681_r13145_p6490
	mc20_13TeV.700321.Sh_2211_Zee_maxHTpTV2_CFilterBVeto.deriv.DAOD_PHYS.e8351_s3681_r13145_p6490
	mc20_13TeV.700322.Sh_2211_Zee_maxHTpTV2_CVetoBVeto.deriv.DAOD_PHYS.e8351_s3681_r13145_p6490
mc23a	mc23_13p6TeV.700786.Sh_2214_Zee_maxHTpTV2_BFilter.deriv.DAOD_PHYS.e8514_s4162_r14622_p6491
	mc23_13p6TeV.700787.Sh_2214_Zee_maxHTpTV2_CFilterBVeto.deriv.DAOD_PHYS.e8514_s4162_r14622_p6491
	mc23_13p6TeV.700788.Sh_2214_Zee_maxHTpTV2_CVetoBVeto.deriv.DAOD_PHYS.e8514_s4162_r14622_p6491
mc23d	mc23_13p6TeV.700786.Sh_2214_Zee_maxHTpTV2_BFilter.deriv.DAOD_PHYS.e8514_s4159_r15224_p6491
	mc23_13p6TeV.700787.Sh_2214_Zee_maxHTpTV2_CFilterBVeto.deriv.DAOD_PHYS.e8514_s4159_r15224_p6491
	mc23_13p6TeV.700788.Sh_2214_Zee_maxHTpTV2_CVetoBVeto.deriv.DAOD_PHYS.e8514_s4159_r15224_p6491

The file naming convention of a MC sample is as follows:

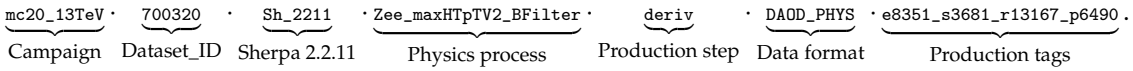

CHAPTER 5

Electron Object Definition and Selection

Electrons are essential objects in ATLAS physics analyses, including standard model measurements and new physics searches. Their accurate reconstruction and selection are crucial for ensuring reliable results. This chapter describes the methods used to reconstruct electrons from calorimeter and tracking information, the criteria applied for their identification using likelihood based or DNN algorithms, and isolation techniques. Additionally, it outlines the event level selection strategy, including kinematic thresholds and trigger matching.

5.1 Reconstruction

The reconstruction of electron objects in ATLAS begins with the identification of topological clusters (commonly called topo-clusters) formed from energy deposits in both the electromagnetic (EM) and hadronic calorimeters. These clusters are built using a dynamic-size algorithm that combines adjacent calorimeter cells based on topological energy patterns. To identify EM topo-clusters, the EM energy of each cluster is first calculated using only the energy from the cells in the EM calorimeter. A cluster is retained for further consideration if its EM energy exceeds 400 MeV and the ratio of its EM energy to the total energy (the sum of EM and hadronic components) is greater than 0.5 [58]. These EM topo-clusters serve as the basis for subsequent electron reconstruction. Simultaneously, tracks are reconstructed within the ID using the standard tracking algorithm [58], or, in some cases, an alternative tracking method that specifically accounts for energy losses from bremsstrahlung during track pattern recognition [59]. A sliding window algorithm is then applied to the EM calorimeter cells to loosely match the reconstructed tracks to the fixed-size calorimeter clusters. Once this initial match is made, the tracks are refitted using a gaussian sum filter algorithm, which enhances the precision of the reconstructed track parameters by accounting for non-Gaussian effects like bremsstrahlung.

To identify an electron, the reconstruction algorithm requires that at least one track from the inner detector is matched to EM topo-clusters. The specific details of this track-cluster matching algorithm and selection criteria can be found in Ref. [59]. These requirements may be satisfied by multiple tracks. The system selects the "best-matching" track based on detector conditions, such as the number of hits in the various inner detector layers. The track that shows the best geometric match (i.e., the smallest

angular distance ΔR) to the energy cluster in the second ECAL layer is selected as the best-matching track. The four-momentum of the reconstructed electron is calculated using both the topo-cluster and the matched track. The energy of the electron is taken from the cluster, while the angular coordinates (ϕ and η) are determined using the best-matched track at the interaction vertex. The electric charge of the electron is inferred from the curvature of this track. Following the identification of initial electron candidates, final EM clusters are formed by merging all nearby clusters associated with those candidates. When an electron undergoes bremsstrahlung radiation, it may appear as two distinct energy clusters in the calorimeter. This phenomenon affects roughly 10% of clusters, particularly in the forward and transition regions of the detector. To account for this, the reconstruction algorithm merges nearby EM topo-clusters into a single, final cluster, which is often referred to as a supercluster. After applying position corrections and calibrating the energy of these final clusters, the track matching is repeated to complete the electron reconstruction, using the calibration procedures described in the Ref. [60]. The energy calibration scheme for electrons is based on a simulation-driven optimization of the energy resolution, ensuring precise reconstruction performance. Corrections are applied to account for discrepancies between real data and simulation. The absolute energy scale is then calibrated using $Z \to e^+e^-$ events and finally, the universality of the calibrated energy scale across different kinematic regions and energy ranges is validated using J/ψ events.

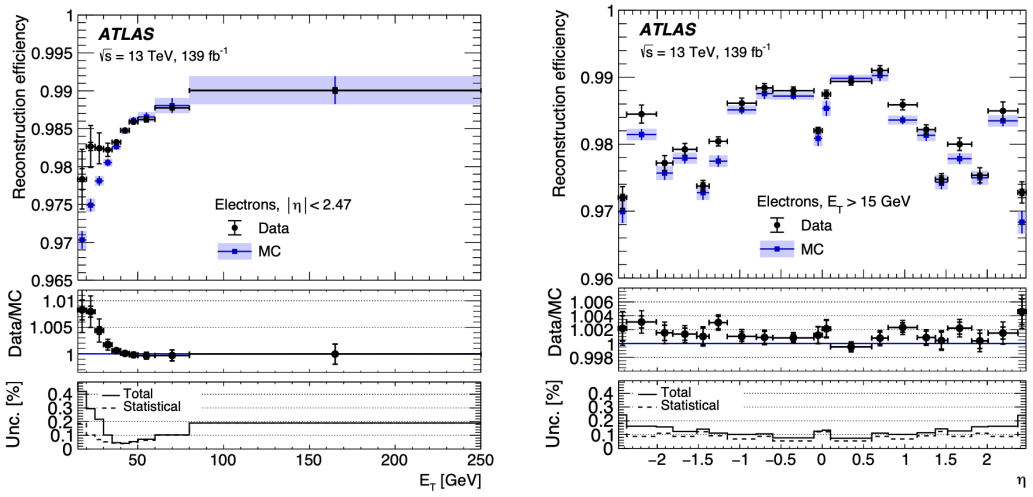

(a) **(b)**

Figure 5.1: Electron reconstruction efficiencies derived from $Z \to e^+e^-$ decays presented as a function of the electron E_T (a)and $|\eta|$ (b) respectively. The top panels display the efficiencies measured in data and simulation, with inner and outer error bars representing the statistical and total uncertainties, respectively. The middle panels show the ratio of the efficiencies in data to those in simulation, which is used as a correction factor. The bottom panels illustrate the relative statistical and total uncertainties associated with the data/MC ratio. Plots are taken from Ref. [61].

The reconstruction efficiency, denoted as ϵ_{reco}, quantifies how effectively tracks are reconstructed and matched to electromagnetic clusters. It is defined as the ratio of the number of reconstructed

electron candidates with an associated track, N_{reco}, to the total number of electromagnetic cluster candidates, $N_{cluster}$. The electron reconstruction efficiency is measured only for $E_T > 15\ GeV$ using a tag-and-probe method based on the $Z \to e^+e^-$ invariant mass as described in Ref. [62], as the presence of significant backgrounds below this threshold renders the measurement unreliable. Furthermore, alternative approaches using low-mass resonances such as the J/ψ are also challenging in this energy regime. Electron reconstruction efficiencies corresponding to the kinematics of simulated $Z \to e^+e^-$ events are shown in Figure 5.1 as a function of the electron transverse energy and pseudorapidity, respectively. The electron reconstruction efficiency is very high with values between 98-99%; however, it drops at higher $|\eta|$ and in the calorimeter transition region. The correction factors, defined as the ratio of reconstruction efficiencies in data to those in simulation, are shown in the middle panels of the figures. The systematic uncertainties on the correction factors are less than 0.5% over most of the kinematic range and less than 0.1% for $E_T > 30$ GeV [61].

5.2 Identification

Electron identification plays a vital role in distinguishing genuine electrons from background processes that can mimic similar signatures in the detector. While the reconstruction algorithms are designed to associate energy clusters in the electromagnetic calorimeter with charged particle tracks, they do not inherently reject backgrounds such as hadronic jets, photon conversions, or electrons originating from heavy-flavor decays. To suppress these background contributions, dedicated electron identification criteria are applied. These criteria utilize detailed information from shower shapes in the calorimeter, track properties, and track–cluster matching variables. Two main approaches are employed in ATLAS: the traditional likelihood (LH) based identification and the more recent Deep Neural Network (DNN) identification, both of which aim to maximize the efficiency of true electron selection while minimizing contamination from background sources.

In MC simulations, various types of particles originating from different physical processes can produce detector signatures that closely resemble those of prompt electrons. As a result, these background particles can be mistakenly reconstructed as electrons. The effectiveness of any electron identification algorithm can vary significantly depending on the type of background particle being considered. To address this, different categories of reconstructed electron-like objects are defined, each corresponding to a distinct source or physical origin at the MC truth level. These categories, along with their definitions and the simulation samples used to study them, are summarized in Table 1 of Ref. [63]. In this context, the term "Signal" specifically refers to prompt electrons, meaning those directly produced in electroweak decays such as from $Z \to e^+e^-$, $W \to e\nu$ and $H \to ZZ^* \to 4l$.

A particular subset of prompt electrons, known as charge-flip electrons, arises when the reconstruction algorithms assign the wrong electric charge to an otherwise genuine electron. Whether such electrons are considered signal or background depends on the specific physics analysis. For example, analyses focused on same-sign dilepton final states must treat charge-flip electrons as background, since they can fake the signature of two same-charge leptons from a Drell–Yan process, which naturally produces opposite-charge leptons. The incorrect reconstruction of charge in such cases inflates

the background due to the Drell–Yan process's high production cross-section. Therefore, rejecting charge-flip electrons is essential to suppress this contribution.

Conversely, in analyses with a single-lepton final state that do not depend on the sign of the charge, charge-flip electrons can be accepted as part of the signal, thereby improving selection efficiency. The remaining four categories: electrons from photon conversions, from heavy-flavor quark decays, from light-flavor hadron decays, and light-flavor hadrons are all regarded as background sources and must be suppressed through stringent identification criteria.

5.2.1 Likelihood Identification

Prompt electrons entering the central region of the detector ($|\eta| < 2.47$) are identified using a LH based identification algorithm. The inputs to the LH include measurements from the tracking system, the calorimeter system, and quantities that combine both tracking and calorimeter information. The specific inputs are described in Table 1 of Ref. [59]. In the likelihood-based identification approach, one-dimensional probability density functions (PDFs) are independently constructed for each input variable, treating signal and background samples separately and ignoring variable correlations. For a given electron candidate, the likelihood of being signal (L_S) or background (L_B) is computed by multiplying the corresponding PDFs of all input variables:

$$L_{S(B)}(\mathbf{x}) = \prod_i P_{S(B),i}(x_i), \tag{5.1}$$

where $\mathbf{x}$ is the vector of various quantities described in Table 1 of Ref. [59], $P_{S,i}(x_i)$ is the signal PDF for ith quantity at x_i, and $P_{B,i}(x_i)$ is the background PDF for ith quantity at x_i. The signal is prompt electrons, while the background is the combination of jets that mimic the signature of prompt electrons, electrons from photon conversions in the detector material, and non-prompt electrons from the decay of hadrons containing heavy flavors. Using these likelihoods, the discriminant d_L is calculated as:

$$d_L = \frac{L_S}{L_S + L_B}. \tag{5.2}$$

Electron identification relies on a discriminant d_L, which effectively separates signal from background. This discriminant tends to cluster sharply, approaching 1 for signal electrons and 0 for background, making it challenging to define selection thresholds without using very fine binning [59]. To overcome this limitation, an inverse sigmoid transformation is applied to d_L, producing a new discriminant d'_L given by:

$$d'_L = -\frac{1}{\tau} \ln\left(\frac{1}{d_L} - 1\right), \tag{5.3}$$

with the scaling parameter τ fixed at 15 [64]. This transformation spreads out the discriminant values, making them more suitable for defining practical operating points. Electron candidates with a d'_L value exceeding a defined threshold are then classified as signal, depending on the chosen identification working point.

To meet the diverse requirements of physics analyses in ATLAS, ranging from those favoring high signal efficiency to those needing strong background suppression, four fixed thresholds of the likelihood discriminant are used to define standard identification levels. These levels, known as VeryLoose, Loose, LooseBLayer (additional cut on number of hits in the b-layer of the pixel detector), Medium, and Tight, represent increasing levels of stringency. Each corresponds to a progressively higher threshold on the LH discriminant, d_L', which is determined based on MC simulations. These operating points allow analyses to balance electron selection efficiency against background rejection according to their specific goals. In this thesis, only three of the standard operating points: Loose, Medium, and Tight are used for the electron identification. The Loose working point offers the highest signal efficiency but provides the least background rejection, while the Tight working point achieves the strongest background suppression at the cost of reduced signal efficiency. The identification efficiency, ϵ_{id}, is the probability of a reconstructed electron to satisfy a certain identification criterion. It is defined as the number of identified and reconstructed electron candidates, N_{id}, divided by N_{reco}. The PDFs for the E_T range of 4.5 GeV to 20 GeV are determined using $J/\psi \to ee$ MC simulation and the PDFs for E_T >15 GeV are determined using $Z \to e^+e^-$ MC simulation. The $J/\psi \to ee$ measurement determines the

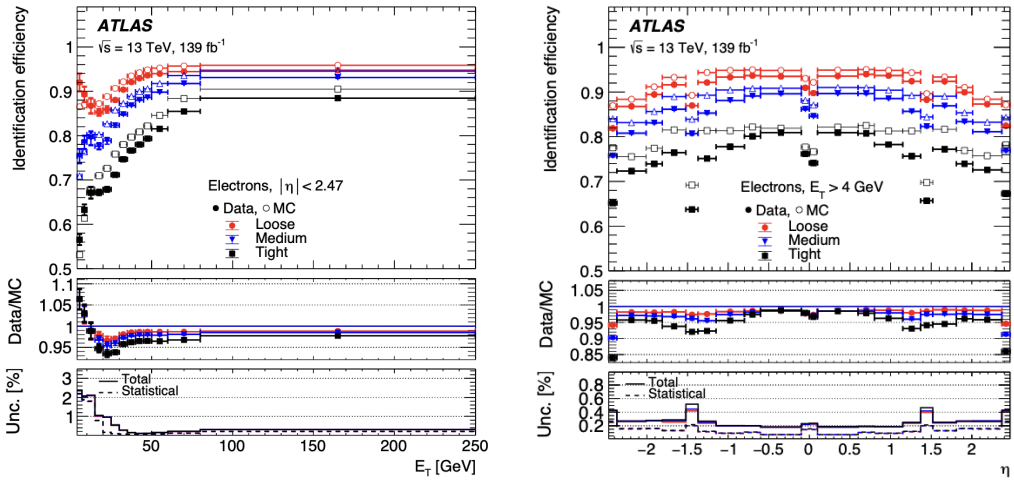

(a) **(b)**

Figure 5.2: Electron identification efficiencies for various working points. The electron identification efficiency is measured as a function of the electron's (a) transverse energy E_T and (b) pseudorapidity η for the three main electron identification working points. The top panels display the efficiencies measured in data and simulation, with inner and outer error bars representing the statistical and total uncertainties, respectively. The middle panels show the ratio of the efficiencies in data to those in simulation, which is used as a correction factor. The bottom panels illustrate the relative statistical and total uncertainties associated with the data/MC ratio. Plots are taken from Ref. [61].

electron identification efficiency by using the invariant mass of the two electron candidates. In contrast, the $Z \to e^+e^-$ measurement uses either the invariant mass of the electron pair (Z-mass method) or the amount of transverse energy deposited within an isolation cone surrounding the probe elec-

tron (Z-isolation method). The details of these methods can be found in Ref. [61]. The identification efficiencies corresponding to different working points are presented in Figure 5.2(a) as a function of transverse energy E_T, and in Figure 5.2(b) as a function of η. As we can see from the plots, the efficiencies for identifying a prompt electron with $E_T \simeq 40$ GeV are 93%, 88%, and 80% for the Loose, Medium, and Tight operating points, respectively.

5.2.2 *Identification using Deep Neural Network*

This section describes the Deep Neural Network (DNN) based electron identification approach, which provides improved performance compared to the traditional LH method. Table 2 in Ref. [63] lists all input variables used in the DNN, which contain information from the tracking detectors, calorimeter systems, and the matching between reconstructed tracks and energy clusters in the calorimeter. The variables are specifically chosen to maximize discrimination between electrons and various background components. While similar in purpose, the set of input variables used in the DNN differs slightly from those employed in the LH method [59]. For example, the transverse energy E_T and the $|\eta|$ are included as direct inputs to the DNN to allow the network to learn a parameterized response over these variables. In contrast, these quantities cannot be used directly in the LH method. Instead, separate LH models are constructed in bins of E_T and $|\eta|$, thereby incorporating this dependence indirectly. Another important distinction lies in the treatment of variable correlations. The DNN can accept input variables that are correlated, whereas the LH method requires uncorrelated inputs, as it is based on a product of one-dimensional PDFs. For instance, both R_{had} [1] and R_{had1} [2], which are highly correlated, can be simultaneously included as inputs to the DNN across the entire $|\eta|$ range. In contrast, the LH approach uses only one of them depending on the candidate's $|\eta|$, based on detector geometry. Specifically, in regions where the first layer of the hadronic calorimeter is absent, R_{had} is used; elsewhere, $R_{had1}$is preferred due to its lower noise. It should also be noted that the final decision on whether an electron candidate passes a given working point is not solely based on the DNN output. Additional selection criteria such as requirements on the number of hits in specific sub-detectors and the ambiguity classification are also applied. These additional requirements are identical to those used in the LH method. For DNN training and evaluation, $Z \to ee$, $J/\psi \to ee$ and JF17 [3] samples are used. The details on DNN training procedure can be found in Ref. [63]. The performance of the DNN model is based on the value of discriminant $\mathcal{D}_{el}$ defined in Equation 1 of Ref. [63].

To assess the classification performance of the DNN relative to the LH method, Receiver Operating Characteristic (ROC) curves are employed. These curves are obtained by scanning the DNN discriminant output over a range of threshold values τ, and computing the corresponding signal efficiency and background rejection at each point. The signal efficiency is defined as the fraction of signal electrons that have a DNN output value $\mathcal{D}_{el} > \tau$, relative to the total number of signal electrons. Conversely,

[1] R_{had} quantifies the total transverse energy leakage into the hadronic calorimeter relative to the EM cluster's transverse energy.
[2] R_{had1} quantifies the fraction of transverse energy in the first layer of the hadronic calorimeter relative to the EM cluster's transverse energy.
[3] The JF17 sample consists of multijet production, $qg \to q\gamma$, $q\bar{q} \to g\gamma$, and W and Z production and top quark production selected by requiring a localised transverse energy deposit above 17 GeV within a $\Delta\eta \times \Delta\phi$ window of 0.1×0.1, to enhance backgrounds that mimic prompt electrons.

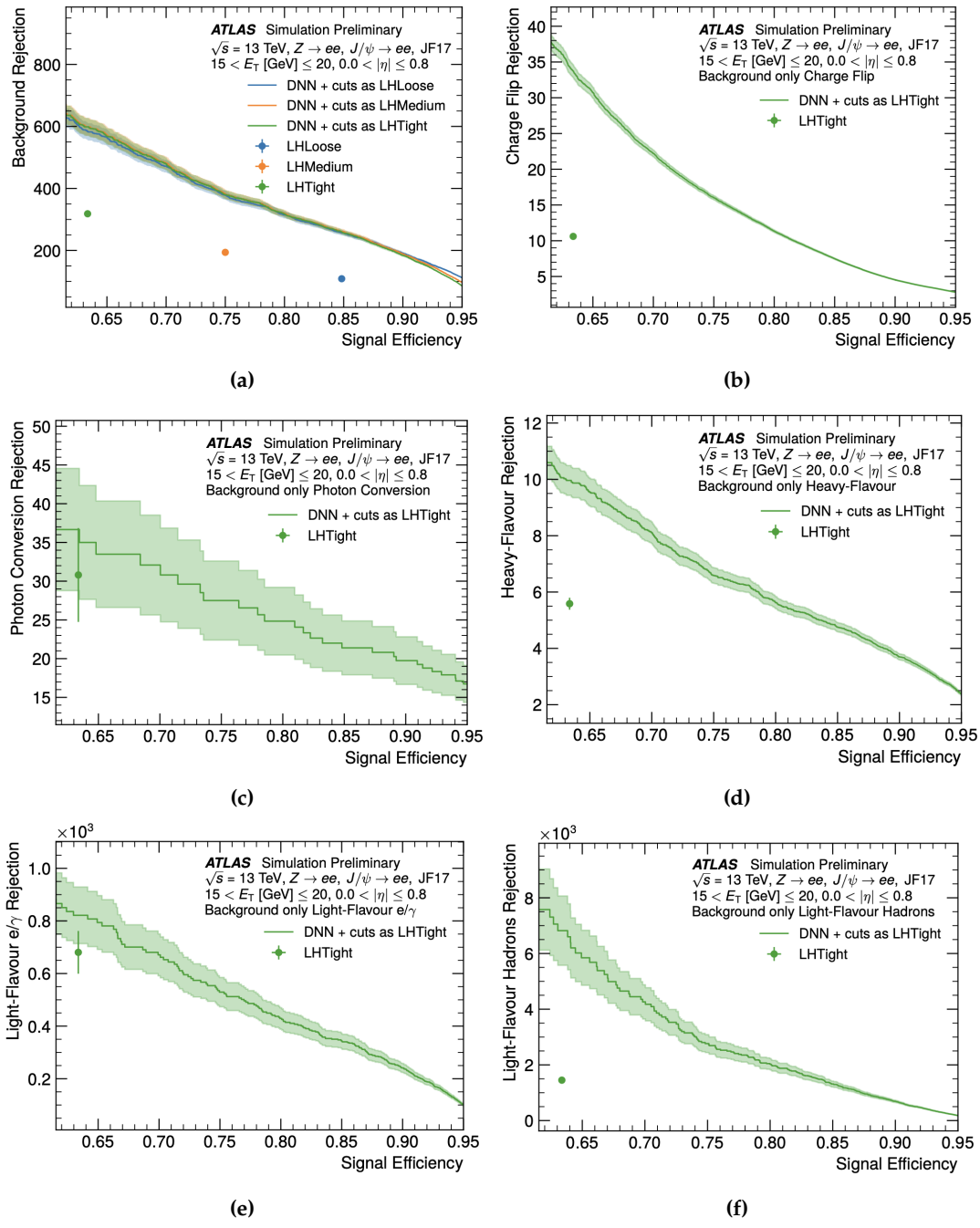

Figure 5.3: ROC curves for combined and different backgrounds. (a) Combined background, (b) only charge flip electrons, (c) only electrons from photon conversions (d) only electrons from heavy-flavour quark decays, (e) only electrons and photons from light-flavour hadrons, and (f) only light-flavour hadrons. The plots include only candidates with $15 < E_T$ [GeV] ≤ 20 and $|\eta| \leq 0.8$. Plots are taken from Ref. [63].

the background rejection is calculated as the inverse of the background efficiency, which is the ratio of background electrons with $\mathcal{D}_{el} > \tau$ to the total number of background electrons. Figure 5.3 shows the ROC curves in one $(E_T, |\eta|)$ bin for the combined background and for the single background classes separately.

As illustrated in Figure 5.3(a), the DNN achieves significantly improved background rejection compared to the combined background rejection performance of the LH method. At the signal efficiency corresponding to the Tight LH working point, the DNN increases background rejection by approximately a factor of two. This performance gain becomes even more pronounced at higher signal efficiencies. Figure 5.3(b) presents the rejection of charge-flip electrons. Since these electrons originate from prompt sources but are reconstructed with the incorrect charge, they are treated as signal and should ideally not be rejected. The DNN, however, rejects a greater fraction of charge-flip electrons than the LH, resulting in lower acceptance for this category. Despite this, the overall impact on signal efficiency remains negligible due to the relatively large number of correctly reconstructed prompt electrons present in data. Figures 5.3(c)-5.3(f) display the rejection performance for individual background sources. In all cases, the DNN outperforms the LH in rejecting background electrons. However, the degree of improvement varies across the different background components.

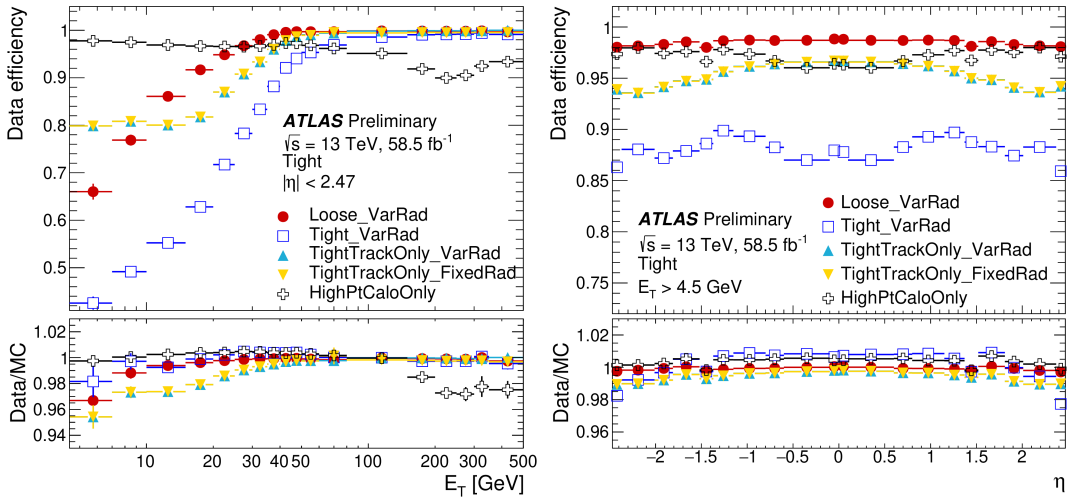

(a) (b)

Figure 5.4: Isolation efficiency in data 2018 with different isolation working points for electrons in $Z \to e^+e^-$ events as a function of the (a) E_T and (b) $|\eta|$. The lower panel shows the ratio of the efficiencies measured in data and in MC simulations. The total uncertainties are shown, including the statistical and systematic components. Plots are taken from Ref. [65].

5.3 Isolation

In addition to the electron identification working points, isolation criteria are applied to further suppress contributions from fake or non-prompt electrons. Within the ATLAS Collaboration, five isolation

working points are officially recommended: HighPtCaloOnly, TightTrackOnly_VarRad, TightTrackOnly_FixedRad, Tight_VarRad, and Loose_VarRad. These working points are designed to optimize the balance between maintaining high efficiency for selecting prompt electrons regardless of whether they are in isolated or densely populated environments and achieving effective rejection of background electrons that originate from non-prompt sources or detector related fakes. Two sets of isolation variables are used, calorimeter-based isolation and track-based isolation [59]. The definition of the electron isolation criteria can be found in the Table 2 of the Ref. [61]. The isolation efficiency, ϵ_{iso}, is the probability of an identified electron to pass requirements on the track or calorimeter isolation. It is calculated as the number of identified electron candidates satisfying the isolation, identification, and reconstruction requirements, N_{iso}, divided by N_{id}. Figure 5.4, shows the electron isolation efficiency for all five isolation working points, when the electrons are selected with the Tight identification working point. As we can see from the plots, Tight_VarRad has the lowest isolation efficiency for signal electrons, reflecting its stricter isolation criteria below 60 GeV.

5.4 Object Selection

In this section, the selection criteria for all the different objects used in the measurement of charge misidentified scale factors using $Z \to e^+e^-$ is presented.

5.4.1 Electrons

Table 5.1 lists the requirements for signal and baseline electrons.

Table 5.1: Electron selection requirements.

Requirement	**Baseline**	**Signal**
p_T	> 4.5 GeV	> 4.5 GeV
$\|\eta\|$	< 2.47	< 2.47
Identification	`TightLH`	`TightLH`
Isolation	No isolation	`Tight_VarRad`
Crack veto	veto $1.37 < \|\eta\| < 1.52$	veto $1.37 < \|\eta\| < 1.52$
$\|d_0\|/\sigma_{d_0}$	-	< 5.0
$\|z_0 \sin\theta\|$	< 0.5 mm	< 0.5 mm

Baseline electrons are a broad selection of electron candidates that satisfy minimal quality criteria. They are used for calculating object multiplicities (e.g., number of electrons in the event), overlap removal with other objects (e.g., muons, jets) and forming initial event pre-selection. *Signal electrons* are a subset of baseline electrons that pass stricter selections, suitable for physics analysis.

The crack veto refers to the requirement that electrons must not fall within the η region $1.37 < |\eta| < 1.52$, known as the crack region of the ECAL. This region contains services and infrastructure for the ID and lacks sufficient active calorimeter material, resulting in reduced measurement performance. The transverse impact parameter, d_0, is defined as the minimum distance between a particle's trajectory

and the beam collision point in the plane transverse to the beam direction, with σ_{d_0} representing its associated measurement uncertainty. The longitudinal impact parameter, z_0, measures the distance along the beam axis between the primary vertex and the point where the transverse impact parameter, d_0, is calculated. The product $z_0 \sin\theta$ gives the transverse component of z_0 and indicates the extent to which the particle's path deviates from an ideal longitudinal trajectory.

Also, electron calibration `es2023_R22_Run2_v1` is used for Run 2, while `es2024_Run3_v0` is applied for Run 3 data. For this thesis, three identification working points are used: Tight, Medium, and Loose with isolation working point of Tight_VarRad for signal electrons.

5.4.2 *Trigger Selection*

A set of single-electron triggers defined for each data-taking year is shown in Table 5.2, combined using a logical `OR` condition. All triggers listed in the table are unprescaled [4].

Table 5.2: Unprescaled single electron trigger for each data-taking year.

Year	Trigger
2015	`HLT_e24_lhmedium_L1EM20VH`
	`HLT_e60_lhmedium`
	`HLT_e120_lhloose`
2016-2018	`HLT_e26_lhtight_nod0_ivarloose`
	`HLT_e60_lhmedium_nod0`
	`HLT_e140_lhloose_nod0`
2022-2024	`HLT_e26_lhtight_ivarloose_L1eEM26M`
	`HLT_e60_lhmedium_L1eEM26M`
	`HLT_e140_lhloose_L1eEM26M`

The trigger name typically encodes the specific selection criteria applied by the trigger itself. This includes the trigger level (e.g., HLT or L1), kinematic thresholds, identification and isolation criteria. For instance, the trigger `HLT_e60_lhmedium_nod0` refers to a HLT that selects events containing atleast one electron with transverse momentum $p_T > 60$ GeV, passing the medium LH identification, and without any constraint on the transverse impact parameter d_0.

5.4.3 *Muons*

Table 5.3 lists the requirements for signal and baseline muons. Muons are included in the selection criteria only as a veto. The event selection explicitly requires exactly two signal electrons and rejects any event containing additional baseline electrons or any baseline muons. This muon veto suppresses contamination from processes such as WZ production, which can yield final states with two electrons and an additional muon.

[4] A prescale factor, denoted by N, determines the fraction of events passing a trigger that are recorded for analysis. A prescale of $N > 1$ means that only one out of every N events is retained, whereas $N = 1$ corresponds to an unprescaled trigger where all accepted events are saved. Prescaling is employed to manage limited computing resources and optimize data acquisition efficiency.

Table 5.3: Muon selection requirements.

Requirement	**Baseline**	**Signal**
p_T	> 3.0 GeV	> 3.0 GeV
$\|\eta\|$	< 2.5	< 2.5
Identification	`Medium`	`Medium`
Isolation	No isolation	`PflowTight_VarRad`
$\|d_0\|/\sigma_{d_0}$	-	< 3.0
$\|z_0 \sin\theta\|$	< 0.5 mm	< 0.5 mm

CHAPTER 6

Electron Charge Misidentification

In ATLAS, the accurate reconstruction of particle properties, including electric charge, is fundamental to performing precise measurements and searches for new physics. While the charge of most particles is reliably determined, electrons are particularly susceptible to charge misidentification, an effect where the reconstructed charge does not correspond to the true charge of the particle. This phenomenon becomes especially critical in analyses that rely on final states with same-sign electron pairs, such as searches for rare processes or physics beyond the SM. In such cases, a standard background process like $Z \rightarrow e^+e^- + jets$ can fake a signal if one of the electron charges is incorrectly measured. Therefore, charge misidentification can introduce a non-negligible and irreducible background if not properly accounted for. This chapter provides a detailed overview of the phenomenon of electron charge misidentification. It begins with a formal definition, followed by a discussion of the primary sources contributing to this effect in the ATLAS detector.

6.1 Definition

Charge misidentification constitutes a significant background in analyses involving two same-sign leptons, particularly when electrons are present in the final state. In such events, electrons that are originally produced with opposite charges can be incorrectly reconstructed as having the same charge due to detector-related effects. These charge misidentified electrons, also referred to as **charge flip** electrons, can lead to false-positive signatures that mimic genuine same-sign lepton signals, thereby contaminating the measurement of rare processes or searches for new physics phenomena. Accurately modeling and correcting for this background is thus essential to ensure the integrity of the analysis.

We focus specifically on electrons for the study of charge misidentification, although it is possible for muons to also undergo charge misidentification. The determination of the muon charge relies on track curvature measurements obtained from the inner detector and the muon spectrometer, significantly enhancing the precision of the curvature and charge determination. Furthermore, due to their relatively larger mass, muons are much less susceptible to bremsstrahlung radiation compared to electrons. As a result, the muon charge misidentification rate is considered negligible.

6.2 Sources of Electron Charge Misidentification

As an electron moves through the material of the detector, it can emit photons via the bremsstrahlung process. These photons may subsequently convert into electron–positron pairs, resulting in the production of secondary charged particles close to the original electron trajectory. The presence of these secondaries can interfere with the accurate reconstruction of the electron's track. In some cases, hits from these nearby particles are mistakenly included in the fit of the primary electron's track, distorting the measurement of its curvature and potentially leading to an incorrect determination of its charge. In other situations, the reconstruction algorithm may incorrectly associate the track of one of these secondary particles with the electron, particularly in high-density environments. Even though the curvature of this incorrectly selected track may be determined correctly, it does not correspond to the true electron. These two scenarios lead to charge misidentification and are commonly referred to as **type-2** and **type-4** charge flip electrons, depending on whether the issue arises from a distortion in curvature or the misassociation of tracks, respectively.

6.2.1 Type-2 Charge Flip Electrons

This type of charge flip electrons result from an inaccurate measurement of the curvature of an electron's track within the inner detector. When a charged particle propagates through a uniform magnetic field $\vec{B}$ with its velocity vector $\vec{v}$ perpendicular to the field direction, its trajectory bends in a circular arc. The radius of this curvature ($R \propto \frac{p_T}{Q}$) is directly proportional to the particle's transverse momentum p_T and inversely proportional to its electric charge Q. For a fixed magnetic field strength, electrons with high-p_T, the curvature is small (nearly straight), making it harder to determine whether the trajectory curves "left" or "right", i.e., what the sign of the charge is.

This issue is particularly pronounced in the forward regions of the detector (at high values of η), where the quality of tracking information is degraded. For example, in the end-cap region of the Transition Radiation Tracker (TRT), tracking coverage becomes limited for particles with $|\eta| > 2.0$, reducing the number of hits available for curvature fitting. Additionally, in the forward direction, particles tend to travel nearly parallel to the magnetic field lines, making their tracks inherently less bent and harder to measure accurately. As illustrated in Figure 6.1, a prompt electron with high transverse momentum follows a trajectory that is only slightly curved (shown in blue) and deposits energy in the electromagnetic calorimeter (orange region). While the calorimeter correctly associates this deposit with the true generated electron (green), the reconstructed track, shown as a dashed line, has insufficient curvature and poor fit quality. This leads to an erroneous estimate of the track's bending direction and, consequently, to an incorrect assignment of the particle's electric charge.

6.2.2 Type-4 Charge Flip Electrons

Figure 6.2 illustrates the mechanism by which an electron's charge can be misidentified as a consequence of bremsstrahlung radiation and subsequent photon conversions. The process begins with an electron originating from the physics event of interest which is denoted as the generated electron

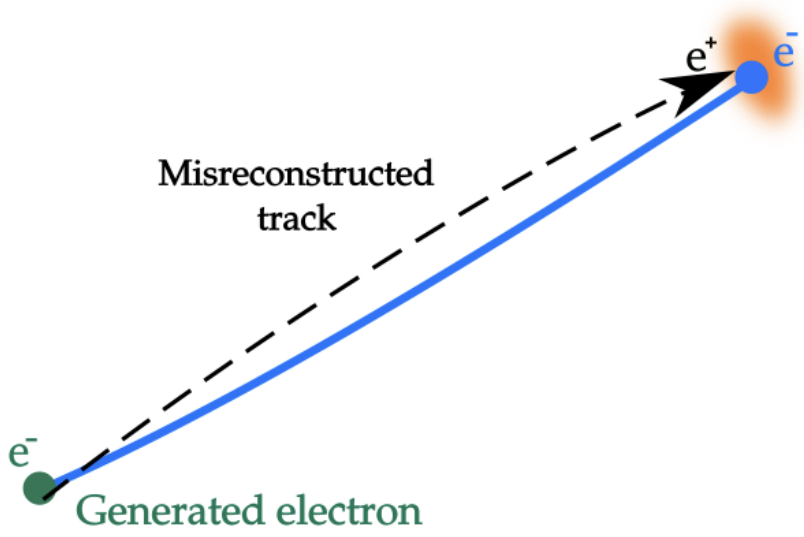

Figure 6.1: Type-2 charge flip electrons. Track misreconstruction at high p_T. Figure is taken from Ref. [66].

(shown in green on the left). This prompt electron then enters the detector volume, and its trajectory is shown as a solid blue line.

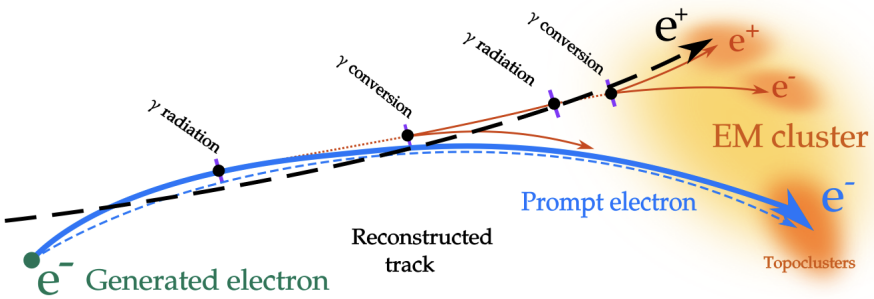

Figure 6.2: Type-4 charge flip electrons.. A generated electron (green) emits bremsstrahlung photons as it traverses the detector material. These photons undergo conversions, producing secondary electron–positron pairs. Energy from the resulting electromagnetic shower is deposited in the EM calorimeter (orange cluster). Multiple tracks are reconstructed from hits in the inner detector and associated with the calorimeter cluster. If the track from a secondary particle (e.g., a positron) is selected, such as one with higher transverse momentum, the reconstructed electron charge may be incorrect, resulting in a charge-flip electron. Figure is taken from Ref. [66].

As the prompt electron propagates through the detector region (with detector material indicated by the small lilac bars), interaction takes place and it emits bremsstrahlung photons. These photons,

in turn, can convert into secondary electron–positron pairs. The locations of these interactions are marked by black points along the trajectory. The ensemble of particles produced through this electromagnetic cascade eventually deposits energy in the ECAL, forming a spread-out cluster of energy represented by the orange shaded region. This cluster, or topocluster, reflects the total electromagnetic energy measured in the calorimeter, primarily stemming from the initial prompt electron and its radiated products. In the reconstruction phase, multiple track candidates are associated with the same EM cluster. These tracks include not only the prompt electron's original trajectory but also those from secondary particles created through photon conversions. Figure 6.2 shows one possible wrong track (the dashed black arrow ending at the e^+). The final electron candidate is selected by associating the EM cluster with one of these tracks based on specific criteria such as selecting the track with the highest transverse momentum. However, if the chosen track corresponds to a secondary electron or positron rather than the original electron, the inferred charge of the electron will be incorrect. This results in a charge misidentification, where a true negatively charged electron is reconstructed as a positively charged one (as indicated by the black e^+ in the figure).

In the nutshell, type-4 charge flip electrons are electrons from photon conversions and have an opposite charge compared to the true charge. These are very similar to brem electrons which originate from photon conversions of bremsstrahlung photons and which have the same truth signature but correctly reconstructed charge.

6.3 Final State Radiation

Electrons may also radiate photons through the process of Final State Radiation (FSR), which can mimic the topology of charge-flip scenarios, particularly those resembling type-4 electrons. This process is illustrated in Figure 6.3, where a quark–antiquark pair annihilates into a virtual boson (Z/γ^*), which subsequently decays into a pair of charged leptons. One of these leptons (e^- or μ^-) may emit a photon in the final state but we are considering only electrons for this thesis.

If this FSR photon subsequently interacts with the detector material and converts into an electron-positron pair, the resulting final state includes an additional lepton of opposite charge. Such events can resemble true charge misidentification, as the detector may reconstruct an apparent charge flip if the conversion electron is incorrectly matched. However, in this case, the original lepton's charge remains correctly reconstructed, and the extra track arises from a genuine physical process, not from an error in track reconstruction. For this reason, FSR is treated as a separate background rather than as a source of charge misidentification.

6.4 Electron Truth Classification

Truth level classification is essential for studying electron charge misidentification in MC simulations. Since charge misidentification is defined as a purely detector-induced effect, it must not originate from the event generator itself. However, MC samples often include other processes that can closely resemble charge flips, such as photon conversions or FSR, which complicate the identification of true

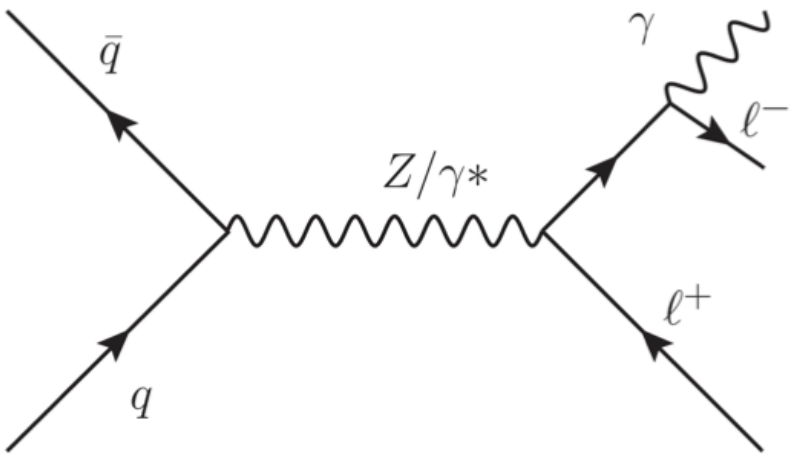

Figure 6.3: Feynman diagram illustrating FSR from an electron. A quark–antiquark pair annihilates into a virtual photon or Z boson, which subsequently decays into a pair of leptons.

misidentified events. To properly distinguish genuine charge misidentification, it is necessary to compare the true charge of the electron (i.e., the charge of the generated particle) with the reconstructed charge, which is determined by the curvature of the matched track in the inner detector. Discrepancies between these two charges may indicate a charge-flip event. However, care must be taken to separate this from other processes such as hard FSR photons converting into e^+e^- pairs that can produce final states similar to misidentified electrons.

In this study, the `MCTruthClassifier` [68] tool is employed to aid in this classification. It assigns each electron a set of identifiers: `TruthType`, which classifies the nature of the electron (e.g. prompt or from conversions) and `TruthOrigin`, which encodes the source of the particle (e.g. from a Z boson, photon, or meson decay). To ensure a reliable match, the *TruthMatchProbability* is computed as the ratio of hits in the inner detector (ID) caused by the truth electron to the total number of hits used in reconstructing the track. Furthermore, hits are weighted depending on the position in the detector; pixel hits are weighted with a factor of 10, SCT hits with a factor of 5, and TRT hits with a factor of 1. The truth electron with the largest truth match probability is than matched to the reconstructed electron [67]. However, truth matching based solely on proximity and hit contribution is insufficient when assessing charge accuracy. This is because the matched truth particle may itself be a secondary electron produced from bremsstrahlung photons followed by pair production, rather than the original prompt electron. In such cases, comparing the reconstructed and truth charge becomes misleading, as it does not reflect the charge of the true originating electron.

To resolve this, a consistent definition is adopted by tracing each matched truth electron back

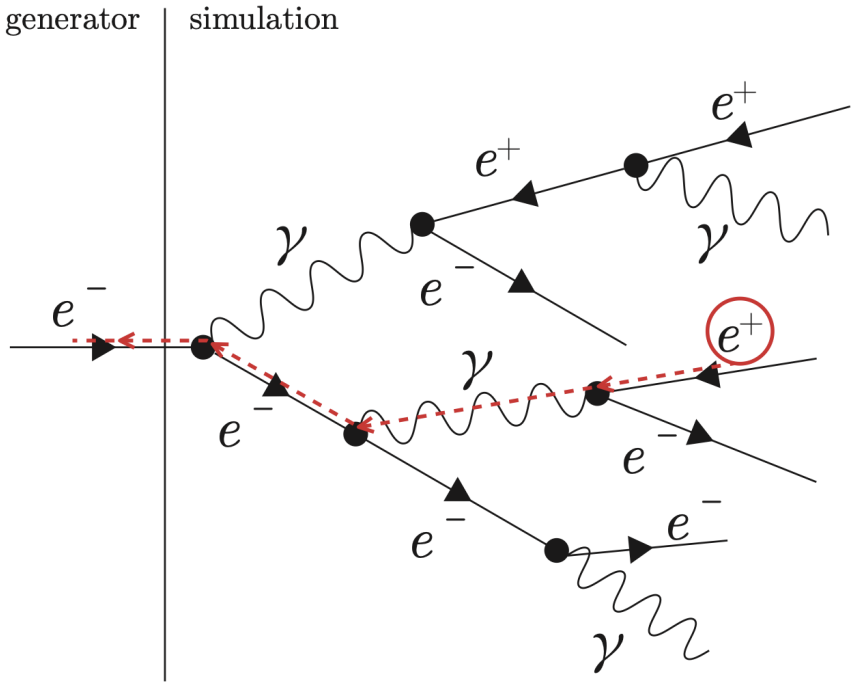

Figure 6.4: Schematic of the electron truth classification. A prompt electron is generated (left side) and undergoes bremsstrahlung as it passes through the detector. One of the resulting photons converts into an e^+e^- pair. A positron from this conversion (circled) is incorrectly matched to the electromagnetic energy deposit, resulting in a misidentified charge. Tracing this positron's ancestry reveals its true origin, the original generated electron, which serves as the `FirstEgMother` and carries the correct charge information. Figure is taken from Ref. [67].

through the full decay chain to its generator-level ancestor. This ancestor, referred to as the `FirstEgMother`, represents the first non-simulation particle (electron or photon) in the chain, and it holds the correct charge information. The `MCTruthClassifier` then assigns properties to this ancestor, such as `FirstEgMotherType` (electron or photon), `FirstEgMotherOrigin` (e.g., Z boson, photon conversion), and `FirstEgMotherPdgID` (which is ± 11 for electrons and positrons). This process is visually represented in Figure 6.4.

Electron type	TruthType	TruthOrigin	FirstEgMotherType	FirstEgMotherOrigin	Charge-flip
Prompt	2	13	2	13	No
Charge-flip type-2	2	13	2	13	Yes
Brem	4	5	2	13	No
Charge-flip type-4	4	5	2	13	Yes
FSR	4	5	15	40	—

Table 6.1: Truth classification for different categories of electrons relevant to charge misidentification studies. The `TruthType` and `TruthOrigin` identify the matched truth electron, while `FirstEgMotherType` and `FirstEgMotherOrigin` trace the electron's ancestry to determine its generator-level origin. The last column indicates whether the reconstructed charge is expected to be incorrect.

To define the set of electrons relevant for charge misidentification studies, the following selection criteria are applied:

$$\texttt{TruthType} == 2 \quad \text{or} \quad (\texttt{TruthOrigin} == 5 \text{ and } |\texttt{FirstEgMotherPdgID}| == 11)$$

`TruthType == 2` identifies prompt electrons from electroweak boson decays (e.g., $Z \to e^+e^-$). `TruthOrigin == 5` and `|FirstEgMotherPdgID| == 11` identifies electrons from photon conversions, where the photon came from bremsstrahlung of a prompt electron. To determine if an electron has a wrongly reconstructed charge, we compare the reconstructed charge to the sign of `FirstEgMotherPdgID`. A mismatch is flagged when:

$$\texttt{recoCharge} \times \texttt{FirstEgMotherPdgID} > 0$$

Here, a positive product indicates that the reconstructed charge does not match the true charge. Using this framework, electrons in MC can be classified into the following categories:

- *Prompt electrons*: from W/Z decays, correctly reconstructed.
- *Brem electrons*: from bremsstrahlung conversions, but still correctly charged.
- *Type-2 charge-flip electrons*: prompt-like truth electrons with wrongly reconstructed charge.
- *Type-4 charge-flip electrons*: from photon conversions, where the selected track is of opposite charge to the originating (`FirstEgMother`) prompt electron.

The corresponding electron truth classification for these categories is summarized in detail in Table 6.1. The composition of same-sign charge events in different type of electrons is shown in Figure 6.5.

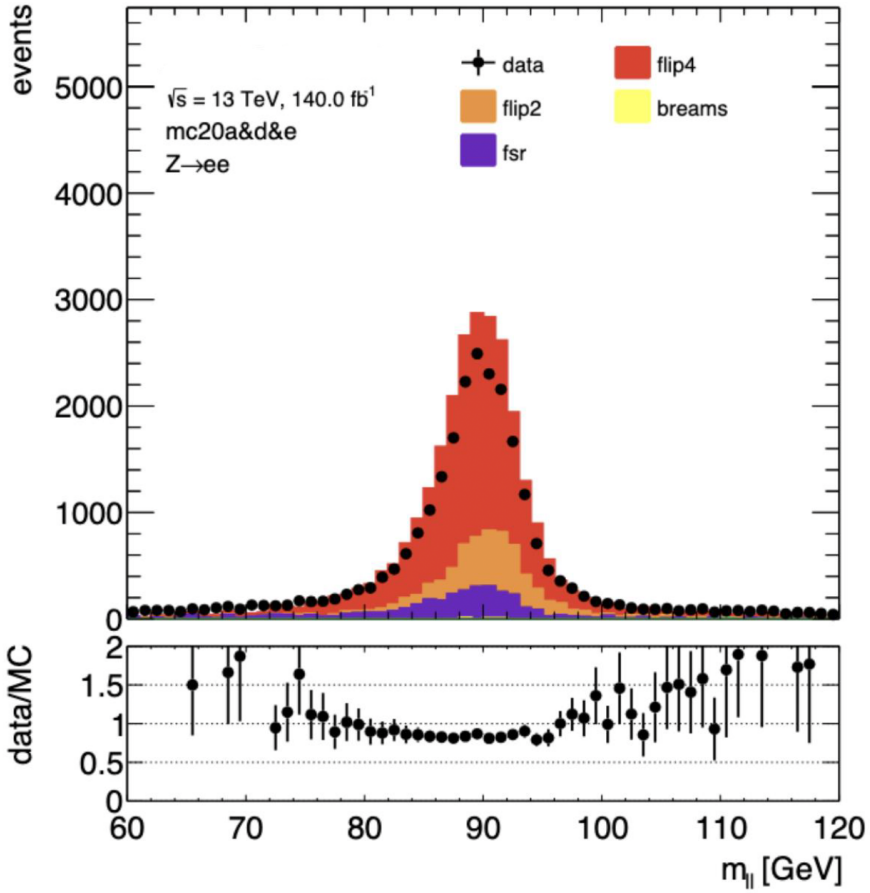

Figure 6.5: Composition of $Z \to e^+e^-$ events selected with electrons with same-sign charge. The events are classified using the truth information.

CHAPTER 7

Measurement of Charge misID Rates and Scale Factors

This chapter outlines the procedures used to measure electron charge misidentification (misID) rates and to derive corresponding scale factors. These scale factors are essential for correcting differences between data and simulation, particularly in physics analyses involving same-sign leptons. The methodology includes the transition to a new analysis framework, event selection, histogramming, and corrections for backgrounds such as sideband contributions and final-state radiation. An approach based on likelihood maximization is then used to extract the misidentification rates and scale factors. The chapter also discuss the different parameterization strategies, including one-dimensional and two-dimensional binning schemes, and their impact on fit stability and performance.

7.1 Methodology

To extract the electron charge misidentification rates, a data-driven approach is employed using a sample enriched in genuine opposite-sign lepton pairs by selecting events in the vicinity of the $Z \to e^+e^-$ mass peak. The total number of events, as well as the number of observed same-sign events, is determined within the main region and two adjacent sideband regions. To isolate the true Z signal, non-Z background is estimated and subtracted from main region using a sideband subtraction technique. Following this, the charge-flip probability for a single electron in a given (η,p_T) bin to have the charge wrongly reconstructed is derived. The extraction of these charge-flip rates is performed using a likelihood minimization procedure and the resulting probabilities are then parametrized using two distinct approaches. These steps are described in detail in the following subsections in the order in which they are performed.

7.1.1 Migration to a New Framework

The first step in the derivation of electron charge misID scale factors involves the production of analysis ntuples from both data and MC simulation samples. These ntuples serve as the foundational input for

all subsequent steps in the charge flip analysis.

In Release 21 with Run 2 data, SUSY analysis group used the *SusySkimAna* framework, which is based on the functionality of *SUSYTools* for object selection, calibration, and systematic handling on the xAOD level. The electron energy calibration used in this framework was `es2018_R21_v0`. However, the ntuple production has since transitioned to a framework based on CPAlgorithms (CPAlgs). This is motivated by several practical considerations:

- Easier configuration: CPAlgs offers easier and more flexible configuration, streamlining the setup and execution of analysis workflows. CPAlgs simplifies the process of updating configurations when switching between Run 2 and Run 3 data taking periods. Moreover, the framework enables the simultaneous processing of multiple electron identification working points (WPs) within a single job.
- CPAlgs is a modern alternative tool. AMG is deprecating old tools and SUSYTools is widely used for Run 1 and Run 2. On the other hand, CPAlgs is a modern tool better aligned with Run 3 analyses.
- CPAlgs is a simpler tool. Unlike SUSYTools, which is designed to support the full complexity of supersymmetry analyses, CPAlgs focuses on the configuration and calibration of physics objects. As a result, it avoids the overhead and dependencies associated with SUSYTools, making it more lightweight and easier to maintain for targeted studies.

For the purpose of validation, the same electron energy calibration model, `es2018_R21_v0`, is used. The derivation of the scale factors uses the most up-to-date electron energy calibration models, namely `es2023_R22_Run2_v1` for Run 2 and `es2024_Run3_v0` for Run 3. To validate[1] the new framework, comparison between the two frameworks is shown in the Figure 7.1. The plots demonstrate excellent agreement between SUSYTools and VBSTTools [2] across all tested kinematic variables. The matching distributions and flat ratio plots confirm that the two frameworks yield consistent physics object definitions and event-level selections even in regions of lower statistics. This validates the transition to CPAlgs for the charge flip analysis and confirms it reproduces nearly the same results as the previously used SUSYTools framework.

7.1.2 Histogramming

The second step in the analysis involves creating input histograms from the ntuples produced by the CPAlgs based framework. For this purpose, the FastFrames package [69] is employed. Comprehensive documentation for the package, including step-by-step instructions for compilation and execution, is available at Ref. [70]. FastFrames is a lightweight and modular histogramming framework designed to process ntuples generated by a CPAlgs based framework. It leverages the ROOT `RDataFrame` interface for efficient event loop processing, allowing for parallelized and memory safe operations on

[1] This validation was performed by another collaborator, John McGowan.
[2] VBSTools is a wrapper around the CPAlgs framework.

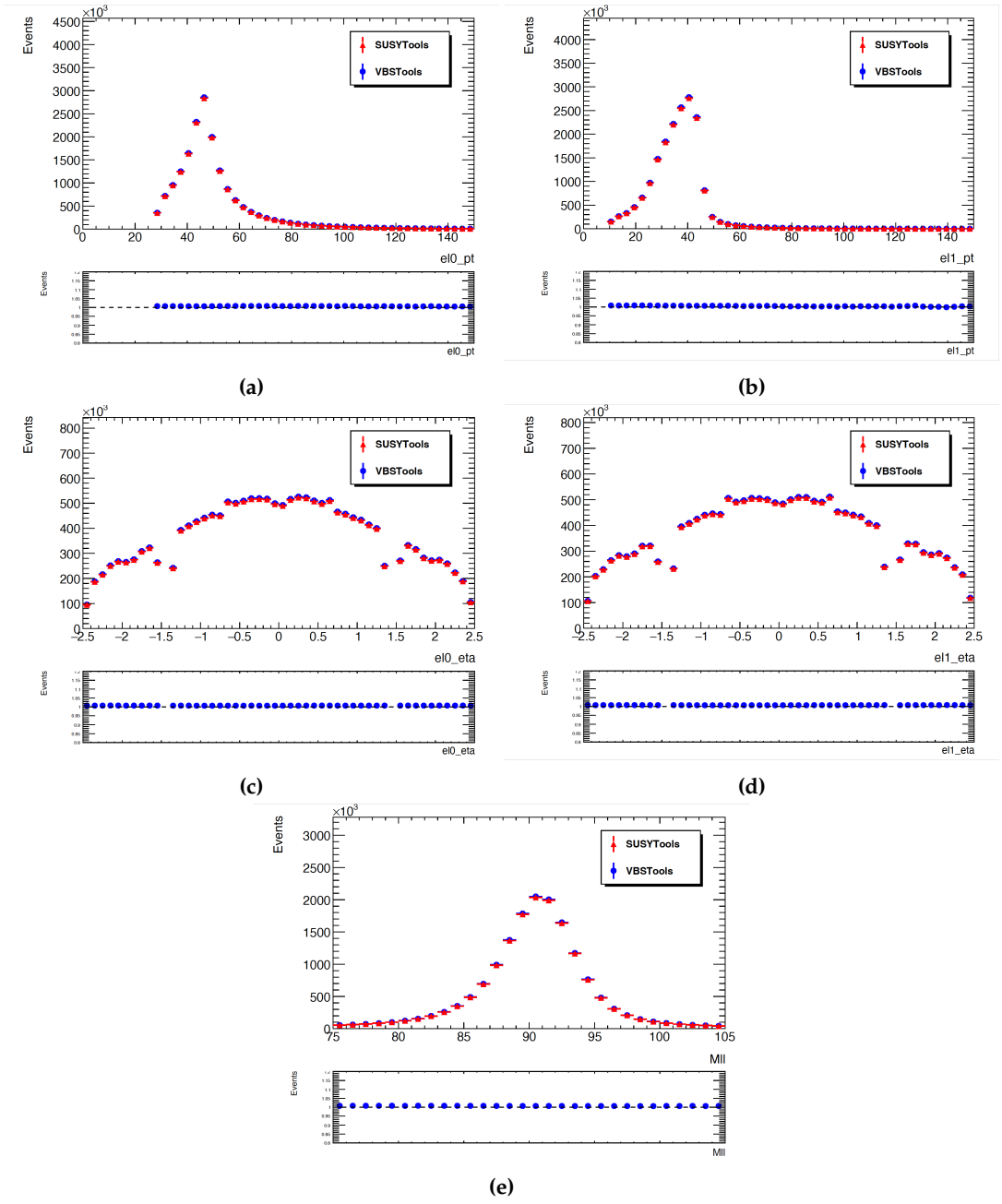

Figure 7.1: Validation plots for the new framework. (a) p_T distribution for leading electron, (b)p_T distribution for subleading electron, (c) η distribution for leading electron, (d) η distribution for subleading electron (e) invariant mass distribution for 2018 data only.

large datasets. FastFrames provide a flexible infrastructure in which users can define custom analysis variables with minimal coding overhead. All the event selections can be made in the configuration file. For the charge-flip analysis, the event selections can be found in the Table 7.1. The single-electron triggers used for each data-taking year are listed in Table 5.2 of Chapter 5, and a logical OR is applied to ensure that an event passing any of these triggers is accepted. Single electron trigger matching ensures that the online trigger objects are geometrically matched to their corresponding offline reconstructed objects. The $m_{ll} \in [60, 120]$ GeV window isolates lepton pairs consistent with a real Z-boson decay, maximizing signal purity while excluding lower and higher mass backgrounds.

Table 7.1: Event-Selection Criteria.

Selection
Two signal electrons
No additional baseline lepton
Single electron trigger Single electron trigger matching
Leading electron $p_T > 28$ *GeV*
Sub-leading electron $p_T > 10$ *GeV*
Invariant mass m_{ll} window $[60, 120]$
Signal electrons: Id: `TightLH` and Iso: `Tight_VarRad`
Baseline electrons: Id: `TightLH`
$\lvert\eta\rvert < 2.47$ && $!(1.37 < \lvert\eta\rvert < 1.52)$

To accurately capture the dependence of the electron charge misID rates on kinematic variables, the analysis employs both fine and coarse binning schemes in p_T and $|\eta|$ of electrons.

Coarse binning : $p_T = [20.0, 60.0, 95.0, 145.0, 7000.0]$ and $|\eta| = [0.00, 0.60, 1.15, 1.37, 1.52, 1.81, 2.37, 2.47]$. The corresponding bin number is computed using: $P_T\_bin + 4 * \eta\_bin$.

Fine binning : $p_T = [20.0, 30.0, 35.0, 40.0, 45.0, 60.0, 95.0, 115, 145, 185, 240, 7000.0]$ and $|\eta| = [0.00, 0.10, 0.60, 0.80, 1.15, 1.37, 1.52, 1.81, 2.01, 2.37, 2.47]$. The corresponding bin number is computed using: $P_T\_bin + 11 * \eta\_bin$.

Two-dimensional histograms are constructed where x-axis represents the bin number for leading electron and y-axis represents the bin number for sub-leading electron. Events are further classified into four distinct invariant-mass m_{ll} regions: *Main Window* ($80\ GeV < m_{ll} < 100\ GeV$), *Main Window same-sign* ($80\ GeV < m_{ll} < 100\ GeV$) with same-sign electrons, *Sideband* ($60\ GeV < m_{ll} < 80\ GeV$ or $100\ GeV < m_{ll} < 120\ GeV$), and *Sideband same-sign* ($60\ GeV < m_{ll} < 80\ GeV$ or $100\ GeV < m_{ll} < 120\ GeV$) with same-sign electrons. Four histograms will be produced based on these regions each for data and MC (charge-flip and FSR electrons) samples and are shown in Figure 7.2 These histograms will be further used as input histograms for the sideband and FSR subtraction to calculate the charge misID rates.

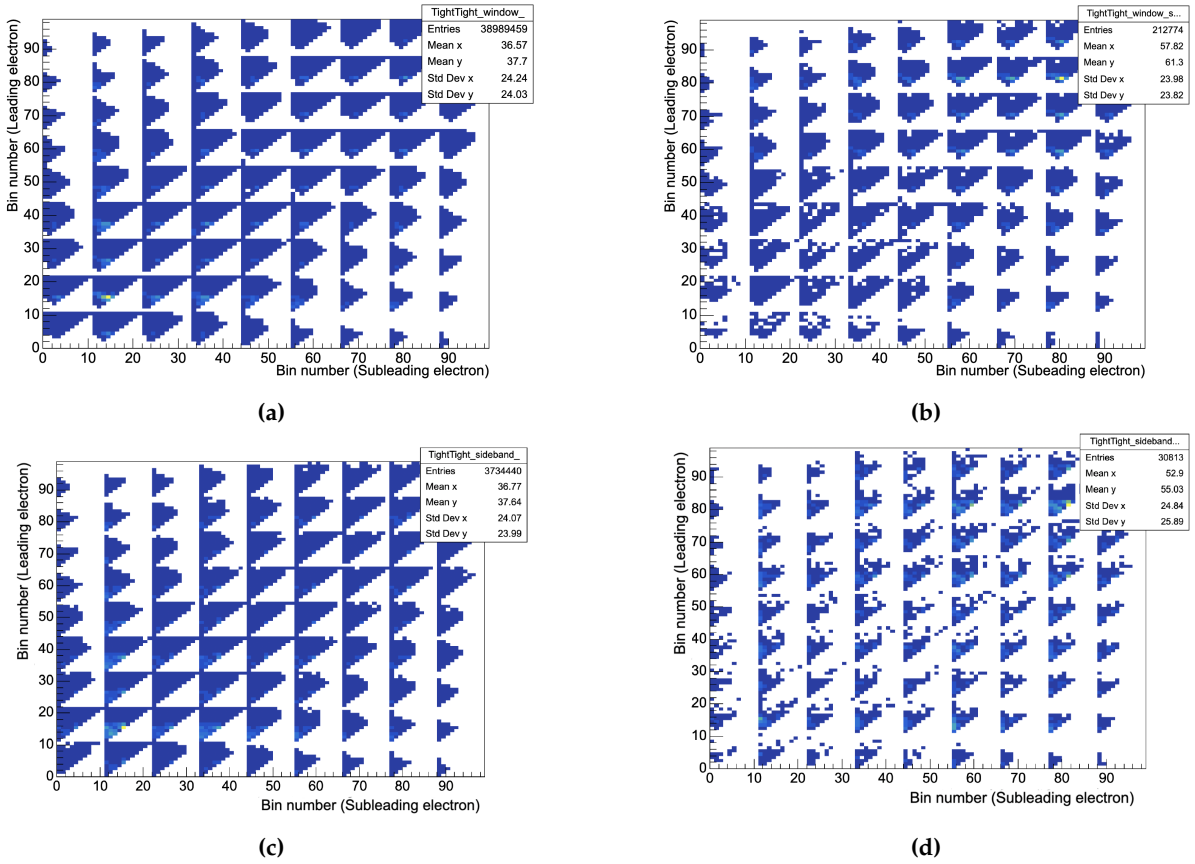

Figure 7.2: Input histograms for the likelihood fitting. (a) shows the total number of events which includes same-sign and opposite-sign electron pairs and (b) is the subset of (a) and only contain same-sign electron pairs in the main region. (c) and (d) corresponds to the sideband region. These histograms are made using full Run 2 data and in fine binning scheme.

7.1.3 Sideband Subtraction

The sideband subtraction method is a data-driven technique used to estimate and remove background contamination from signal regions. The method relies on dividing the invariant mass distribution of electron pairs in $Z \to e^+e^-$ into three regions: a main region and two adjacent sideband regions. Main region is the central region around the Z boson mass peak (typically 80–100 GeV), where genuine $Z \to e^+e^-$ events dominate. Sideband regions with the size of 20 GeV lies on the high mass (100-120 GeV) and low mass (60-80 GeV) side of the main region summarized in Table 7.2.

Table 7.2: Definitions of main regions and sideband regions.

Event type	Invariant mass region	Event weight
Main region	$\lvert m_{ee} - m_Z \rvert < 10\ GeV$	1.0
Sideband region	$10\ GeV < \lvert m_{ee} - m_Z \rvert < 30\ GeV$	0.5

These regions are enriched in non-Z background such as ,di-boson events, and fake electrons from W+jets events. This method estimates the background in the main region by assuming a relatively flat distribution of non-Z background events across the invariant mass spectrum as seen in Figure 6.5. This flatness means that the non-Z background contribution is roughly constant in the regions around the Z mass peak. This non-Z background yield in the central signal region can be approximated by averaging the yields from the high and low mass sidebands and then subtracted from the total number of same-sign events in the signal region as explained in Figure 7.3 [3] This method is only used in data, because MC has truth information to directly isolate prompt $Z \to e^+e^-$ electrons. Because this sideband subtraction carries uncertainties (e.g., from the assumption of flatness and potential signal contamination in sidebands), the entire subtracted yield is treated with a 100% systematic uncertainty.

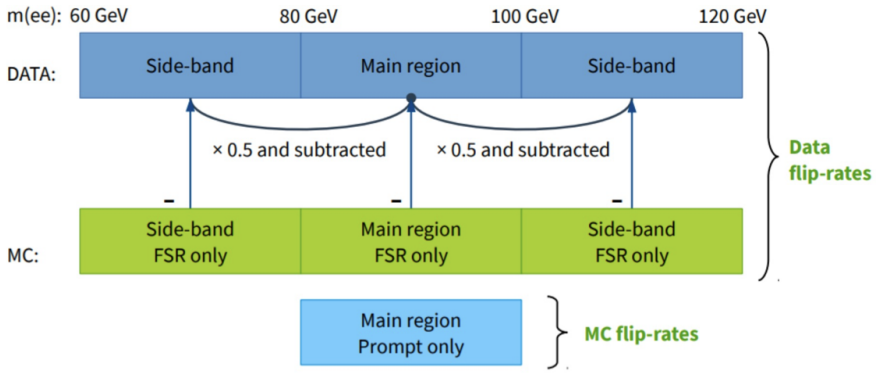

Figure 7.3: Sideband/FSR subtraction. The non-Z background yield in the main window is estimated by averaging the event counts in the two sidebands.

7.1.4 Final State Radiation Subtraction

When measuring the charge misID rates, it is crucial to isolate prompt electrons from those arising due to FSR. FSR electrons are prompt in nature, but their charge is ambiguous because the photon that converts into an electron–positron pair originates from a prompt lepton and upon conversion, it is not always clear which of the resulting electrons should inherit the original charge. Due to this ambiguity, the charge flip scale factors derived from regular prompt electrons are not valid for FSR electrons.

In MC FSR electrons are identified using truth information. Only non-FSR prompt electrons are used for measuring charge misID probabilities in MC. Since truth classification is not available in data, events containing potential FSR electrons must be excluded. This is done by subtracting the FSR contribution estimated from MC from both the main $Z \to e^+e^-$ region and the sideband regions. Since the charge misID measurement requires two electrons per event, an event is labeled as containing FSR if at least one electron is identified as originating from FSR. The classification and truth matching criteria used for this selection are summarized in Table 7.3.

[3] This figure is taken from a presentation presented in eGamma Combined Performance (CP) group meeting, June 2024.

Table 7.3: Truth matching used in MC to determine signal and FSR electrons.

Event type	`firstEgMotherType/firstEgMotherOrigin` **Leading electron**	`firstEgMotherType/firstEgMotherOrigin` **Sub-leading electron**
Signal	2/13	2/13
FSR	15/40	2/13
	2/13	15/40
	15/40	15/40

7.1.5 The Likelihood Function

The measurement of electron charge misID rates is carried out as a double-differential analysis in bins of p_T and η, as these variables have a significant influence on the charge reconstruction performance. Due to incorrect charge assignment during the reconstruction process, a small fraction of $Z \to e^+e^-$ events appears with same-sign electron pairs. The objective of the measurement is to determine the probability that a single electron, falling within a specific (p_T, η) bin, is reconstructed with the wrong electric charge after the background subtraction. These probabilities can be measured using the method of likelihood maximization. To build the likelihood function, the electrons are grouped into 2-dimensional (2D) bins based on the two variables (p_T, η). The expected number of same-sign (SS) pairs in a given bin (i,j), denoted λ', can be modeled as a function of the single-electron charge-flip probabilities where i and j represents the bin index for the leading and sub-leading electron respectively. Let ϵ_i is the charge-flip probability for the leading electron in bin i, ϵ_j is the charge-flip probability for the sub-leading electron in bin j and N^{ij} is the total number of observed electron pairs in bin (i,j) which includes opposite sign (OS) pairs N^{ij}_{OS} as expected from the true $Z \to e^+e^-$ events and same-sign (SS) pairs N^{ij}_{SS} which arise when one of the electrons is misidentified.

With the assumption that only one electron flips charge at a time, the expected number of same-sign events is given by:

$$\lambda' \to \lambda^{ij} = N^{ij}[\epsilon_i(1-\epsilon_j) + \epsilon_j(1-\epsilon_i)] + BKG^{ij}_{SS} + FSR^{ij}_{SS}, \tag{7.1}$$

where the term $\epsilon_i(1-\epsilon_j)$ depicts the scenario when leading electron flips the electron and the sub-leading electron does not. On the other hand, $\epsilon_j(1-\epsilon_i)$ depicts the scenario when sub-leading electron flips the electron and the leading electron does not. However, in data, this expected number must be corrected to account for backgrounds, such as same-sign background estimated from the sideband subtraction BKG^{ij}_{SS} and contribution from FSR electrons FSR^{ij}_{SS}. To extract the best-fit charge-flip probabilities ϵ_i and ϵ_j, a likelihood function is constructed with a Poisson probability for observing the measured number of same-sign events N^{ij}_{SS} as:

$$f(N^{ij}_{SS};\, \lambda') = \frac{{\lambda'}^{N^{ij}_{SS}} e^{-\lambda'}}{N^{ij}_{SS}!}. \tag{7.2}$$

The charge-flip rates are extracted with a likelihood fit by summing all of the Poissonian probabilities in Equation 7.2 and maximizing the likelihood by varying the charge-flip probabilities. Since likelihood maximization is numerically more stable when turned into a minimization problem, a negative log-likelihood is used instead. The factorial term from the Equation 7.2 is ignored (because it is constant and does not affect the minimization) while constructing the negative log-likelihood:

$$-\log L\left(\vec{\varepsilon}\,|\,\vec{N}_{\mathrm{SS}},\vec{N}\right) \approx -\sum_{i,j}\left[N_{\mathrm{SS}}^{ij}\log\left(\lambda^{ij}\right)-\lambda^{ij}\right]. \tag{7.3}$$

The minimization of the negative log-likelihood is performed using the `Minuit2` [71] minimization package with the different algorithms such as `MIGRAD, MINIMIZE, SIMPLEX, SCAN` and `SEEK`, as implemented in the ROOT framework.

7.2 Parameterization of Charge Misidentification Probability

Once the charge misidentification probabilities are extracted from the likelihood fucntion, they must be expressed in a form that can be used in physics analyses. This is achieved through a parameterization of the charge flip probability as a function of p_T and η. Two different parameterizations 1D×1D and 2D are discussed here.

7.2.1 1DX1D vs 2D Parameterization

The standard approach to measuring charge-flip probabilities is through a double-differential 2D binning in p_T and η. If we use fine binning scheme explained in Section 7.1.2, there will be 11 bins of p_T and 9 bins of η results in total of $N_{p_T} \times N_\eta = 99$ free parameters, one for each bin in the 2D map. The measurement is performed at $Z \to e^+e^-$ peak, which limits the statistics at high p_T. Beyond $p_T = 45$ GeV, and especially above $p_T = 95$ GeV, the number of events drops significantly, leading to very large statistical uncertainties. This makes the 2D measurements statistically unstable.

To mitigate the problem of limited statistics at high p_T, a 1D×1D factorized model is introduced. The idea here is to approximate the 2D charge flip probability $\epsilon(p_T, |\eta|)$ as the product of two independent 1D functions:

$$\epsilon(p_T, |\eta|) = \sigma(p_T) \times f(|\eta|) \tag{7.4}$$

The assumption is that the shape of the $|\eta|$-dependence is approximately the same across all p_T bins, allowing this factorization. So, instead of estimating a separate rate for each (p_T, η) bin, it can be factor into two 1D components, reducing the total number of free parameters, which helps in stability even at high p_T. To ensure a non-trivial solution and reduce redundancy, one of the functions $f(|\eta|)$ is normalized to unit area:

$$\int f(|\eta|)\, d\eta = 1 \tag{7.5}$$

With this normalization constraint, the number of free parameters in the likelihood is reduced to $N_{p_T} + N_\eta - 1 = 19$, enabling improved granularity in η without inflating the statistical uncertainties.

7.3 Charge misID Rates

This section presents the extracted electron charge misID rates obtained using the methodology described in the Section 7.1. The charge misID probability is computed for single electrons as a function of their transverse momentum p_T and pseudorapidity $|\eta|$, through 1D×1D parameterization. These rates quantify the probability that the charge of an electron is incorrectly reconstructed, and are crucial for estimating backgrounds in analyses involving final state same-sign leptons.

The results are shown in Figure 7.4 for `TightLH` identification and `Tight_VarRad` isolation working point and are based on data collected in year 2015-2018 at $\sqrt{s} = 13\,\text{TeV}$, 140 fb^{-1} using $Z \to e^+e^-$ events after applying corrections for non-Z backgrounds and FSR using 1D×1D parameterization in fine binning. As expected, the charge flip rate increases with increasing $|\eta|$, particularly in the forward region of the detector where bremsstrahlung and material interactions are more significant and the track curvature measurement is less precise. Additionally, a mild rise in the misID rate is observed at higher p_T, especially beyond 60 GeV, which is consistent with increased curvature misreconstruction at high energies. The impact of FSR subtraction and sideband background modeling is quantified via variations shown in blue and green respectively. The charge flip rates for other working points are shown in Appendix A.

7.4 Charge misID Scale Factors

The charge misID Scale Factors (SFs) are introduced to correct for differences in the probability of electron charge misidentification between data and MC simulation. These scale factors ensure that the modeling of charge flip rates in MC reflects the behavior observed in real data. Scale factors are computed from data and MC rates for right and wrong charge electrons. The SFs for wrong-charge and right-charge electrons are given by:

$$\text{SF}_{\text{wrong}} = \frac{\varepsilon_{\text{data}}}{\varepsilon_{\text{MC}}} \qquad \text{SF}_{\text{right}} = \frac{1-\varepsilon_{\text{data}}}{1-\varepsilon_{\text{MC}}} \tag{7.6}$$

$\varepsilon_{\text{data}}$ and ε_{MC} are charge misidentification probabilities in data and MC, respectively. The scale factors for electrons selected with different identification and isolation working points, together with the respective relative statistical uncertainties are shown in the Chapter 8.

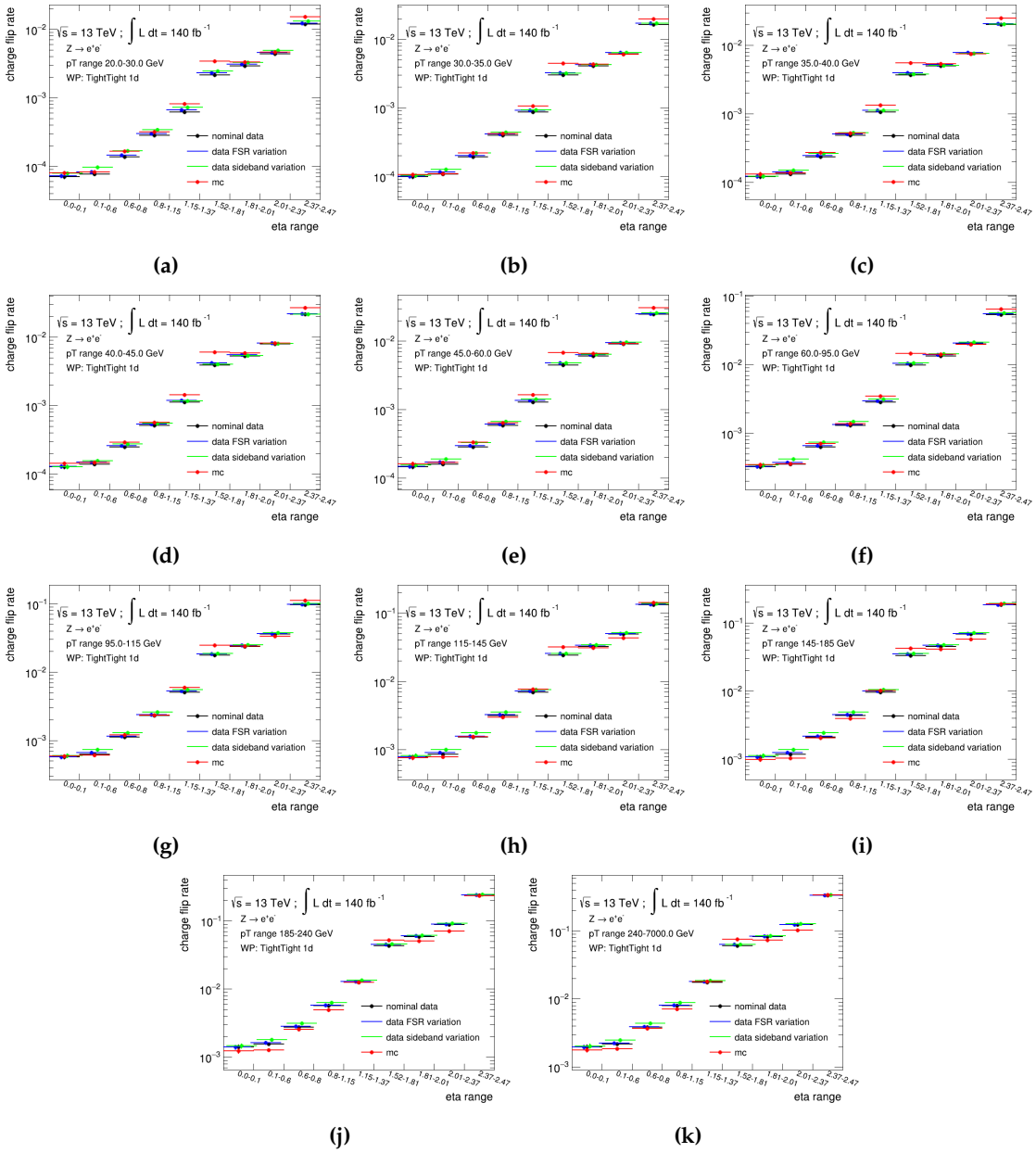

Figure 7.4: Charge misID rates passing the `TightLH` identification and `Tight_VarRad` isolation working point. These rates are derived using 1D × 1D parameterization in full Run 2 data (2015-2018) and MC campaigns mc20a, mc20d and mc20e. Each sub-figure corresponds to a different bin in electron p_T, with the charge flip rate plotted as a function of $|\eta|$. (a–c): Low p_T region (20–45 GeV) showing lower flip rates, but still showing η dependence. (d–h): Intermediate p_T (45–145 GeV) showing moderate flip rates with clear forward-region rise, (i–k): High p_T(>145 GeV) showing low statistics, but flip rates remain high at large η.

CHAPTER 8

Results

8.1 Non-convergence in 2D parameterized Scale Factors

As discussed in Section 7.2.1, the charge misidentification probabilities are parameterized either using a 2D binning in p_T and η, or via a factorized 1D×1D approach. While the 2D parameterization allows fine-grained modeling, it is particularly susceptible to statistical fluctuations in high-p_T and forward η bins where data statistics are relatively low. During the scale factor extraction process using the 2D parameterization with fine binning, we observe non-convergence of the likelihood minimization. In this context, non-convergence refers to the failure of the minimizer (`MIGRAD` algorithm from `Minuit2` package) to find a stable set of charge misID rates across all bins. This is likely due to limited statistics in certain regions of the fine-binned histogram, leading to flat or poorly constrained likelihood profiles. This issue is illustrated in Figure 8.1, where the extracted values for multiple bins are either undefined or poorly constrained. Alternatively, the 1D×1D parameterization consistently shows successful convergence even in fine binning (see Figure 8.2). This approach benefits from a reduced number of fit parameters and introduces a normalization constraint that stabilizes the likelihood function.

To mitigate this issue, a coarser binning scheme is tested in 2D parameterization, wherein the number of and p_T and η bins are reduced. Under this configuration, the likelihood minimization successfully converges, indicating that the bin merging restores statistical robustness in Figure 8.3. The scale factors show broad compatibility with those from the 1D×1D parameterization under coarse binning (Figure 8.4), though some level of discrepancy persists.

In 2D parametrization, the charge-flip probability $\epsilon(p_T, \eta)$ is extracted in bins of both p_T and η, which means each bin has its own independent estimate. Sideband and FSR subtraction is performed individually in each bin and treated as 100 % systematics. So, any statistical fluctuation in a single bin can significantly bias the estimate in that bin. These fluctuations are localized, i.e. they effect only that bin and not regularized because each 2D bin is treated independently. Thus, in 2D parameterization the systematic error per bin due to sideband/FSR subtraction becomes amplified, especially in low statistic bins. On the other hand, in 1D×1D approach, the probability is factorized as $\epsilon(p_T, |\eta|) = \sigma(p_T) \times f(|\eta|)$. The histograms for $\sigma(p_T)$ and $f(|\eta|)$ are projected along one axis and therefore involve more statistics per bin. The sideband/FSR subtraction is still done per bin, but now each 1D bin

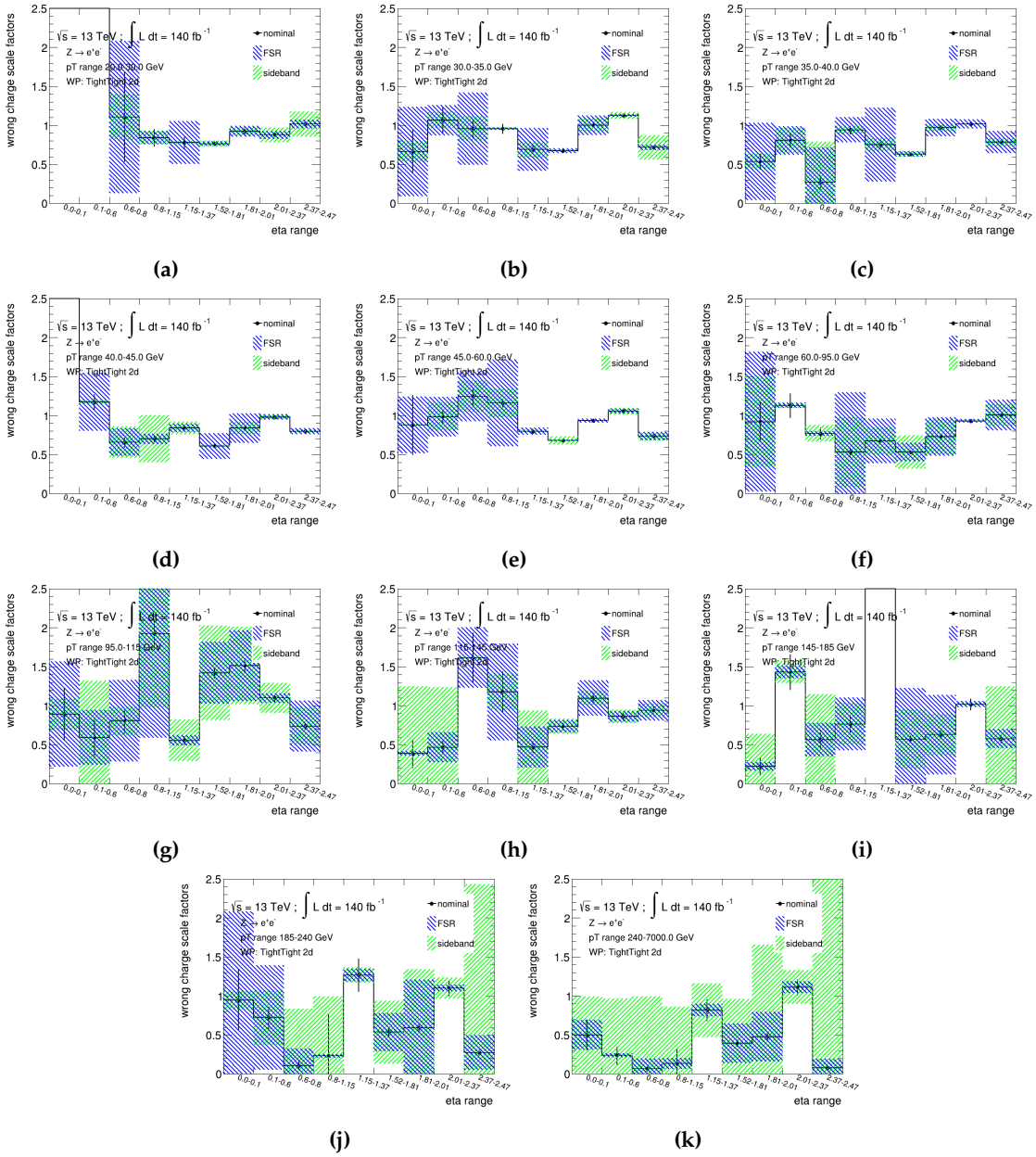

Figure 8.1: Charge misID scale factors for electrons passing `TightLH` identification and `Tight_VarRad` isolation working point using 2D parameterization in fine binning. The scale factors are presented for wrongly reconstructed electron charges along with corresponding systematic uncertainties from FSR and sideband subtraction in various p_T slices. Fine binning is used in deriving these scale factors using 2D parameterization which shows the non convergence in low statistics region.

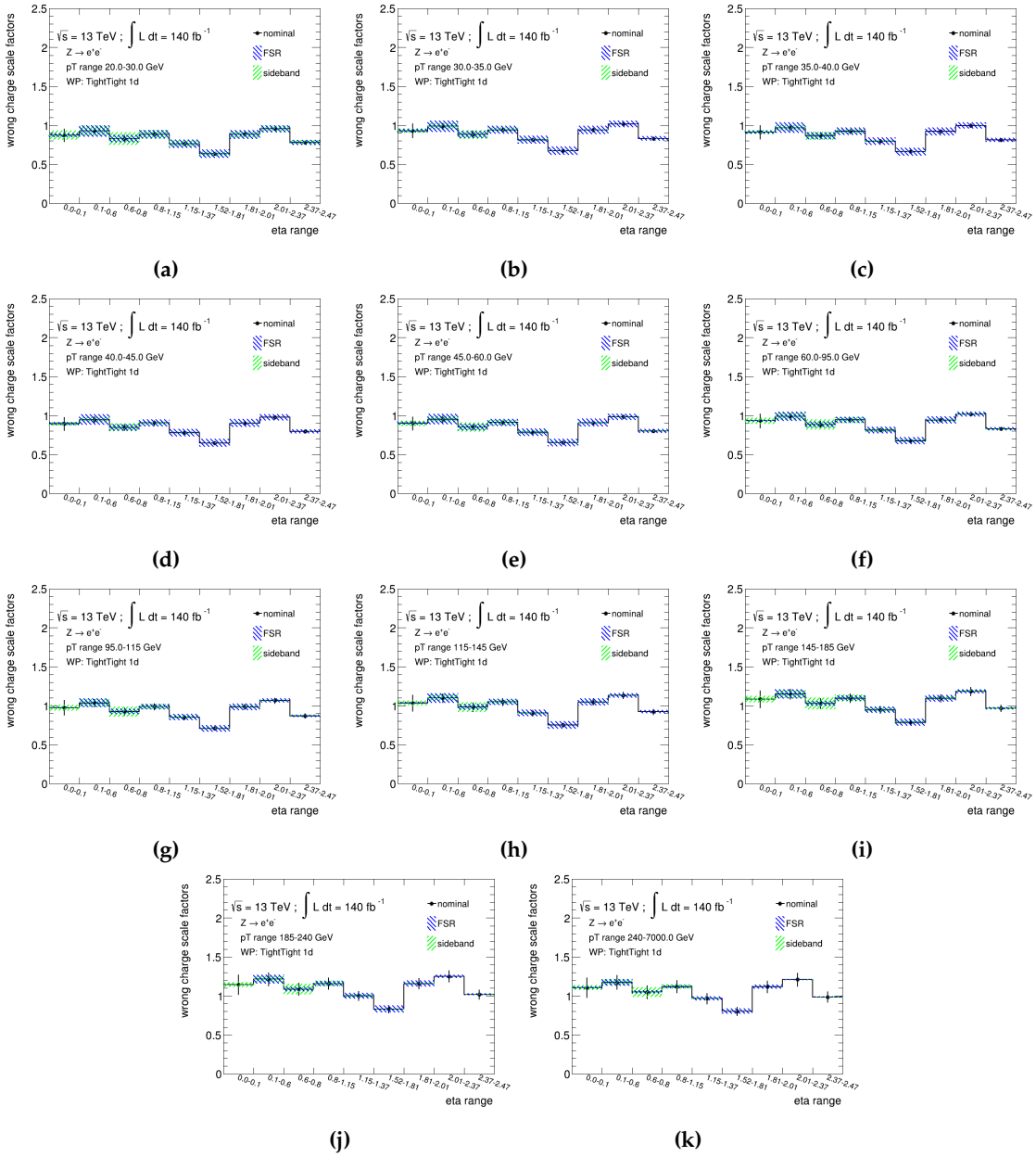

Figure 8.2: Charge misID scale factors for electrons passing `TightLH` identification and `Tight_VarRad` isolation working point using 1D×1D parameterization in fine binning. The scale factors are presented for wrongly reconstructed electron charges along with corresponding systematic uncertainties from FSR and sideband subtraction in various p_T slices. Fine binning is used in deriving these scale factors using 1D×1D parameterization which shows a good convergence even in low statistics region.

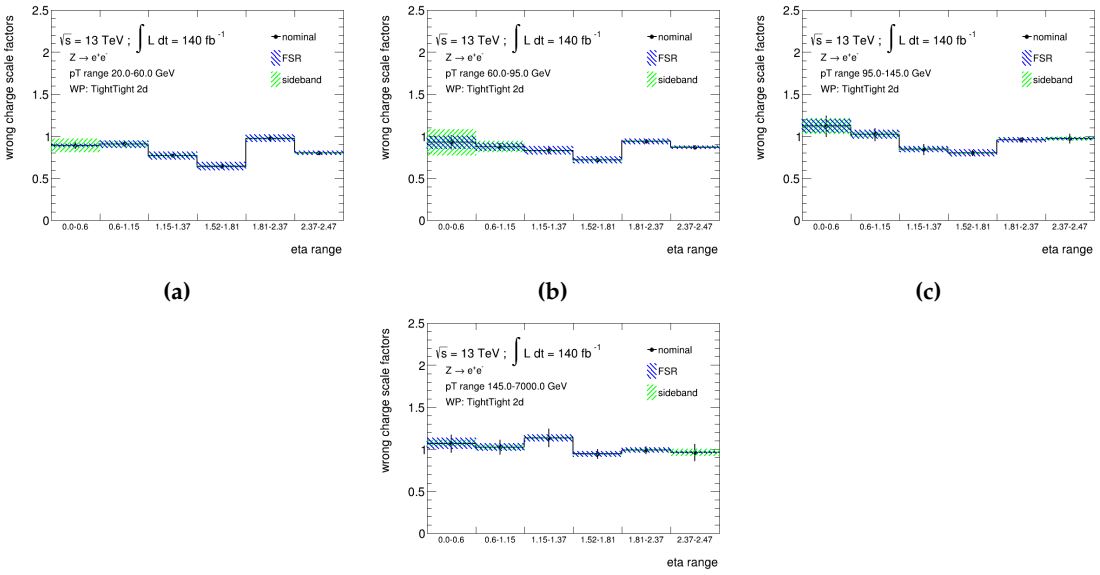

Figure 8.3: Charge misID scale factors for electrons passing `TightLH` identification and `Tight_VarRad` isolation working point using 2D parameterization in coarse binning. The scale factors are presented for wrongly reconstructed electron charges in various p_T slices. Coarse binning is used in deriving these scale factors using 2D parameterization which shows a better convergence in low statistics region.

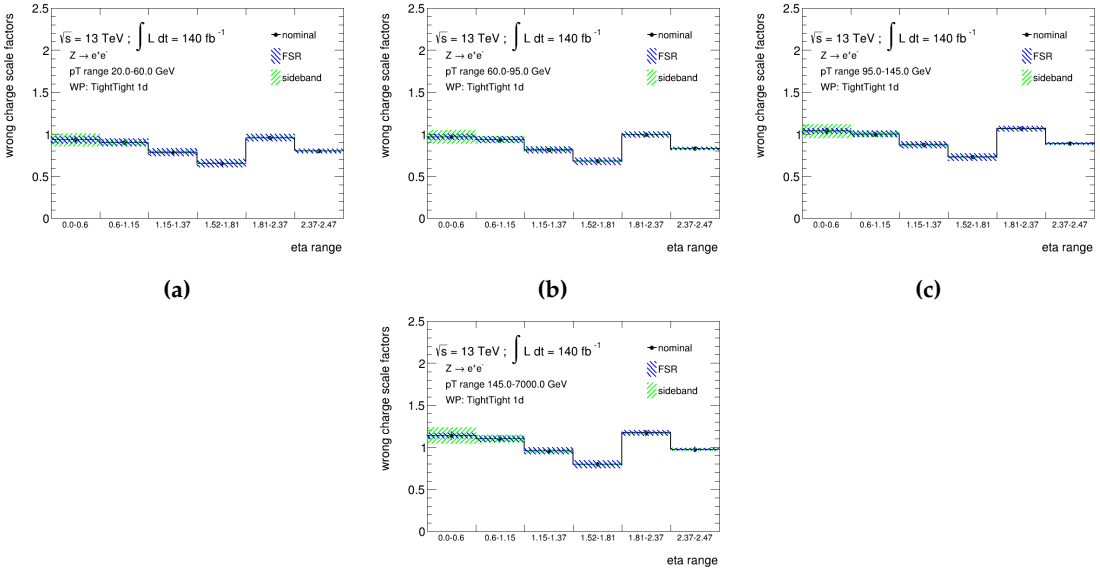

Figure 8.4: Charge misID scale factors for electrons passing `TightLH` identification and `Tight_VarRad` isolation working point using 1D×1D parameterization in coarse binning. The scale factors are presented for wrongly reconstructed electron charges in various p_T slices. Coarse binning is used in deriving these scale factors using 1D×1D parameterization which shows almost same convergence as in case of 2D parameterization.

accumulates more events, reducing the relative fluctuation from any given subtraction. Additionally, the normalization constraint in 1D×1D fits helps absorb some of the bin-by-bin fluctuations. Thus, in 1D parameterization, the impact of local fluctuations is averaged out over broader bins. Systematic uncertainties from sideband and FSR subtraction propagate less sharply into individual scale factor values.

Nonetheless, in order to evaluate the impact of the choice of parameterization, a closure test is performed. The charge-flip probabilities obtained using both the 2D and 1D×1D methods are compared to truth-level flip rates in MC simulation. The results are presented in Figure 8.5, where 8.5(a) corresponds to the fine binning scheme and 8.5(b) to the coarse binning scheme. In both cases, the extracted rates follow the general trend of the truth-level values. However, for both binning schemes, flip rates using 2D parameterization shows better closure with truth-level flip rates because this method uses non-factorizable structure, i.e. the dependence on p_T and η is not separable. Due to the correlations between p_T and η, 2D parameterization more accurately reflects the true detector and physics behavior. Therefore, closure tests with 2D are better. Most of the analyses prioritize robustness and stability, especially when applying scale factors to data-driven background estimation and when the main concern is systematic uncertainty propagation, not ultra-fine modeling. So, even though 2D gives better closure, 1D×1D is often preferred for its stability, especially in fine-binned fits with limited statistics. Nonetheless, neither parameterization achieves perfect closure across all bins. To account for this, the level of non-closure observed in the closure test is conservatively assigned as a systematic uncertainty, which is evaluated by comparing 1D×1D and 2D parametrization scale factors in coarse binning, on the final scale factors shown in Figure 8.8.

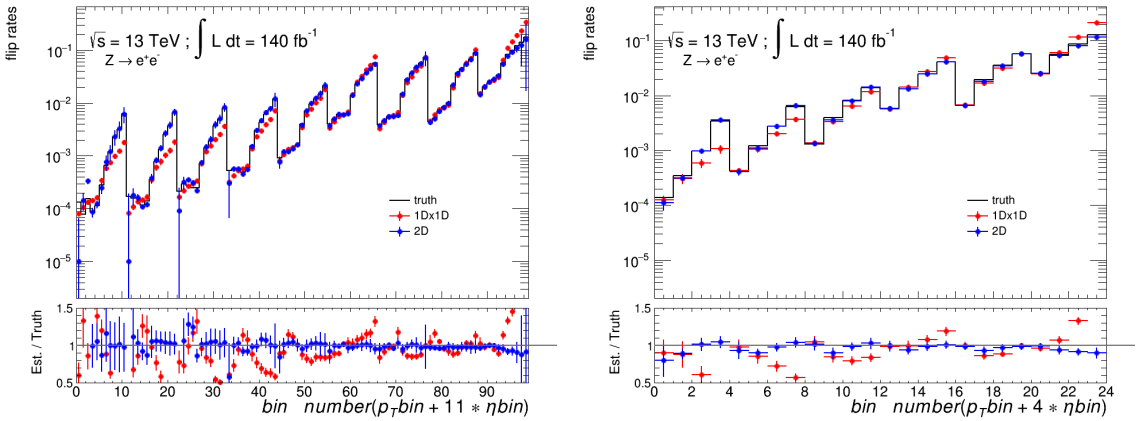

(a) **(b)**

Figure 8.5: Closure test for 2D and 1D×1D parameterized flip-rates with truth-level charge-flip rates from MC simulation. (a) Using fine binning (b) Using coarse binning. Although better truth closure is achieved with the 2D parameterization, residual differences compared to the 1D×1D method lead to an additional systematic uncertainty to account for non-closure effects.

8.2 Scale Factors using Likelihood only

In this section scale factors derived with the `TightLH` identification and `Tight_VarRad` isolation working point are presented. Scale factors for other working points are shown in Appendix B.

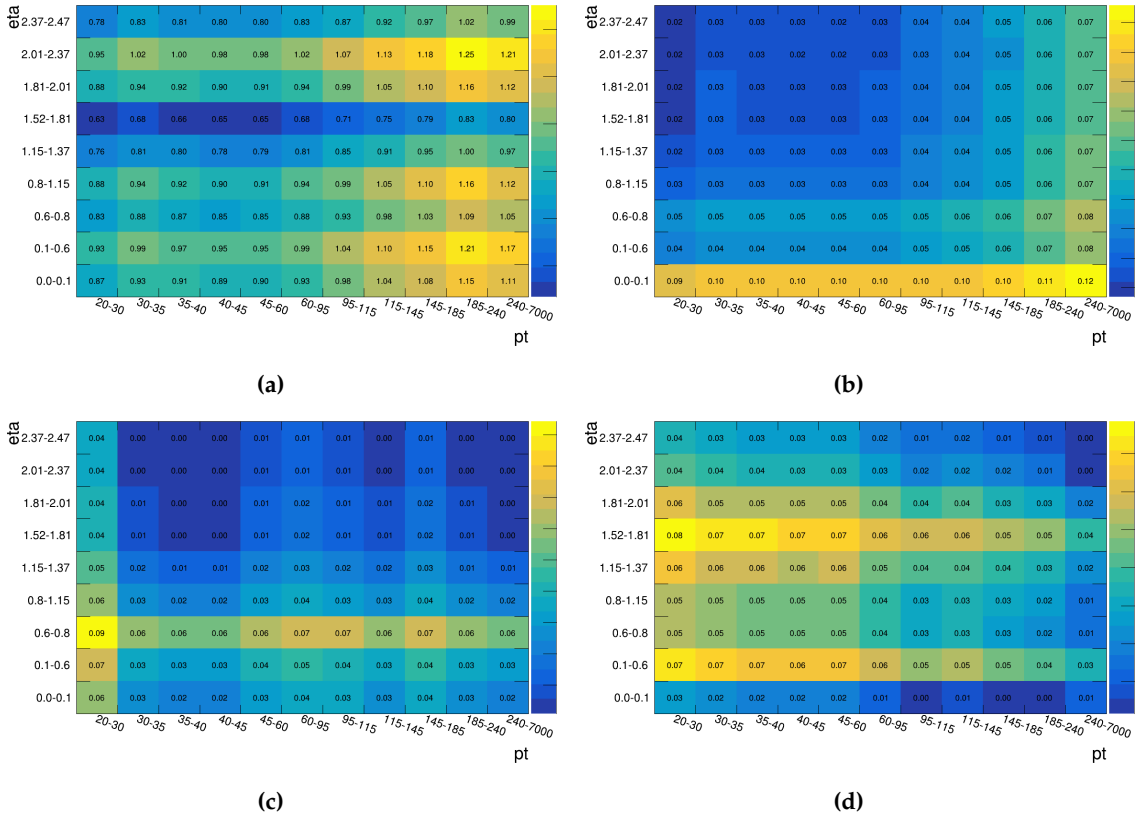

Figure 8.6: Scale factor maps derived with data 2015-2018 and MC campaigns mc20a, mc20d and mc20e for electrons passing `TightLH` identification and `Tight_VarRad` isolation working point. Fine binning with 1D×1D parameterization is used to derive these (a) scale factors for Data/MC (b) statistical uncertainties (c) systematic uncertainties from sideband subtraction (d) systematic uncertainties from FSR subtraction.

Scale factors below the value of 1.0 indicate that MC overestimates the charge misID rate relative to data, scale factors equal to 1 suggests good agreement between data and MC, and scale factors above 1.0 imply that the MC underestimates the charge misID rates compared to what is observed in data. From Figure 8.6 it can be observed that the largest deviations from unity occur in the forward regions, which is expected due to increased bremsstrahlung and tracker inefficiencies in the detector. The maximum scale factor is around 25% for the wrongly reconstructed electrons and never exceed 0.5% for correctly reconstructed electrons. The wrongly and correctly charge scale factors with systematics added due to the 1D×1D and 2D parameterization non-closure are shown in Figure 8.8 and 8.9, respectively. The scale factors with data 2022-2023 are also presented in Figure 8.7.

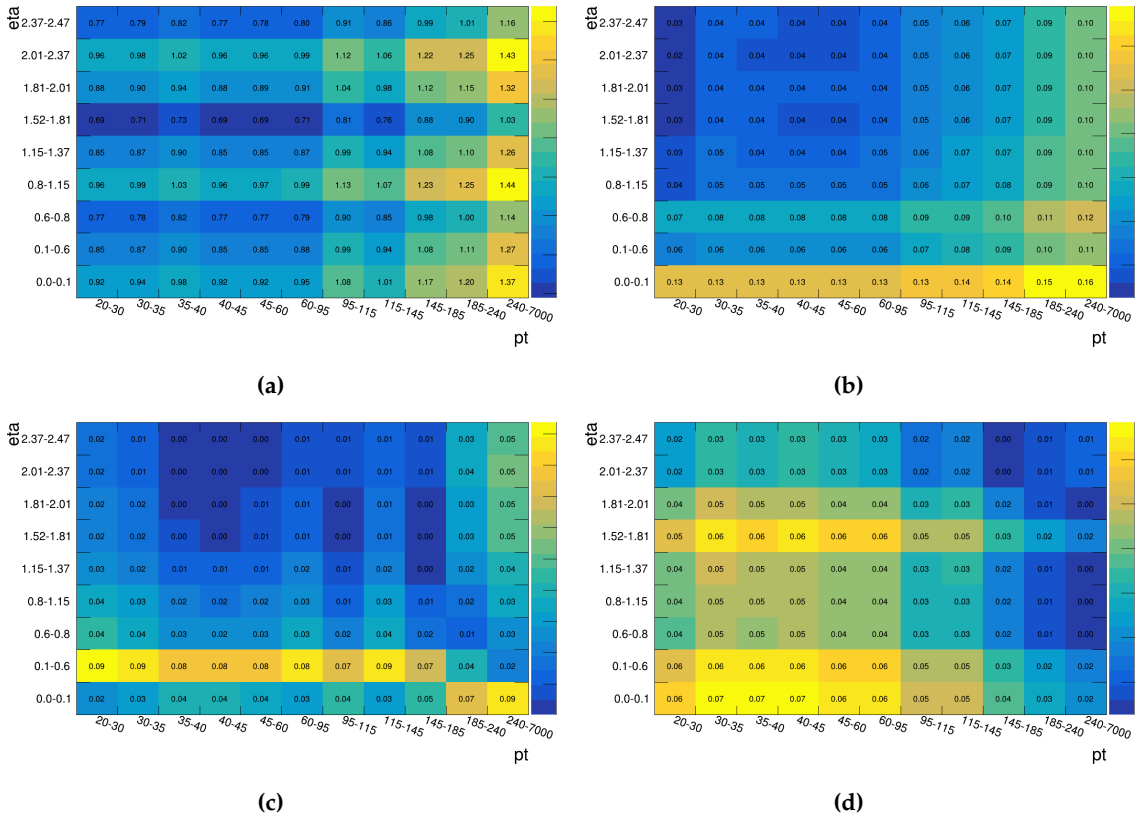

Figure 8.7: Scale factor maps derived with data 2022-2023 and MC campaigns mc23a and mc23d for electrons passing `TightLH` identification and `Tight_VarRad` isolation working point. Fine binning with 1D×1D parameterization is used to derive these (a) scale factors for Data/MC (b) statistical uncertainties (c) systematic uncertainties from sideband subtraction (d) systematic uncertainties from FSR subtraction.

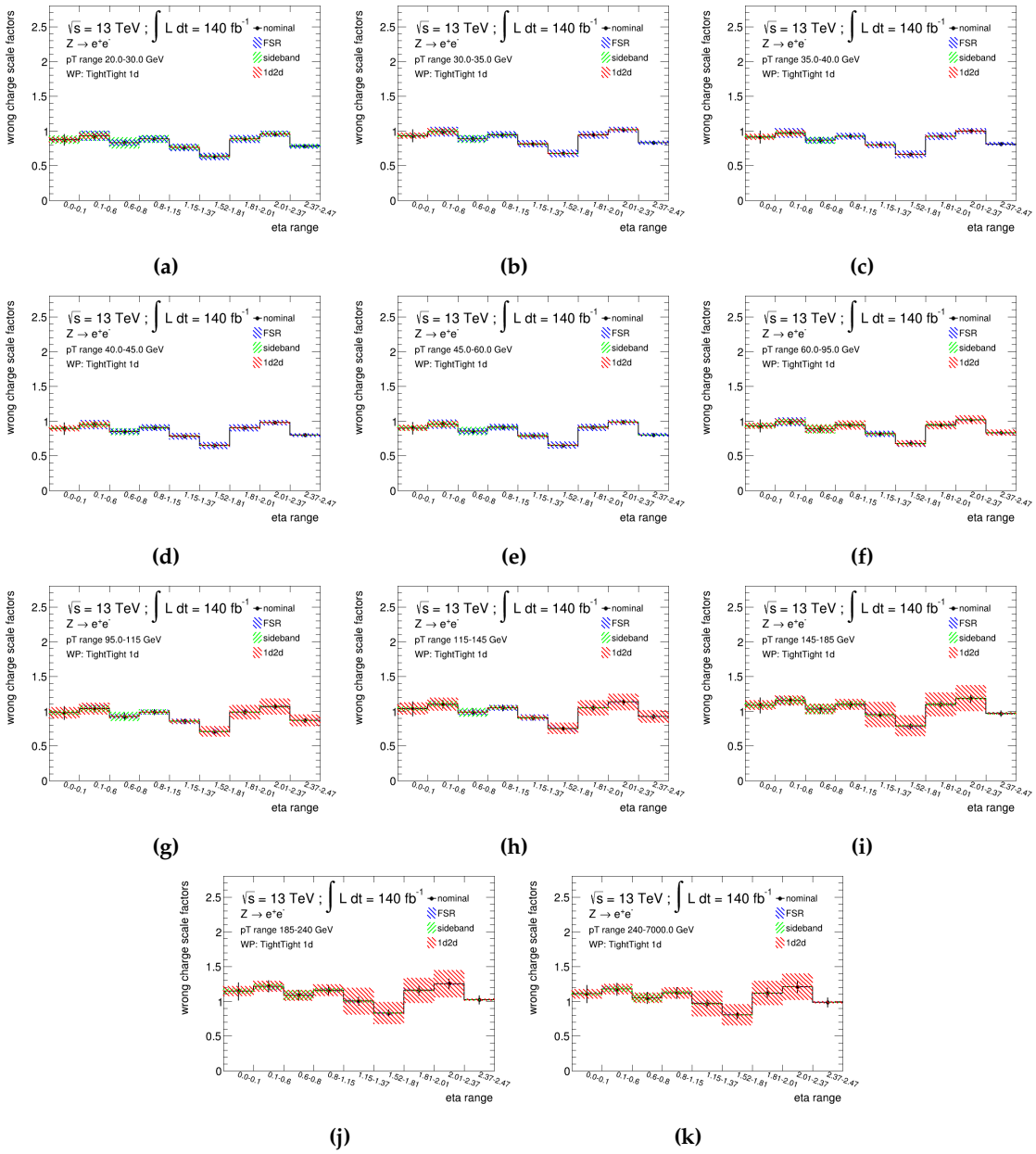

Figure 8.8: Charge misID scale factors for incorrectly reconstructed charged electrons passing `TightLH` identification and `Tight_VarRad` isolation working point . Scale factors are shown for full Run 2 data and corresponding systematic uncertainties from FSR, sideband subtraction and non closure from 1D×1D and 2D parameterization in various p_T slices calculated with the 1D×1D parameterization are also shown.

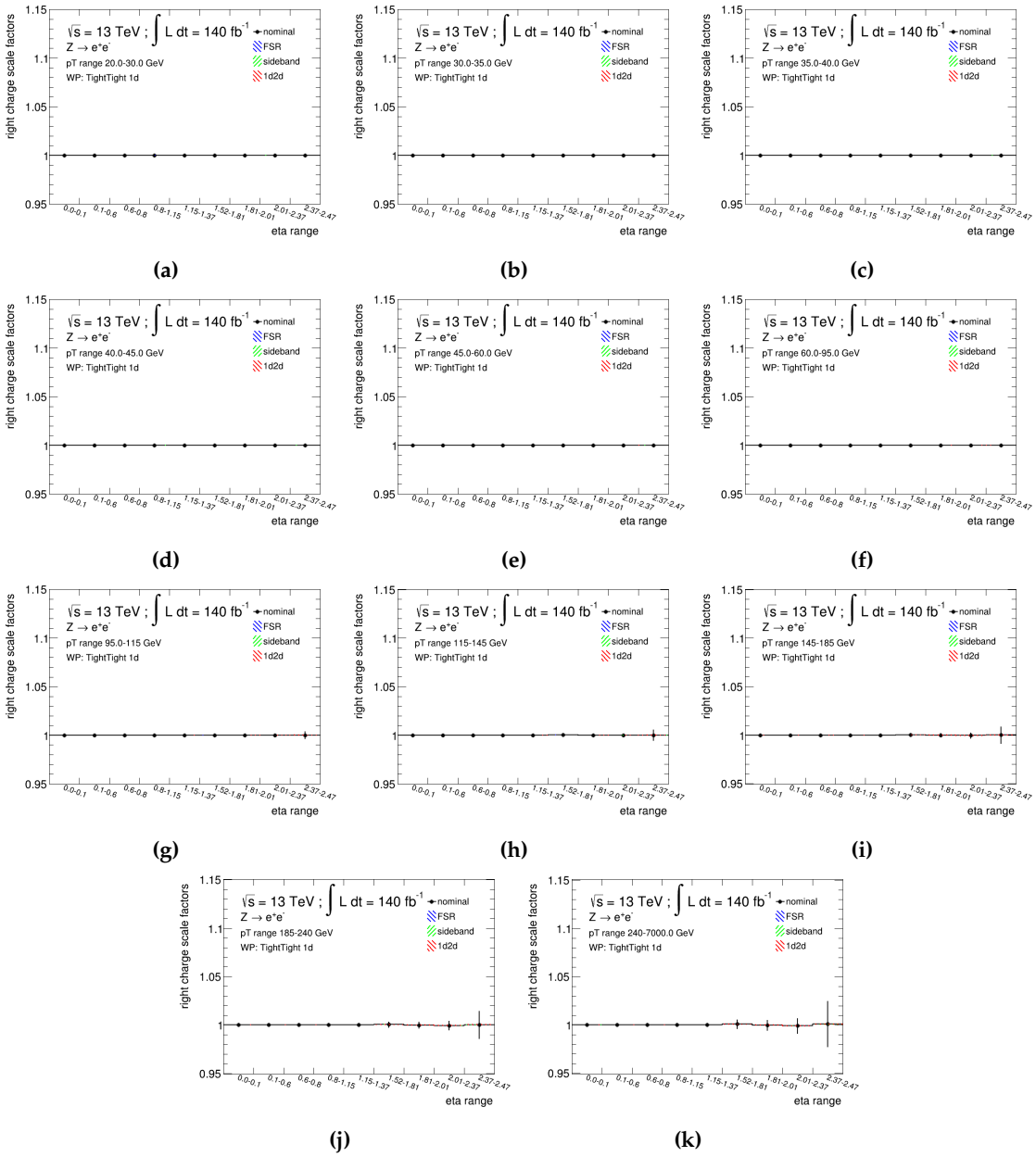

Figure 8.9: Charge misID scale factors for correctly reconstructed charged electrons passing `TightLH` identification and `Tight_VarRad` isolation working point. Scale factors are shown for full Run 2 data and corresponding systematic uncertainties from FSR, sideband subtraction and non closure from 1D×1D and 2D parameterization in various p_T slices calculated with the 1D×1D parameterization are also shown.

8.3 Scale Factors using Likelihood+ECIDS

Electron charge misidentification remains a challenging background to suppress because no single variable can reliably distinguish correctly reconstructed (prompt) electrons from those with misassigned charge. Rather than relying on a single variable, studies have shown that using multiple observables related to track quality, shower shape, and track–cluster matching offers partial discrimination power. A simple cut-based rejection of poorly classified electrons would unnecessarily reduce the efficiency for genuine prompt electrons. To maximize discrimination while maintaining high signal efficiency, a multivariate approach was adopted using a Boosted Decision Tree (BDT) implemented via TMVA (Toolkit for multivariate data analysis) in ROOT. This tool, known as the Electron Charge ID Selector (ECIDS), combines all relevant variables [67] into a single powerful classifier.

Scale factors derived with the electrons passing ECIDS rejection along with `TightLH` identification and `Tight_VarRad` isolation working point are shown in Figure 8.10.

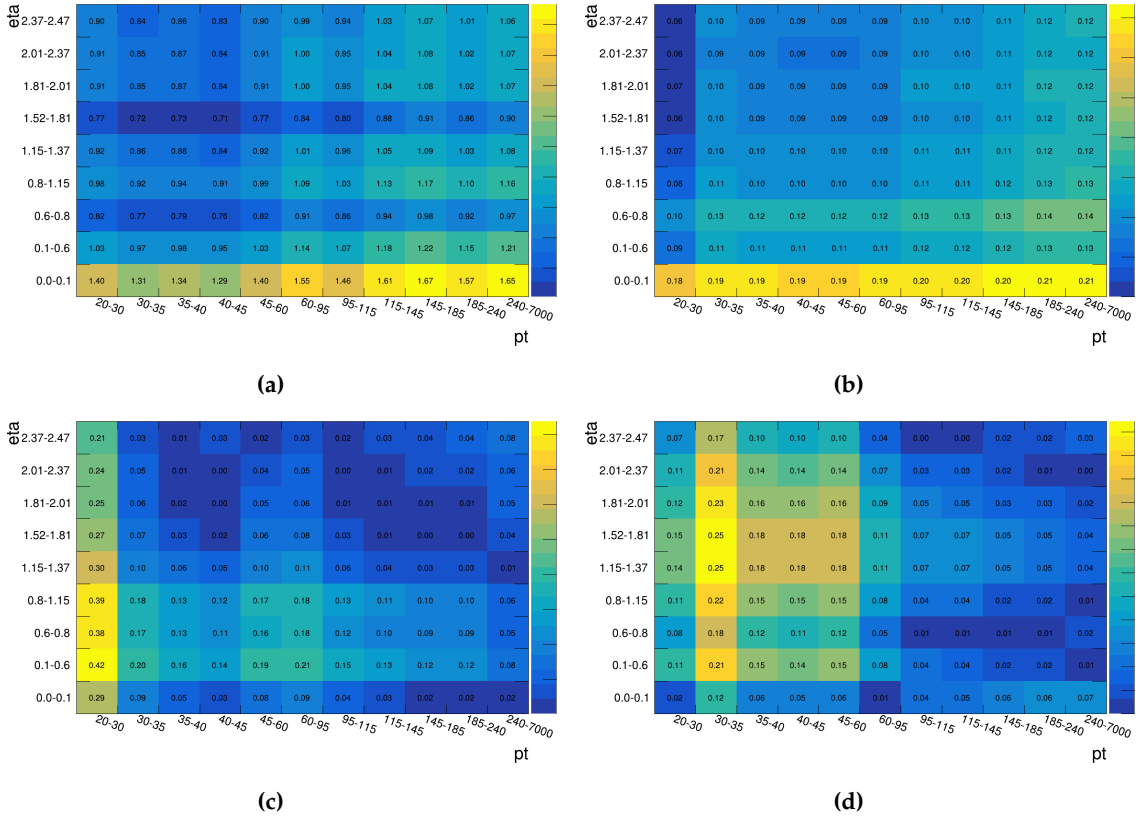

Figure 8.10: Scale factor maps derived with data 2015-2018 and MC campaigns mc20a, mc20d and mc20e for electrons passing `TightLH` identification and `Tight_VarRad` isolation working point along with ECIDS tool. Fine binning with 1D×1D parameterization is used to derive these (a) scale factors for Data/MC (b) statistical uncertainties (c) systematic uncertainties from sideband subtraction (d) systematic uncertainties from FSR subtraction.

8.4 Scale Factors using DNN+CF rejection

A DNN-based electron identification algorithm, integrated with a charge-flip rejection mechanism, offers improved performance in suppressing charge misidentification. Likelihood with ECIDS tool relies on one-dimensional probability density functions (PDFs) and thus assumes that its input variables are uncorrelated while the DNN can also account for correlations between inputs. This ability to capture complex inter-dependencies allows the DNN to extract more discriminating power from the same input variables compared to the LH+ECIDS method. When combined with a dedicated charge-flip (CF) rejection strategy, the DNN not only improves the overall identification performance but also enhances the suppression of electron charge misidentification.

Scale factors derived with the electrons passing `TightDNN` identification are shown in Figures 8.11 and 8.12 for Run 2 data and Run 3 data, respectively.

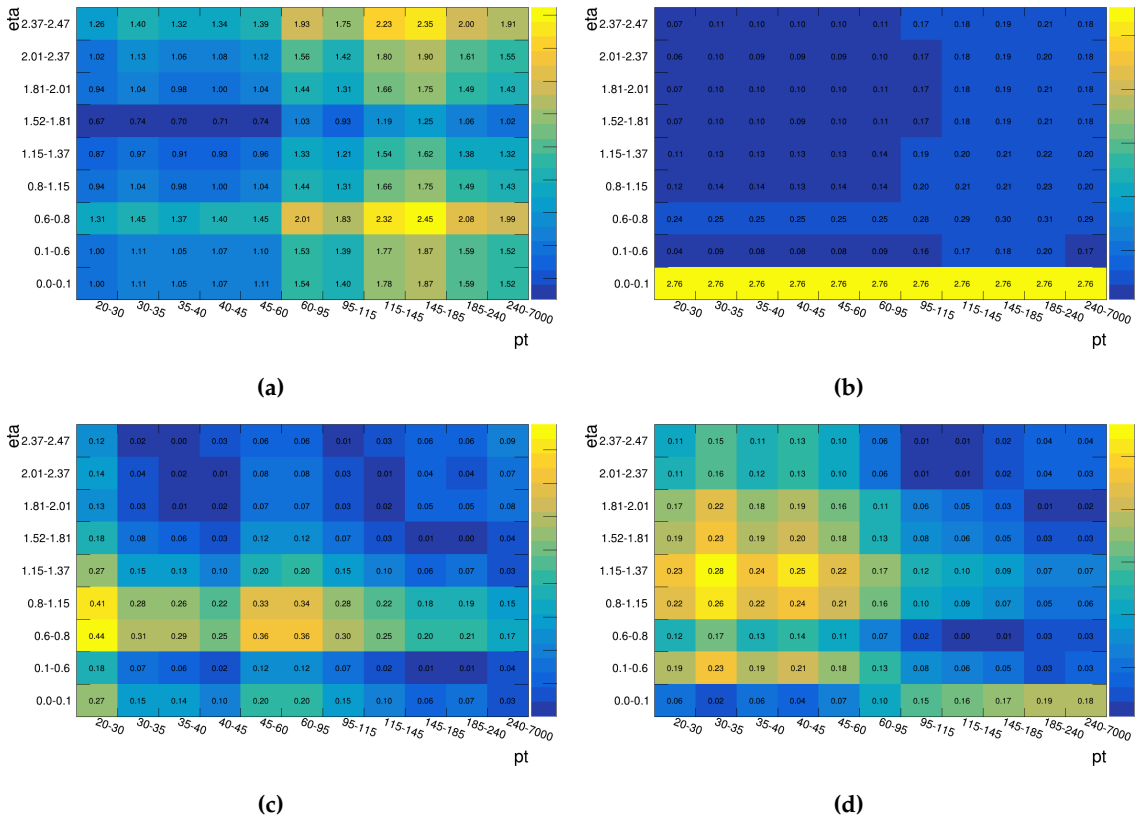

Figure 8.11: Scale factor maps derived with data 2015-2018 and MC campaigns mc20a, mc20d and mc20e for electrons passing `TightDNN` identification with charge-flip rejection.. Fine binning with 1D×1D parameterization is used to derive these (a) scale factors for Data/MC (b) statistical uncertainties (c) systematic uncertainties from sideband subtraction (d) systematic uncertainties from FSR subtraction.

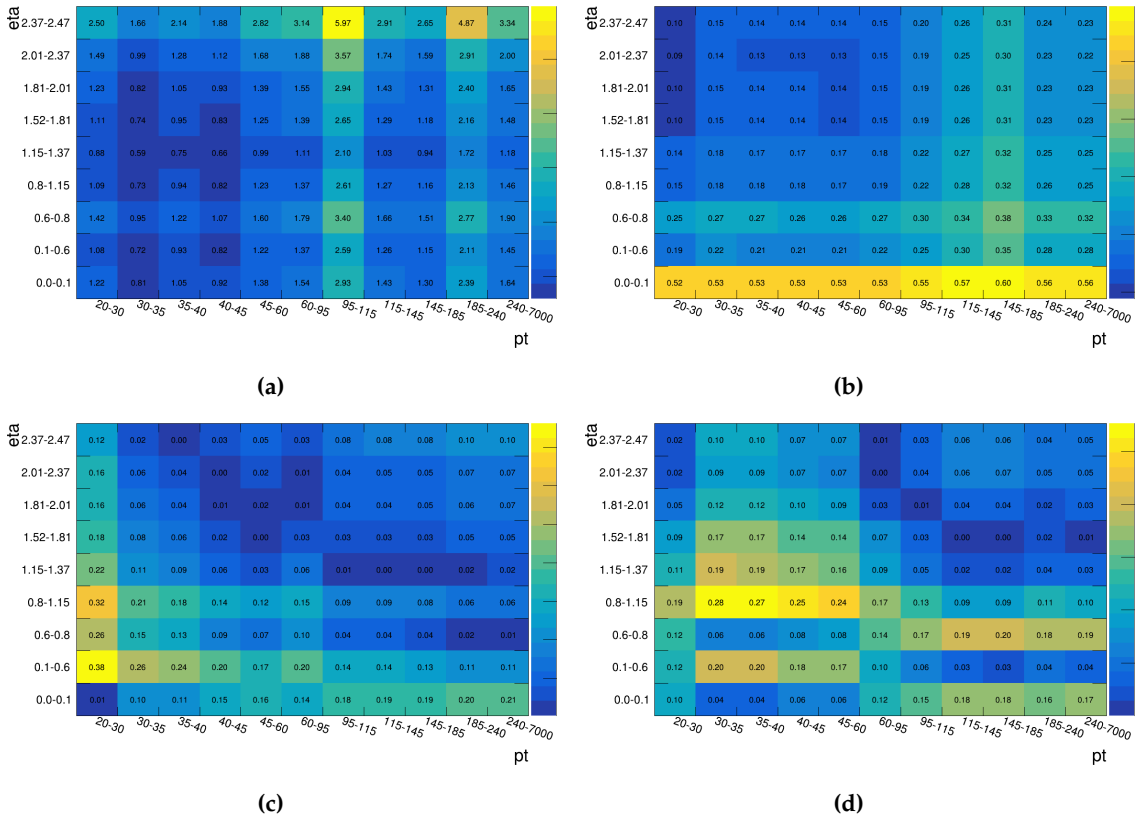

Figure 8.12: Scale factor maps derived with data 2022-2023 and MC campaigns mc23a and mc23d for electrons passing `TightDNN` identification with charge-flip rejection.. Fine binning with 1D×1D parameterization is used to derive these (a) scale factors for Data/MC (b) statistical uncertainties (c) systematic uncertainties from sideband subtraction (d) systematic uncertainties from FSR subtraction.

8.5 Scale Factors Closure Tests

To validate the accuracy of the charge-flip scale factors, closure tests are performed by comparing same-sign di-electron distributions in data and MC for $Z \rightarrow e^+e^- + jets$ events. Figure 8.13 presents the comparison of relevant kinematic observables in the same-sign di-electron channel prior to the application of the scale factors. Significant deviations are visible across multiple bins, particularly in the high p_T and forward η regions, where charge misidentification is more prevalent. The invariant mass distribution further highlights these discrepancies near the Z boson peak, underscoring the need for robust charge-flip corrections. After applying the derived scale factors, Figure 8.14 demonstrates the improved agreement between data and MC for the same set of observables. The improved closure validates the scale factor approach and confirms its effectiveness in mitigating mismodeling of the charge-flip background in analyses using same-sign leptons.

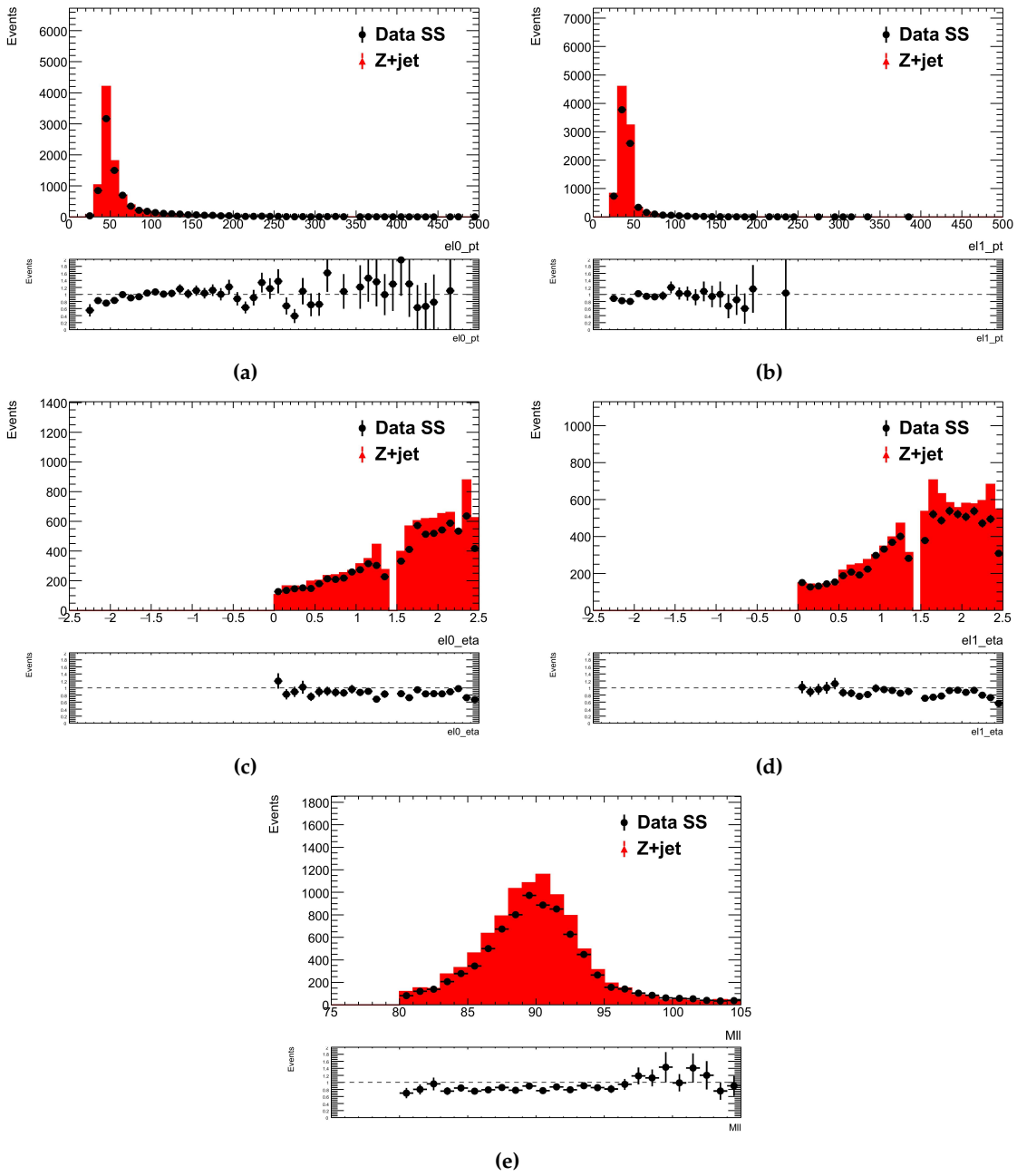

Figure 8.13: Comparison of same-sign di-electron distributions in Data and Simulation (Z+jets) before applying charge-flip SFs.. (a) p_T for leading electron (b) p_T for sub-leading electron (c) η for leading electron (d) η for sub-leading electron (e) invariant mass of di-electron. The bottom panel of each sub-figure shows the ratio of data to Monte Carlo, highlighting discrepancies prior to the correction. These comparisons illustrate the initial level of agreement and motivate the need for applying charge-flip corrections to improve modeling accuracy.

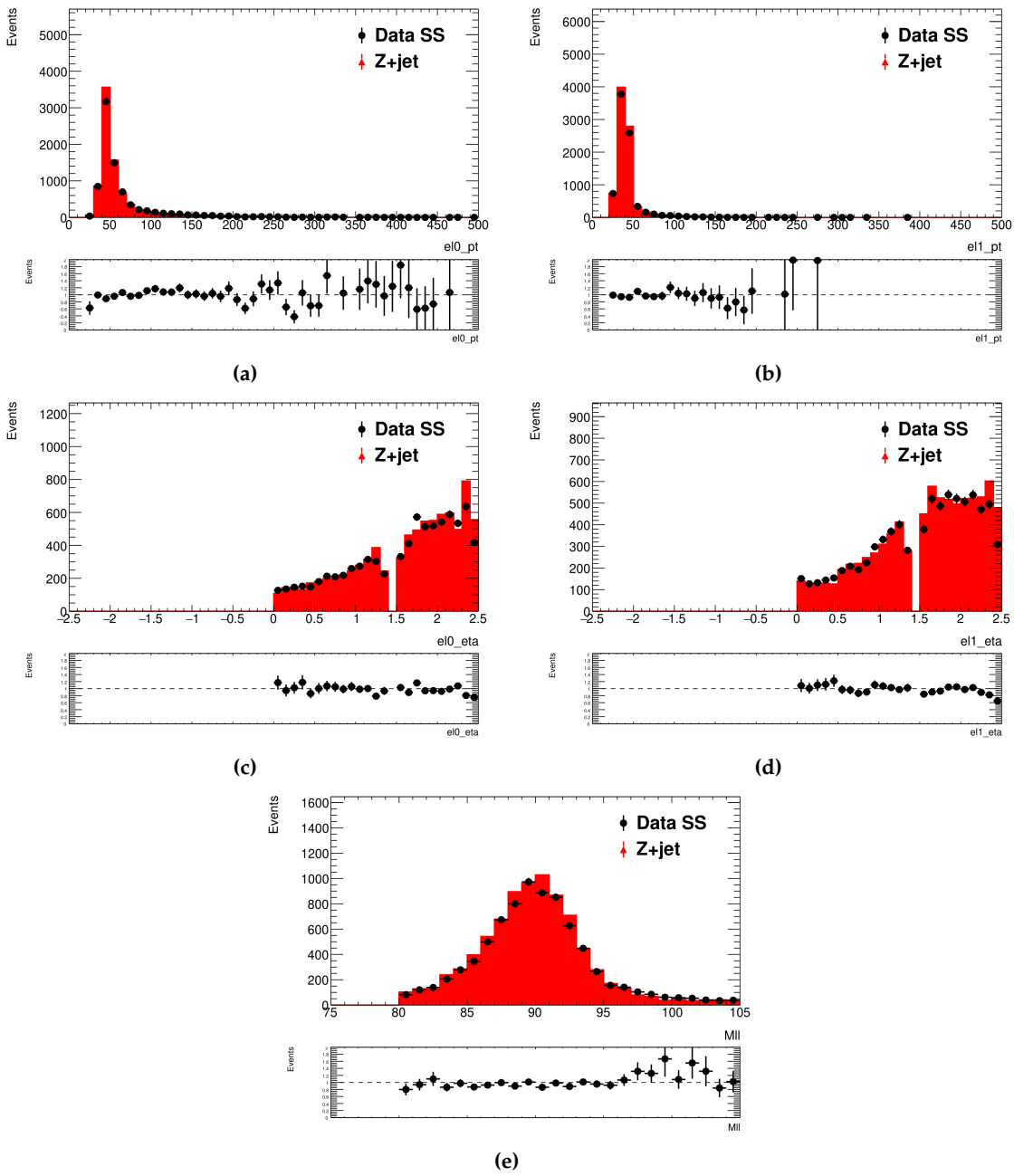

Figure 8.14: Comparison of same-sign di-electron distributions in Data and Simulation (Z+jets) after applying charge-flip SFs.. (a) p_T for leading electron (b) p_T for sub-leading electron (c) η for leading electron (d) η for sub-leading electron (e) invariant mass of di-electron. The bottom panels show the ratio of data to corrected simulation. The improved level of agreement demonstrates the effectiveness of the charge-flip scale factor corrections and validates the method used to derive them.

CHAPTER 9

Discussion

Charge misidentification, where an electron's charge is incorrectly reconstructed, gives rise to so-called charge-flip electrons. These represent a significant background in analyses involving same-sign lepton pairs, such as searches for $t\bar{t}H$, Supersymmetry, doubly-charged Higgs bosons $H++/H+$, and $t\bar{t}t\bar{t}$, as well as in precision measurements sensitive to lepton charge, like the forward-backward asymmetry in $Z \to e^+e^-$ decays. Section 7 outlined the methodology used to extract charge-flip rates using opposite-sign and same-sign control regions enriched in $Z \to e^+e^-$ events. These measured rates, or scale factors when expressed relative to MC predictions, can then be applied to either data control regions or simulated samples. This enables a data-driven estimation of the charge-flip electron background tailored to the needs of each specific analysis. This background is estimated by selecting opposite-sign $Z \to e^+e^-$ events, re-weighting them with the charge-flip rates, and comparing them to the corresponding same-sign events. The event weight used to re-weight the same-sign events is given by:

$$w = \frac{\epsilon_1(1-\epsilon_2) + \epsilon_2(1-\epsilon_1)}{1-(\epsilon_1(1-\epsilon_2) + \epsilon_2(1-\epsilon_1))}, \tag{9.1}$$

where ϵ_1 and ϵ_2 are charge-flip rates for the leading and sub-leading electrons in the opposite-sign event, respectively. The numerator indicates the probability for a same-sign event to arise from an opposite-sign event, while the denominator indicates the probability for an opposite-sign event to remain as opposite-sign.

In Chapter 8, although the 2D parameterization exhibits better closure with respect to the truth-level charge-flip rates, it is also more sensitive to systematic variations such as those induced by the FSR and sideband subtraction. These systematics introduce significant bin-to-bin fluctuations, especially in kinematic regions with limited statistics. In contrast, the 1D $\times$ 1D parameterization provides a more robust and stable estimation of the scale factors under systematic shifts, making it more suitable for the analysis, albeit with slightly poorer closure.

In likelihood fitting method, the expected number of same-sign electron pairs is modeled as shown in equation 7.1 and the charge-flip probabilities are fitted by minimizing the negative log-likelihood function as shown in equation 7.3. The fitting involves estimating ϵ_i and ϵ_j simultaneously for each (p_T

and η) bin. The parameterization assumes $\lambda^{ij} \approx \epsilon_i + \epsilon_j + \mathcal{O}(\epsilon)$. However, due to the strong correlation between ϵ_i and ϵ_j in some bins and the quadratic terms, the likelihood surface can become flat or ill-conditioned, leading to unstable solutions and hence non-convergence in certain (p_T and η) regions. To address this, a calibration-like method is proposed but not yet implemented. In this method the idea is to recover ϵ_i and ϵ_j by solving a linear system of equations, exploiting the relation: $\lambda^{ij} \approx \epsilon_i + \epsilon_j$. Instead of directly minimizing a non-linear likelihood for each pair, the system is linearized per (p_T and η) bin. This linear system can then be constrained and regularized, stabilizing the fit and improving convergence. This method has been tested and found to work well in context of in-situ Z-mass measurements [72] where same kind of 2D likelihood fit is used.

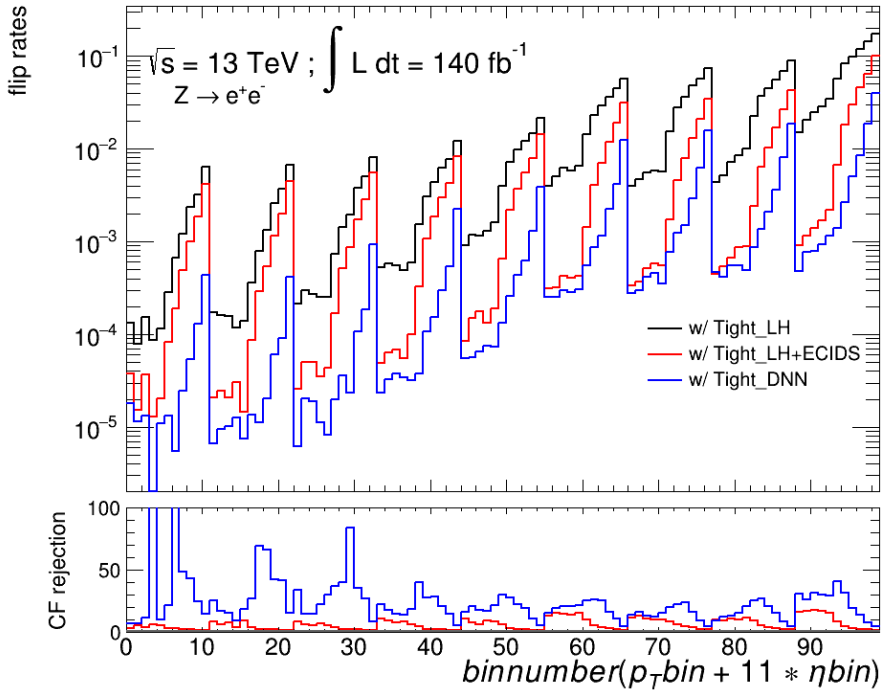

Figure 9.1: Charge flip rejection using ECIDS tool and DNN ID+CF rejection. Using data 2015-2018, the top panel shows the charge-flip rates using likelihood, likelihood+ECIDS and DNN+CF rejection and bottom panel shows the charge-flip rejection due to ECIDS tool and DNN+CF rejection.

Another important thing is to discuss the different methods (ECIDS and DNN+CF rejection algorithm) used to reject the charge flip electrons. During Run 2, the standard approach to suppress charge-flip electrons involved the use of likelihood-based identification in conjunction with ECIDS — a dedicated charge-flip rejection tool based on a Boosted Decision Tree (BDT) multivariate algorithm. ECIDS was specifically trained to discriminate between correctly reconstructed electrons and those with misidentified charge signatures. As part of ongoing improvements in electron identification, a new method based on deep neural networks (DNN ID+CF) is introduced during Run 2 as an alternative to the LH+ECIDS configuration. Although it was under active development at that time, DNN

ID+CF shows promising performance in enhancing charge-flip suppression as shown in Figure 9.1. Moving into Run 3, the ECIDS tool is no longer supported. Consequently, the suppression of charge-flip electrons will rely exclusively on the DNN-based identification algorithm, which is designed to provide improved rejection of charge misidentified electrons while maintaining high signal efficiency.

We discussed the electron efficiencies and different identification and isolation working points in Chapter 5. Different analysis groups make selection of electrons based on different working points (Identification + Isolation). For instance, `Loose + Loose_VarRad` is used in cross-section measurements such as $H \to ZZ^* \to 4l$ [73] and Standard Model ZZ [74] production and `Medium + Tight_VarRad` is used in the measurements of SM WW production [75] and search for VBF production of $H^{\pm}/H^{\pm\pm}$ decaying to same-sign $W^{\pm}W^{\pm}$ and WZ vector bosons. Also, `Tight + Tight_VarRad` is used to study the coupling interactions through the production of an additional Higgs boson referred to as VBS VVh analysis, which studies $W^{\pm}W^{\pm}hqq \to l^{\pm}l^{\pm}\nu\nu bbjj$.

CHAPTER 10

Conclusion

In this thesis, a detailed study of electron charge misidentification in the ATLAS detector has been presented, with a focus on deriving charge-flip scale factors using both Run 2 and partial Run 3 data. The motivation stems from the fact that charge misidentified electrons constitute a non-negligible background in several physics analyses involving same-sign leptons, such as searches for doubly-charged Higgs bosons $H++/H+$.

After a comprehensive theoretical overview and description of the ATLAS detector and datasets, the electron reconstruction, identification, and isolation strategies are detailed with the efficiencies of upto 98-99%, 93% and 91% respectively. Particular attention is given to various working points, including the likelihood and DNN based identification algorithms, and their role in suppressing charge-flip electrons. The ECIDS tool, used in Run 2 for charge-flip suppression, is discussed and compared to the newer DNN ID+CF algorithm adopted in Run 3.

A data-driven methodology is employed to extract charge-flip probabilities using same-sign and opposite-sign $Z \to e^+e^-$ events. These probabilities are parameterized in both 1D×1D and 2D kinematic binning schemes. Scale factors are then derived by comparing the data-driven rates to those predicted by Monte Carlo simulations. To account for biases due to FSR and backgrounds, techniques such as sideband subtraction and FSR correction are implemented and corresponding systematics are added. The maximum scale factors observed with `TightLH` identification and `Tight_VarRad` isolation working point are upto $(25.05 \pm 11.59)\%$. The results indicate that while 1D×1D parameterizations provide stable and robust scale factors, the 2D parameterization suffers from stability issues in regions with limited statistics. Closure tests are performed to validate the derived scale factors, demonstrating good consistency between data and simulation once the scale factors are applied.

This work contributes to the refinement of electron charge-flip background estimation in ATLAS and provides a set of validated scale factors that can be used in various Run 2 and Run 3 analyses. Future improvements could include enhanced training of DNN classifiers for charge-flip suppression, finer binning in well-populated regions, and full Run 3 data once available.

Bibliography

[1] Griffiths David J. Introduction to elementary particles. Physics textbook. New York, NY: Wiley, 2008. URL: https://cds.cern.ch/record/111880.

[2] Purcell Andrew. "Go on a particle quest at the first CERN webfest. Le premier webfest du CERN se lance à la conquête des particules". In: 35/2012 (2012), p. 10. URL: https://cds.cern.ch/record/1473657.

[3] Peskin Michael E. and Schroeder Daniel V. An Introduction to Quantum Field Theory. Boulder, Colorado: Westview Press, 1995. ISBN: 978-0201503975.

[4] Halzen F. and Martin Alan D. Quarks and Leptons: An introductory course in Modern Particle Physics. 1984. ISBN: 978-0-471-88741-6.

[5] Yukawa Hideki. "On the Interaction of Elementary Particles". In: Progress of Theoretical Physics Supplement 1 (Jan. 1955), pp. 1–10. ISSN: 0375-9687. DOI: 10.1143/PTPS.1.1. eprint: https://academic.oup.com/ptps/article-pdf/doi/10.1143/PTPS.1.1/5310694/1-1.pdf. URL: https://doi.org/10.1143/PTPS.1.1.

[6] Skands P. Introduction to QCD. World Scientific, 2013. DOI: 10.1142/9789814525220_0008. URL: http://dx.doi.org/10.1142/9789814525220_0008.

[7] Weinberg Steven. "A Model of Leptons". In: Phys. Rev. Lett. 19 (21 Nov. 1967), pp. 1264–1266. DOI: 10.1103/PhysRevLett.19.1264. URL: https://link.aps.org/doi/10.1103/PhysRevLett.19.1264.

[8] Glashow Sheldon L. "Partial-symmetries of weak interactions". In: Nuclear Physics 22.4 (1961), pp. 579–588. ISSN: 0029-5582. DOI: https://doi.org/10.1016/0029-5582(61)90469-2. URL: https://www.sciencedirect.com/science/article/pii/0029558261904692.

[9] Englert F. and Brout R. "Broken Symmetry and the Mass of Gauge Vector Mesons". In: Phys. Rev. Lett. 13 (1964). Ed. by Taylor J. C., pp. 321–323. DOI: 10.1103/PhysRevLett.13.321.

[10] Higgs Peter W. "Broken Symmetries and the Masses of Gauge Bosons". In: Phys. Rev. Lett. 13 (16 Oct. 1964), pp. 508–509. DOI: 10.1103/PhysRevLett.13.508. URL: https://link.aps.org/doi/10.1103/PhysRevLett.13.508.

[11] Ellis John, Gaillard Mary K., and Nanopoulos Dimitri V. A Historical Profile of the Higgs Boson. WORLD SCIENTIFIC, Aug. 2016, pp. 255–274. DOI: 10.1142/9789814733519_0014. URL: http://dx.doi.org/10.1142/9789814733519_0014.

[12] ATLAS Collaboration. "Observation of a new particle in the search for the Standard Model Higgs boson with the ATLAS detector at the LHC". In: Physics Letters B 716.1 (Sept. 2012), pp. 1–29. ISSN: 0370-2693. DOI: 10.1016/j.physletb.2012.08.020. URL: http://dx.doi.org/10.1016/j.physletb.2012.08.020.

[13] CMS Collaboration. "Observation of a new boson at a mass of 125 GeV with the CMS experiment at the LHC". In: Physics Letters B 716.1 (Sept. 2012), pp. 30–61. ISSN: 0370-2693. DOI: 10.1016/j.physletb.2012.08.021. URL: http://dx.doi.org/10.1016/j.physletb.2012.08.021.

[14] Horejsi Jiri. Fundamentals of electroweak theory. 2022. arXiv: 2210.04526 [hep-ph]. URL: https://arxiv.org/abs/2210.04526.

[15] Drell Sidney D. and Yan Tung-Mow. "Massive Lepton-Pair Production in Hadron-Hadron Collisions at High Energies". In: Phys. Rev. Lett. 25 (5 Aug. 1970), pp. 316–320. DOI: 10.1103/PhysRevLett.25.316. URL: https://link.aps.org/doi/10.1103/PhysRevLett.25.316.

[16] Bagnaia P. et al. "Evidence for $Z^0 \to e^+e$ at the CERN p-p collider". In: Physics Letters B 129.1 (1983), pp. 130–140. ISSN: 0370-2693. DOI: https://doi.org/10.1016/0370-2693(83)90744-X. URL: https://www.sciencedirect.com/science/article/pii/037026938390744X.

[17] Baglio Julien et al. "Inclusive production cross sections at N3LO". In: Journal of High Energy Physics 2022.12 (Dec. 2022). ISSN: 1029-8479. DOI: 10.1007/jhep12(2022)066. URL: http://dx.doi.org/10.1007/JHEP12(2022)066.

[18] Duhr Claude, Dulat Falko, and Mistlberger Bernhard. "Charged current Drell-Yan production at N3LO". In: Journal of High Energy Physics 2020.11 (Nov. 2020). ISSN: 1029-8479. DOI: 10.1007/jhep11(2020)143. URL: http://dx.doi.org/10.1007/JHEP11(2020)143.

[19] Florian Daniel de, Der Manuel, and Fabre Ignacio. "NNLO corrections to Drell-Yan production". In: Physical Review D 98.9 (Nov. 2018). ISSN: 2470-0029. DOI: 10.1103/physrevd.98.094008. URL: http://dx.doi.org/10.1103/PhysRevD.98.094008.

[20] Group Particle Data. "Review of Particle Physics". In: Progress of Theoretical and Experimental Physics 2020.8 (Aug. 2020), p. 083C01. ISSN: 2050-3911. DOI: 10.1093/ptep/ptaa104. eprint: https://academic.oup.com/ptep/article-pdf/2020/8/083C01/34673722/ptaa104.pdf. URL: https://doi.org/10.1093/ptep/ptaa104.

[21] The ATLAS Collaboration webpage. URL: https://atlas.cern/Discover/Collaboration.

[22] CERN. LEP design report. Copies shelved as reports in LEP, PS and SPS libraries. Geneva, 1984. URL: https://cds.cern.ch/record/102083.

[23] Smith C. "Genesis of the large hadron collider". In: Philosophical Transactions of the Royal Society A: Mathematical, Physical and Engineering Sciences 373 (2032 2015), p. 20140037. DOI: 10.1098/rsta.2014.0037.

[24] The ATLAS Collaboration. Public Results. URL: https://twiki.cern.ch/twiki/bin/view/AtlasPublic/LuminosityPublicResultsRun2#Luminosity_Plots_for_multiple_Ru.

[25] ATLAS Collaboration. "Luminosity determination in pp collisions at $\sqrt{s} = 13$ TeV using the ATLAS detector at the LHC". In: The European Physical Journal C 83.10 (Oct. 2023). ISSN: 1434-6052. DOI: 10.1140/epjc/s10052-023-11747-w. URL: http://dx.doi.org/10.1140/epjc/s10052-023-11747-w.

[26] CERN. Linear accelerator 4. CERN Science Home Page. 2022. URL: https://home.cern/science/accelerators/linear-accelerator-4.

[27] CERN. Linear accelerator 2. CERN Science Home Page. 2022. URL: https://home.cern/science/accelerators/linear-accelerator-2.

[28] Welton Robert et al. "Negative hydrogen ion sources for particle accelerators: Sustainability issues and recent improvements in long-term operations". In: J. Phys. Conf. Ser. 2244.1 (2022), p. 012045. DOI: 10.1088/1742-6596/2244/1/012045.

[29] CERN. The Proton Synchrotron Booster. CERN Science Home Page. 2022. URL: https://home.cern/science/accelerators/proton-synchrotron-booster.

[30] CERN. CERN Home Page. URL: https://home.cern/science/engineering/accelerating-radiofrequency-cavities#:~:text=In%20the%20LHC%2C%20each%20RF,energy%20will%20not%20be%20accelerated..

[31] Lopienska Ewa. "The CERN accelerator complex, layout in 2022. Complexe des accélérateurs du CERN en janvier 2022". In: (2022). General Photo. URL: https://cds.cern.ch/record/2742791/files/ATL-COM-PHYS-2020-757.pdf?version=2.

[32] ATLAS Collaboration. "The ATLAS Experiment at the CERN Large Hadron Collider". In: Journal of Instrumentation 3.08 (Aug. 2008), S08003. DOI: 10.1088/1748-0221/3/08/S08003. URL: https://dx.doi.org/10.1088/1748-0221/3/08/S08003.

[33] ATLAS Collaboration. "The ATLAS experiment at the CERN Large Hadron Collider: a description of the detector configuration for Run 3". In: Journal of Instrumentation 19.05 (May 2024), P05063. ISSN: 1748-0221. DOI: 10.1088/1748-0221/19/05/p05063. URL: http://dx.doi.org/10.1088/1748-0221/19/05/P05063.

[34] ATLAS Collaboration. "Study of the material of the ATLAS inner detector for Run 2 of the LHC". In: Journal of Instrumentation 12.12 (Dec. 2017), P12009. DOI: 10.1088/1748-0221/12/12/P12009. URL: https://dx.doi.org/10.1088/1748-0221/12/12/P12009.

[35] ATLAS Collaboration. "ATLAS pixel detector electronics and sensors". In: Journal of Instrumentation 3.07 (July 2008), P07007. DOI: 10.1088/1748-0221/3/07/P07007. URL: https://dx.doi.org/10.1088/1748-0221/3/07/P07007.

[36] ATLAS Collaboration. "Production and integration of the ATLAS Insertable B-Layer". In: Journal of Instrumentation 13.05 (May 2018), T05008–T05008. ISSN: 1748-0221. DOI: 10.1088/1748-0221/13/05/t05008. URL: http://dx.doi.org/10.1088/1748-0221/13/05/T05008.

[37] ATLAS Collaboration. "Operation and performance of the ATLAS semiconductor tracker". In: Journal of Instrumentation 9.08 (Aug. 2014), P08009–P08009. ISSN: 1748-0221. DOI: 10.1088/1748-0221/9/08/p08009. URL: http://dx.doi.org/10.1088/1748-0221/9/08/P08009.

[38] Mindur Bartosz. "ATLAS Transition Radiation Tracker (TRT): Straw tubes for tracking and particle identification at the Large Hadron Collider". In: Nuclear Instruments and Methods in Physics Research 845 (2017). Proceedings of the Vienna Conference on Instrumentation 2016, pp. 257–261. ISSN: 0168-9002. DOI: https://doi.org/10.1016/j.nima.2016.04.026. URL: https://www.sciencedirect.com/science/article/pii/S0168900216301905.

[39] Fabjan Christian W. and Gianotti Fabiola. "Calorimetry for particle physics". In: Rev. Mod. Phys. 75 (4 Oct. 2003), pp. 1243–1286. DOI: 10.1103/RevModPhys.75.1243. URL: https://link.aps.org/doi/10.1103/RevModPhys.75.1243.

[40] Koletsou Iro. "The ATLAS liquid argon calorimeter at the LHC". In: Nuclear Instruments and Methods in Physics Research 628.1 (2011). VCI 2010, pp. 351–354. ISSN: 0168-9002. DOI: https://doi.org/10.1016/j.nima.2010.06.351. URL: https://www.sciencedirect.com/science/article/pii/S016890021001541X.

[41] "ATLAS muon spectrometer". In: Technical design report. ATLAS (1997). URL: https://cds.cern.ch/record/331068.

[42] Dubbert J. et al. "Test, integration and commissioning of monitored drift tube chambers for the ATLAS Barrel Muon Spectrometer". In: PoS HEP2005 (2006). Ed. by Barreira Gaspar, p. 390. DOI: 10.22323/1.021.0390.

[43] Cattani Giordano. "The resistive plate chambers of the ATLAS experiment: Performance studies". In: J. Phys. Conf. Ser. 280 (2011). Ed. by Cannuccia E. et al., p. 012001. DOI: 10.1088/1742-6596/280/1/012001.

[44] D'Amico Valerio. The New Small Wheel upgrade project of the ATLAS Experiment. 2022. DOI: 10.22323/1.398.0756.

[45] ATLAS Collaboration. "Operation of the ATLAS trigger system in Run 2". In: Journal of Instrumentation 15.10 (Oct. 2020), P10004–P10004. ISSN: 1748-0221. DOI: 10.1088/1748-0221/15/10/p10004. URL: http://dx.doi.org/10.1088/1748-0221/15/10/P10004.

[46] Scannicchio D A. "ATLAS trigger and data acquisition". In: Nucl. Instrum. Methods Phys. Res., A 617.1-3 (2010), pp. 306–309. DOI: 10.1016/j.nima.2009.06.114. URL: https://cds.cern.ch/record/1290345.

[47] ATLAS Collaboration. "Performance of the missing transverse momentum triggers for the ATLAS detector during Run-2 data taking". In: Journal of High Energy Physics 2020.8 (Aug. 2020). ISSN: 1029-8479. DOI: 10.1007/jhep08(2020)080. URL: http://dx.doi.org/10.1007/JHEP08(2020)080.

[48] Ruiz-Martinez Aranzazu and Collaboration ATLAS. "The Run-2 ATLAS Trigger System". In: (2016). DOI: 10.1088/1742-6596/762/1/012003. URL: https://cds.cern.ch/record/2133909.

[49] ATLAS Collaboration. "The ATLAS experiment at the CERN Large Hadron Collider: a description of the detector configuration for Run 3". In: JINST 19.05 (2024), P05063. DOI: 10.1088/1748-0221/19/05/P05063. arXiv: 2305.16623 [physics.ins-det].

[50] Sjöstrand Torbjörn et al. "An introduction to PYTHIA 8.2". In: Comput. Phys. Commun. 191 (2015), pp. 159–177. DOI: 10.1016/j.cpc.2015.01.024. arXiv: 1410.3012 [hep-ph].

[51] Buckley Andy et al. "General-purpose event generators for LHC physics". In: Physics Reports 504.5 (July 2011), pp. 145–233. ISSN: 0370-1573. DOI: 10.1016/j.physrep.2011.03.005. URL: http://dx.doi.org/10.1016/j.physrep.2011.03.005.

[52] Sherpa Manual. Version 2.2.15. URL: https://sherpa.hepforge.org/doc/SHERPA-MC-2.2.15.html.

[53] Bothmann Enrico et al. "Event generation with Sherpa 2.2". In: SciPost Physics 7.3 (Sept. 2019). ISSN: 2542-4653. DOI: 10.21468/scipostphys.7.3.034. URL: http://dx.doi.org/10.21468/SciPostPhys.7.3.034.

[54] Alwall Johan et al. "MadGraph 5: going beyond". In: Journal of High Energy Physics 2011.6 (June 2011). ISSN: 1029-8479. DOI: 10.1007/jhep06(2011)128. URL: http://dx.doi.org/10.1007/JHEP06(2011)128.

[55] Alwall J. et al. "The automated computation of tree-level and next-to-leading order differential cross sections, and their matching to parton shower simulations". In: Journal of High Energy Physics 2014.7 (July 2014). ISSN: 1029-8479. DOI: 10.1007/jhep07(2014)079. URL: http://dx.doi.org/10.1007/JHEP07(2014)079.

[56] Oleari C. "The POWHEG BOX". In: Nuclear Physics B - Proceedings Supplements 205–206 (Aug. 2010), pp. 36–41. ISSN: 0920-5632. DOI: 10.1016/j.nuclphysbps.2010.08.016. URL: http://dx.doi.org/10.1016/j.nuclphysbps.2010.08.016.

[57] Agostinelli S. et al. "GEANT4 - A Simulation Toolkit". In: Nucl. Instrum. Meth. A 506 (2003), pp. 250–303. DOI: 10.1016/S0168-9002(03)01368-8.

[58] ATLAS Collaboration. "Electron and photon performance measurements with the ATLAS detector using the 2015–2017 LHC proton-proton collision data". In: Journal of Instrumentation 14.12 (Dec. 2019), P12006–P12006. ISSN: 1748-0221. DOI: 10.1088/1748-0221/14/12/p12006. URL: http://dx.doi.org/10.1088/1748-0221/14/12/P12006.

[59] ATLAS Collaboration. "Electron reconstruction and identification in the ATLAS experiment using the 2015 and 2016 LHC proton–proton collision data at $\sqrt{s} = 13$ TeV". In: The European Physical Journal C 79.8 (Aug. 2019). ISSN: 1434-6052. DOI: 10.1140/epjc/s10052-019-7140-6. URL: http://dx.doi.org/10.1140/epjc/s10052-019-7140-6.

[60] ATLAS Collaboration. "Electron and photon energy calibration with the ATLAS detector using 2015–2016 LHC proton-proton collision data". In: Journal of Instrumentation 14.03 (Mar. 2019), P03017–P03017. ISSN: 1748-0221. DOI: 10.1088/1748-0221/14/03/p03017. URL: http://dx.doi.org/10.1088/1748-0221/14/03/P03017.

[61] ATLAS Collaboration. "Electron and photon efficiencies in LHC Run 2 with the ATLAS experiment". In: Journal of High Energy Physics 2024.5 (May 2024). ISSN: 1029-8479. DOI: 10.1007/jhep05(2024)162. URL: http://dx.doi.org/10.1007/JHEP05(2024)162.

[62] ATLAS Collaboration. Electron efficiency measurements with the ATLAS detector using the 2015 LHC proton-proton collision data. Tech. rep. Geneva: CERN, 2016. URL: https://cds.cern.ch/record/2157687.

[63] ATLAS Collaboration. Identification of electrons using a deep neural network in the ATLAS experiment. Tech. rep. Geneva: CERN, 2022. URL: https://cds.cern.ch/record/2809283.

[64] Hoecker A. et al. "TMVA - Toolkit for Multivariate Data Analysis". In: (2009). arXiv: physics/0703039 [physics.data-an]. URL: https://arxiv.org/abs/physics/0703039.

[65] ATLAS Collaboration. "Electron efficiency with full Run2". In: (). URL: https://atlas.web.cern.ch/Atlas/GROUPS/PHYSICS/PLOTS/EGAM-2022-02/.

[66] Fernandez Pretel Jose Antonio. "Estimation of the electron charge misidentification background for the same-sign WW measurement with the ATLAS detector at $\sqrt{s} = 13TeV$". In: (Mar. 2020).

[67] Arguin Jean-Francois et al. "Support Note for Electron ID: charge mis-identification". In: (2017). URL: https://cds.cern.ch/record/2273365.

[68] ATLAS Collaboration. ATLAS MC Truth Classifier. URL: https://twiki.cern.ch/twiki/bin/viewauth/AtlasProtected/MCTruthClassifier.

[69] FastFrames Package, GitLab. URL: https://gitlab.cern.ch/atlas-amglab/fastframes.

[70] FastFrames Documentation. URL: https://atlas-project-topreconstruction.web.cern.ch/fastframesdocumentation/latest/.

[71] Fred James and Michel Goossens. "MINUIT – Function Minimization and Error Analysis". In: (1994). CERN Program Library entry D506. URL: https://root.cern.ch/download/minuit.pdf.

[72] Guo Linghua et al. "Electron energy in-situ calibration and linearity measurements from Z $\rightarrow$ *ee*". In: (2020). URL: https://cds.cern.ch/record/2742791.

[73] ATLAS Collaboration. "Measurement of the $H \to \gamma\gamma$ and $H \to ZZ^* \to 4l$ cross-sections in pp collisions at $\sqrt{s} = 13.6$ TeV with the ATLAS detector". In: Eur. Phys. J. C 84 (2024). Published 24 Jan 2024, p. 78. DOI: 10.1140/epjc/s10052-023-12130-5. URL: https://doi.org/10.1140/epjc/s10052-023-12130-5.

[74] ATLAS Collaboration. "$Z \to l^+l^-l'^+l'^-$ cross-section measurements and search for anomalous triple gauge couplings in 13 TeV collisions with the ATLAS detector". In: Physical Review D 97.3 (Feb. 2018). ISSN: 2470-0029. DOI: 10.1103/physrevd.97.032005. URL: http://dx.doi.org/10.1103/PhysRevD.97.032005.

[75] ATLAS Collaboration. "Measurement of fiducial and differential W^+W^- production cross-sections at $\sqrt{s} = 13$ TeV with the ATLAS detector". In: The European Physical Journal C 79.10 (Oct. 2019). ISSN: 1434-6052. DOI: 10.1140/epjc/s10052-019-7371-6. URL: http://dx.doi.org/10.1140/epjc/s10052-019-7371-6.

APPENDIX A

Charge misID rates for different working points

This appendix presents the charge misidentification (mis-ID) rates for different identification and isolation working points.

- Figures A.1 and A.2 shows the charge mis-ID rates for Run 2 and Run 3 data, repectively. In these results, electrons are passing the `MediumLH` identification and `Tight_VarRad` isolation working point.
- Figures A.3 and A.4 shows the charge mis-ID rates for Run 2 and Run 3 data, repectively. In these results, electrons are passing the `LooseLH` identification and `Tight_VarRad` isolation working point.

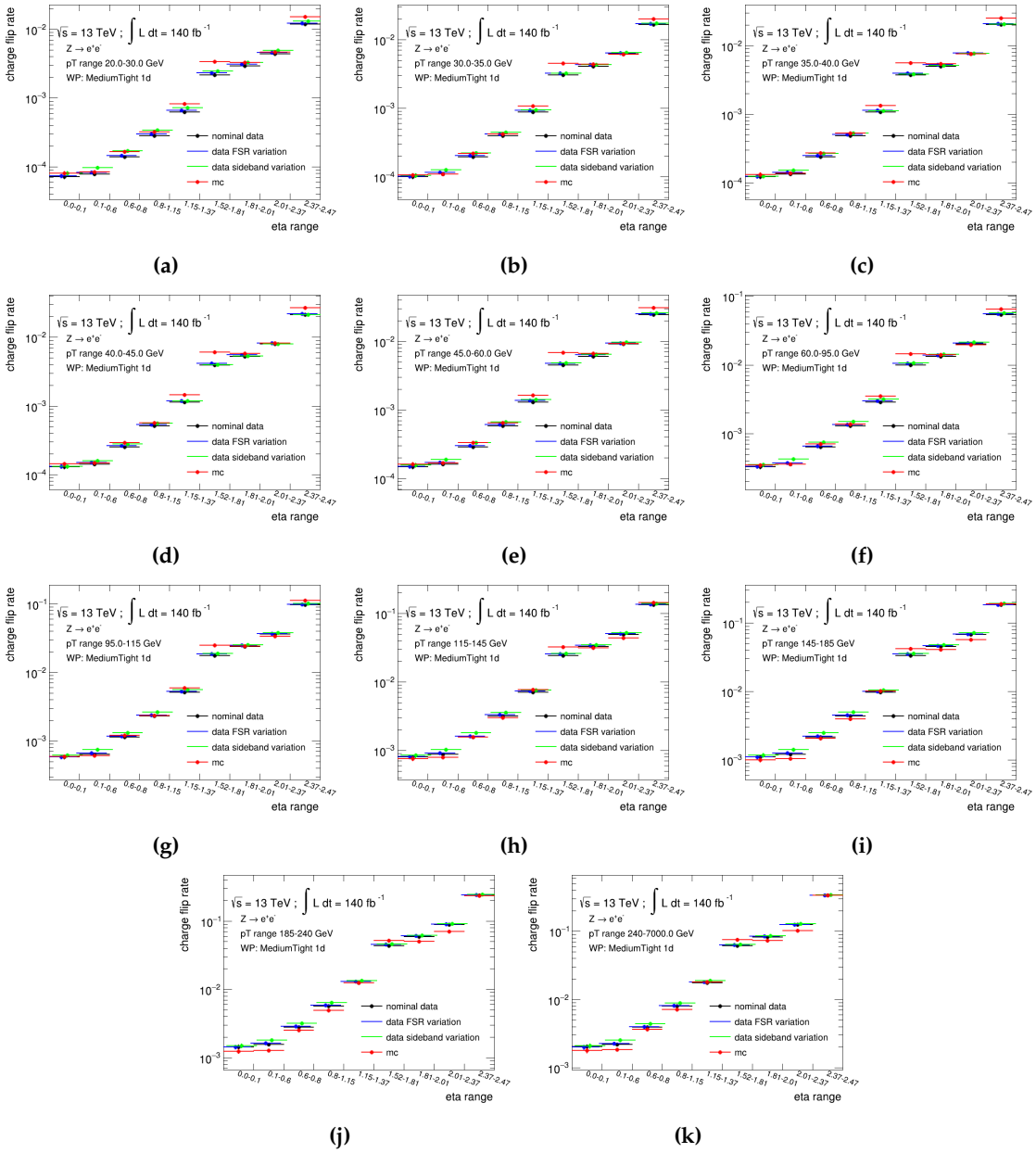

Figure A.1: Charge misID rates for the electrons passing the `MediumLH` identification and `Tight_VarRad` isolation working point. These rates are derived using full Run 2 data (2015-2018) and MC campaigns mc20a, mc20d and mc20e. Each subfigure corresponds to a different bin in electron p_T, with the charge flip rate plotted as a function of $|\eta|$. (a–c): Low p_T region (20–45 GeV) showing lower flip rates, but still showing η dependence. (d–h): Intermediate p_T (45–145 GeV) showing moderate flip rates with clear forward-region rise, (i–k): High p_T(>145 GeV) showing low statistics, but flip rates remain high at large η.

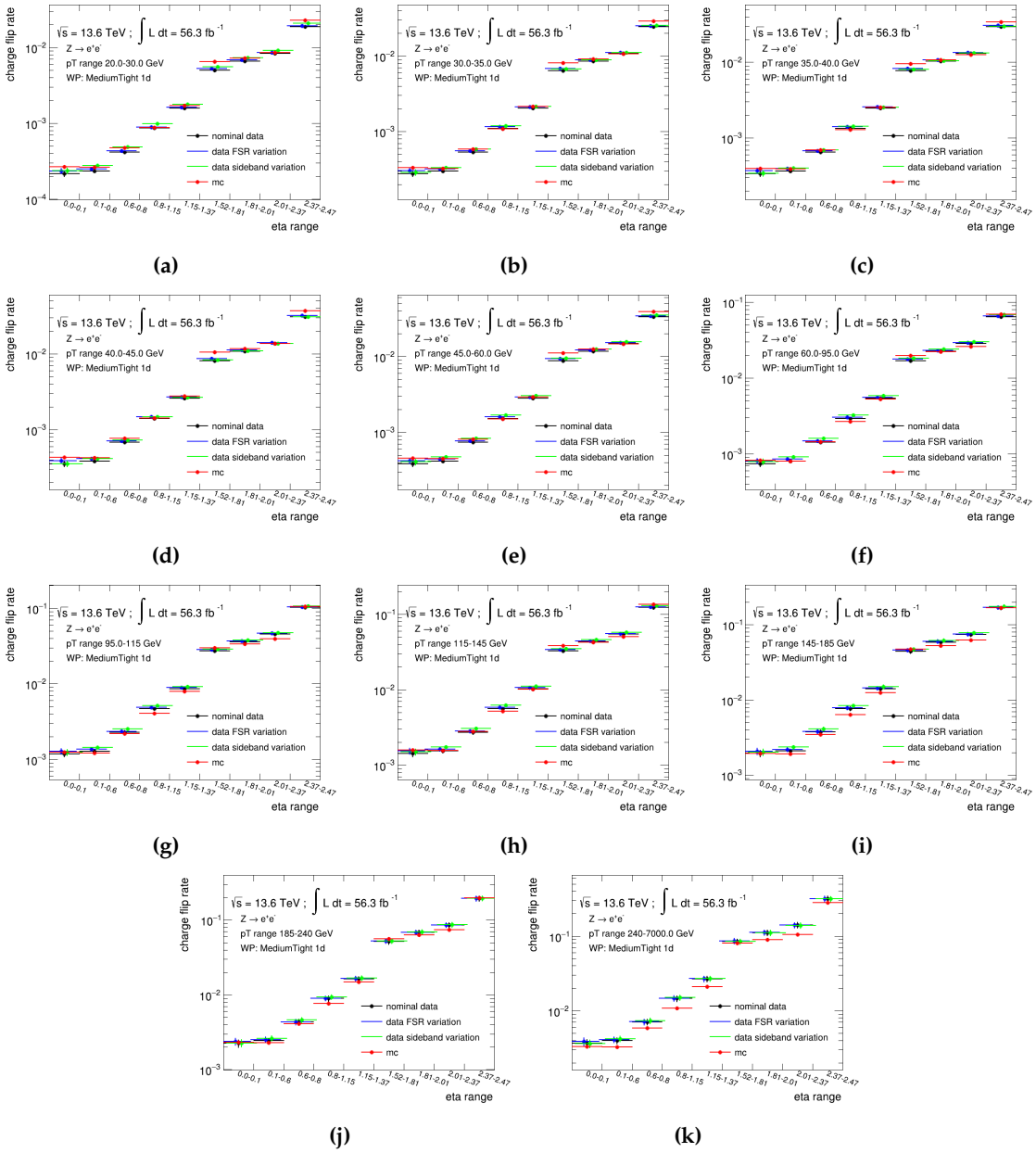

Figure A.2: Charge misID rates passing the `MediumLH` identification and `Tight_VarRad` isolation working point. These rates are derived using Run 3 data (2022-2023) and MC campaigns mc23a and mc23d. Each subfigure corresponds to a different bin in electron p_T, with the charge flip rate plotted as a function of $|\eta|$. (a–c): Low p_T region (20–45 GeV) showing lower flip rates, but still showing η dependence. (d–h): Intermediate p_T (45–145 GeV) showing moderate flip rates with clear forward-region rise, (i–k): High p_T(>145 GeV) showing low statistics, but flip rates remain high at large η.

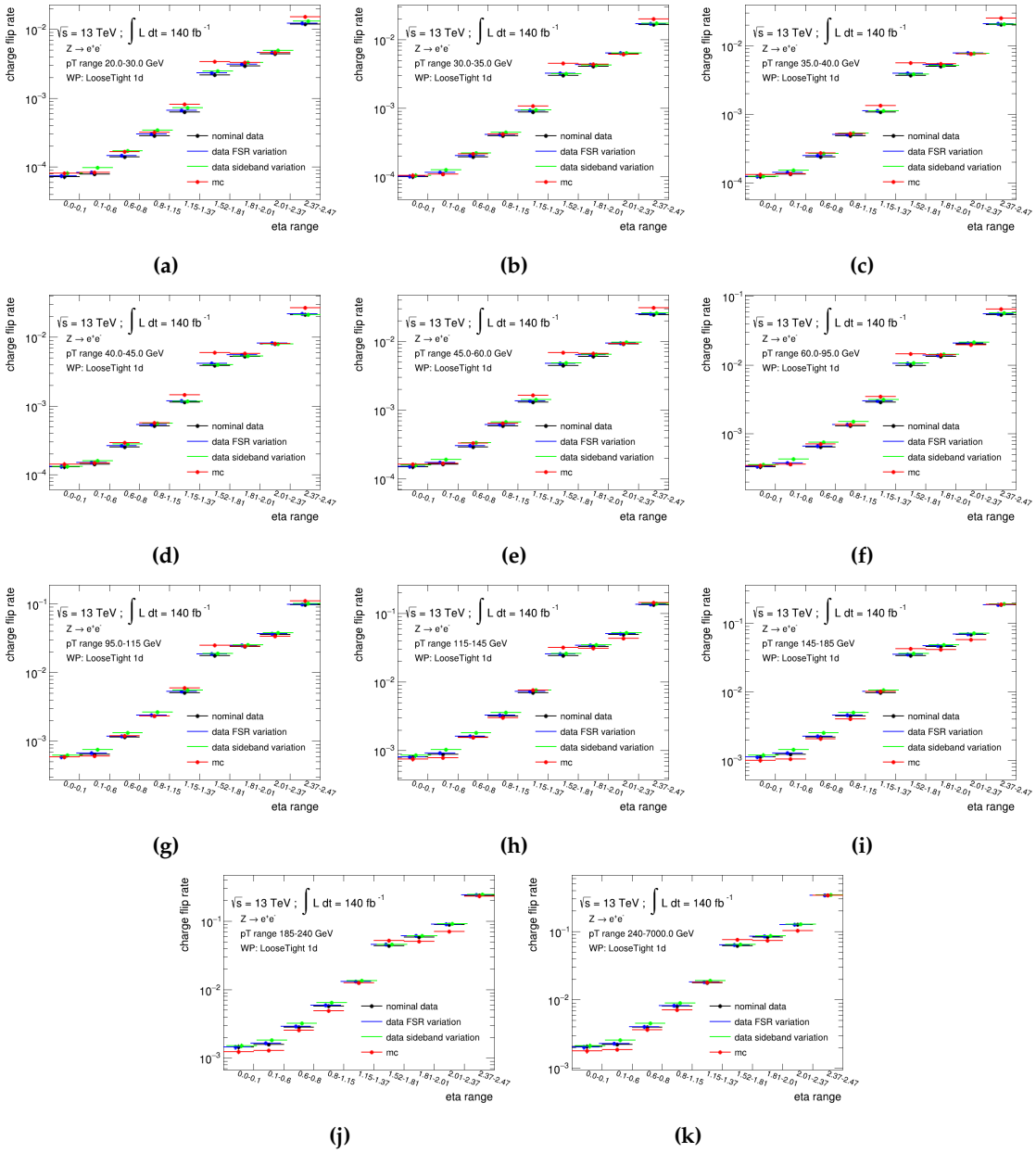

Figure A.3: Charge misID rates passing the `LooseLH` identification and `Tight_VarRad` isolation working point. These rates are derived using full Run 2 data (2015-2018) and MC campaigns mc20a, mc20d and mc20e. Each subfigure corresponds to a different bin in electron p_T, with the charge flip rate plotted as a function of $|\eta|$. (a–c): Low p_T region (20–45 GeV) showing lower flip rates, but still showing η dependence. (d–h): Intermediate p_T (45–145 GeV) showing moderate flip rates with clear forward-region rise, (i–k): High p_T(>145 GeV) showing low statistics, but flip rates remain high at large η.

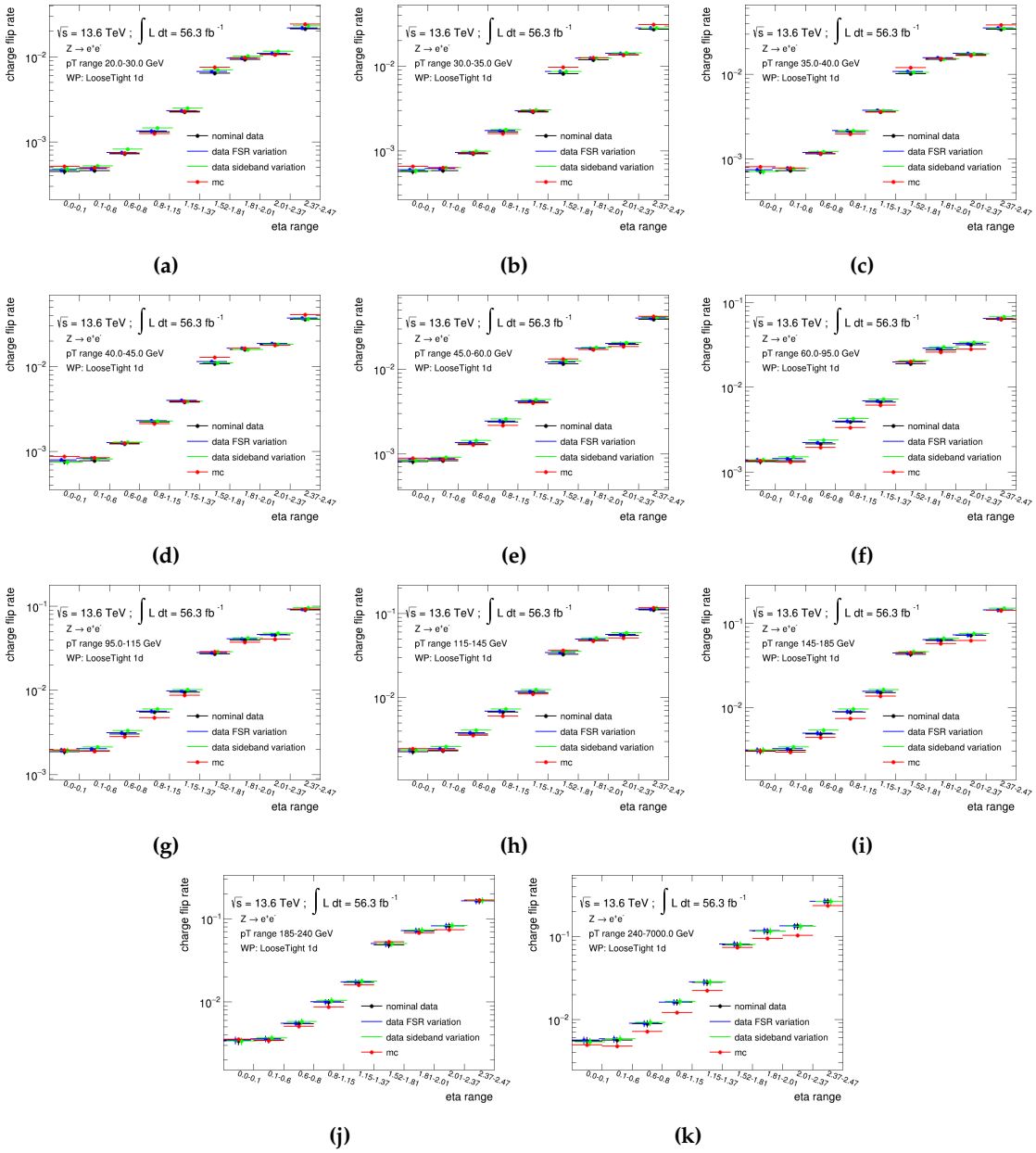

Figure A.4: Charge misID rates passing the `LooseLH` identification and `Tight_VarRad` isolation working point. These rates are derived using Run 3 data (2022-2024) and MC campaigns mc23a and mc23d. Each subfigure corresponds to a different bin in electron p_T, with the charge flip rate plotted as a function of $|\eta|$. (a–c): Low p_T region (20–45 GeV) showing lower flip rates, but still showing η dependence. (d–h): Intermediate p_T (45–145 GeV) showing moderate flip rates with clear forward-region rise, (i–k): High p_T(>145 GeV) showing low statistics, but flip rates remain high at large η.

APPENDIX B

Charge misID scale factors for different working points

This appendix presents the charge misidentification (mis-ID) scale factors for different identification and isolation working points.

- Figures B.1 and B.2 shows the charge mis-ID scale factors for Run 2 and Run 3 data, repectively. In these results, electrons are passing the `MediumLH` identification and `Tight_VarRad` isolation working point.
- Figure B.3 shows the charge mis-ID scale factors for Run 2 data. In these results, electrons are passing the `MediumLH` identification and `Tight_VarRad` isolation working point along with ECIDS tool.
- Figure B.4 shows the charge mis-ID scale factors for Run 3 data. In these results, electrons are passing the `MediumDNN` identification along with CF rejection tool.
- Figures B.5 and B.6 shows the charge mis-ID scale factors for Run 2 and Run 3 data, repectively. In these results, electrons are passing the `LooseLH` identification and `Tight_VarRad` isolation working point.
- Figure B.7 shows the charge mis-ID scale factors for Run 2 data. In these results, electrons are passing the `LooseLH` identification and `Tight_VarRad` isolation working point along with ECIDS tool.
- Figures B.8 and B.9 shows the charge mis-ID scale factors for Run 2 and Run 3 data, respectively. In these results, electrons are passing the `LooseDNN` identification along with CF rejection tool.
- Figures B.10 and B.11shows the charge mis-ID scale factors for incorrectly reconstructed charged electrons passing the `MediumLH` and `LooseLH` identification with `Tight_VarRad` isolation working point, respectively using Run 2 data.

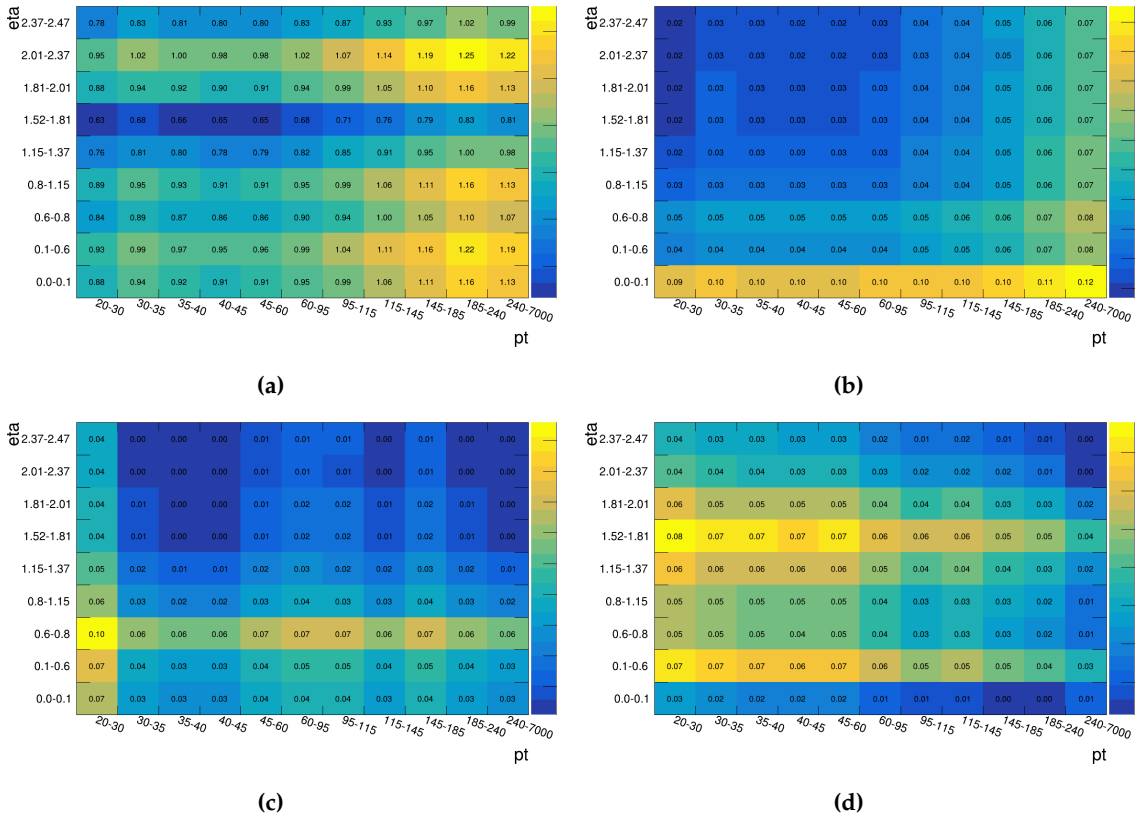

Figure B.1: Scale factor maps derived with Run 2 data taken in 2015-2018 and MC campaigns mc20a, mc20d and mc20e for electrons passing `MediumLH` identification and `Tight_VarRad` isolation working point. Fine binning with 1D×1D parameterization is used to derive these (a) scale factors for Data/MC (b) statistical uncertainties (c) systematic uncertainties from sideband subtraction (d) systematic uncertainties from FSR subtraction.

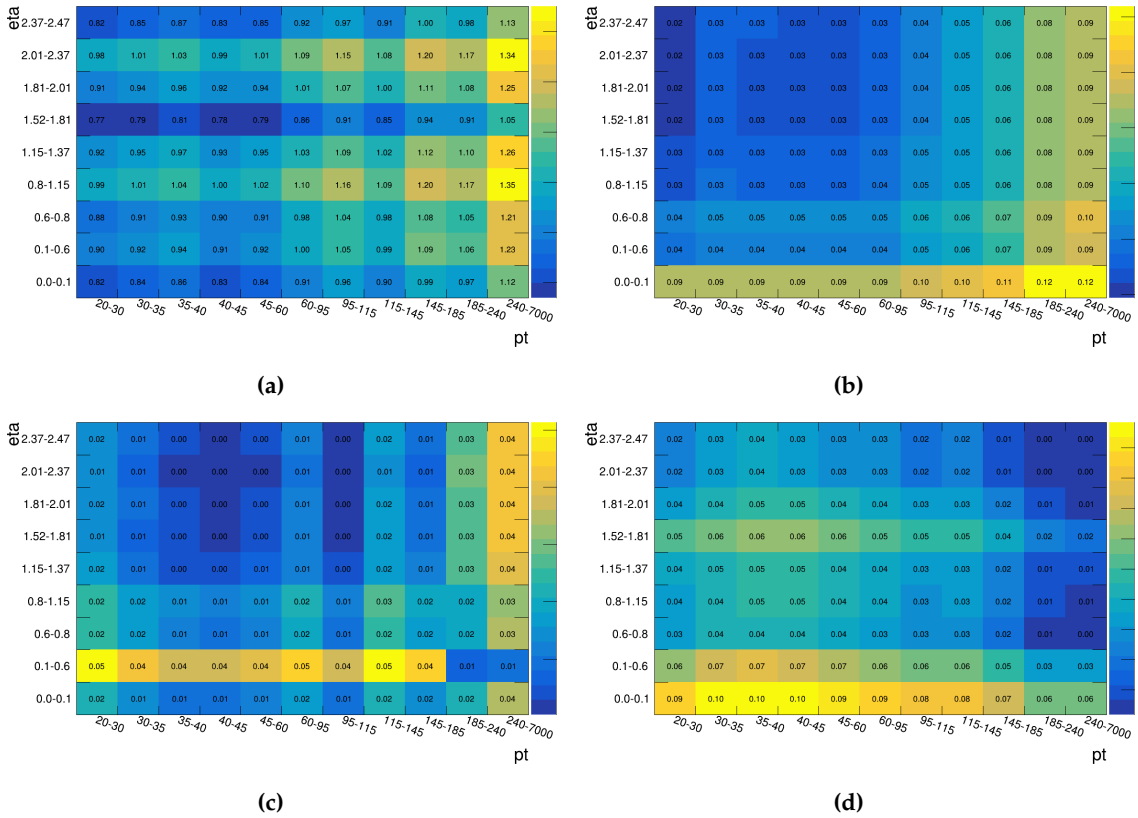

Figure B.2: Scale factor maps derived with Run 3 data taken in 2022-2023 and MC campaigns mc23a and mc23d for electrons passing `MediumLH` identification and `Tight_VarRad` isolation working point. Fine binning with 1D×1D parameterization is used to derive these (a) scale factors for Data/MC (b) statistical uncertainties (c) systematic uncertainties from sideband subtraction (d) systematic uncertainties from FSR subtraction.

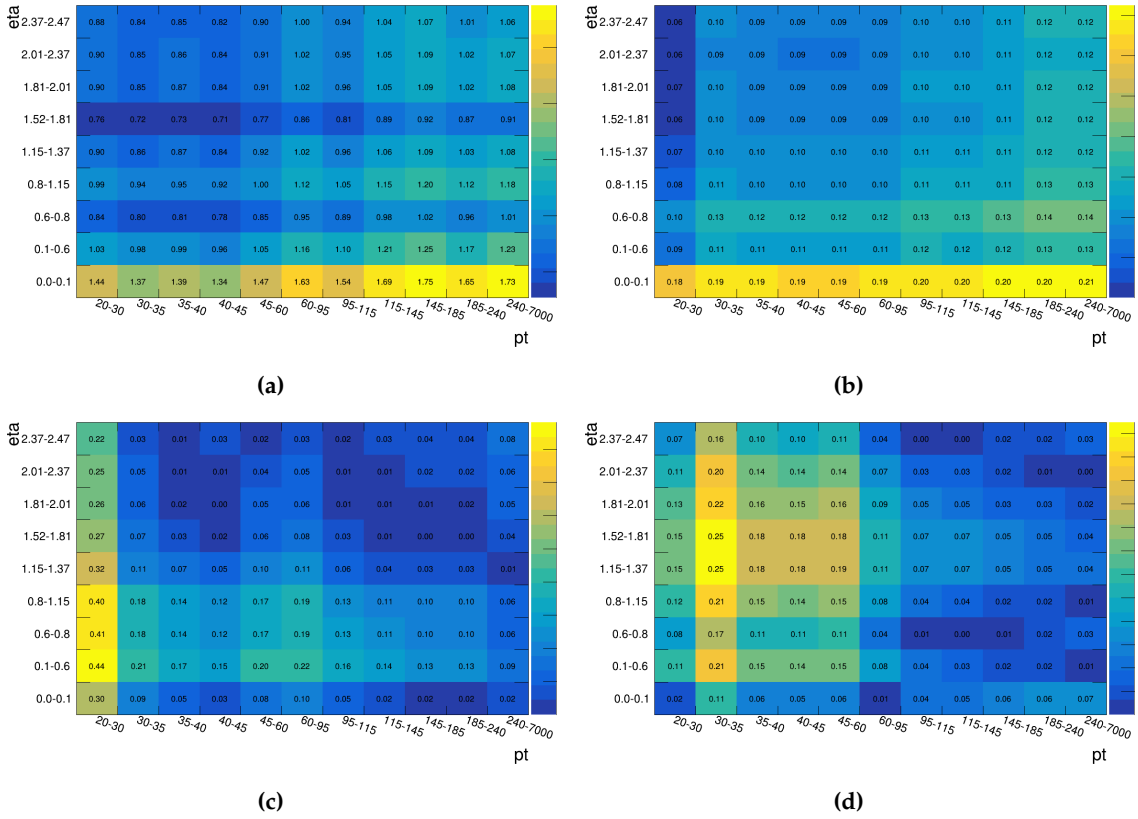

Figure B.3: Scale factor maps derived with Run 2 data taken in 2015-2018 and MC campaigns mc20a, mc20d and mc20e for electrons passing `MediumLH` identification and `Tight_VarRad` isolation working point along with ECIDS tool. Fine binning with 1D×1D parameterization is used to derive these (a) scale factors for Data/MC (b) statistical uncertainties (c) systematic uncertainties from sideband subtraction (d) systematic uncertainties from FSR subtraction.

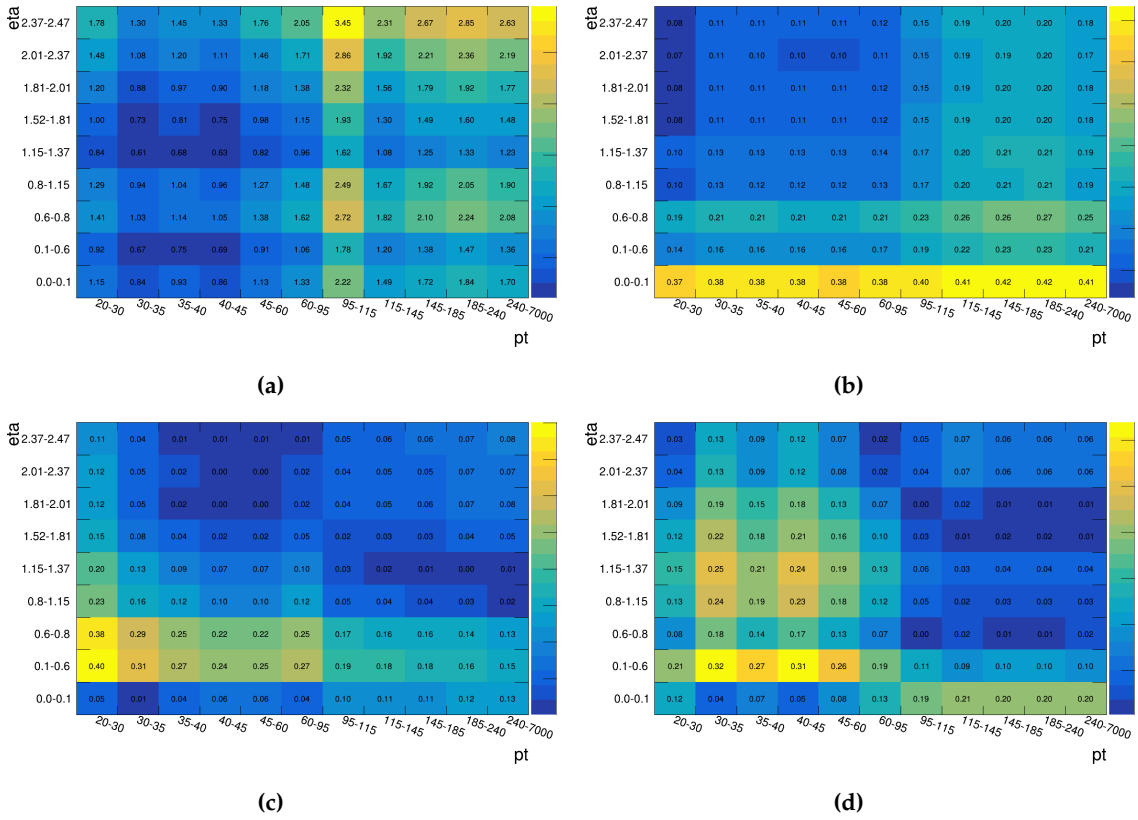

Figure B.4: Scale factor maps derived with Run 3 data taken in 2022-2023 and MC campaigns mc23a and mc23d for electrons passing `MediumDNN` identification with charge-flip rejection. Fine binning with 1D×1D parameterization is used to derive these (a) scale factors for Data/MC (b) statistical uncertainties (c) systematic uncertainties from sideband subtraction (d) systematic uncertainties from FSR subtraction.

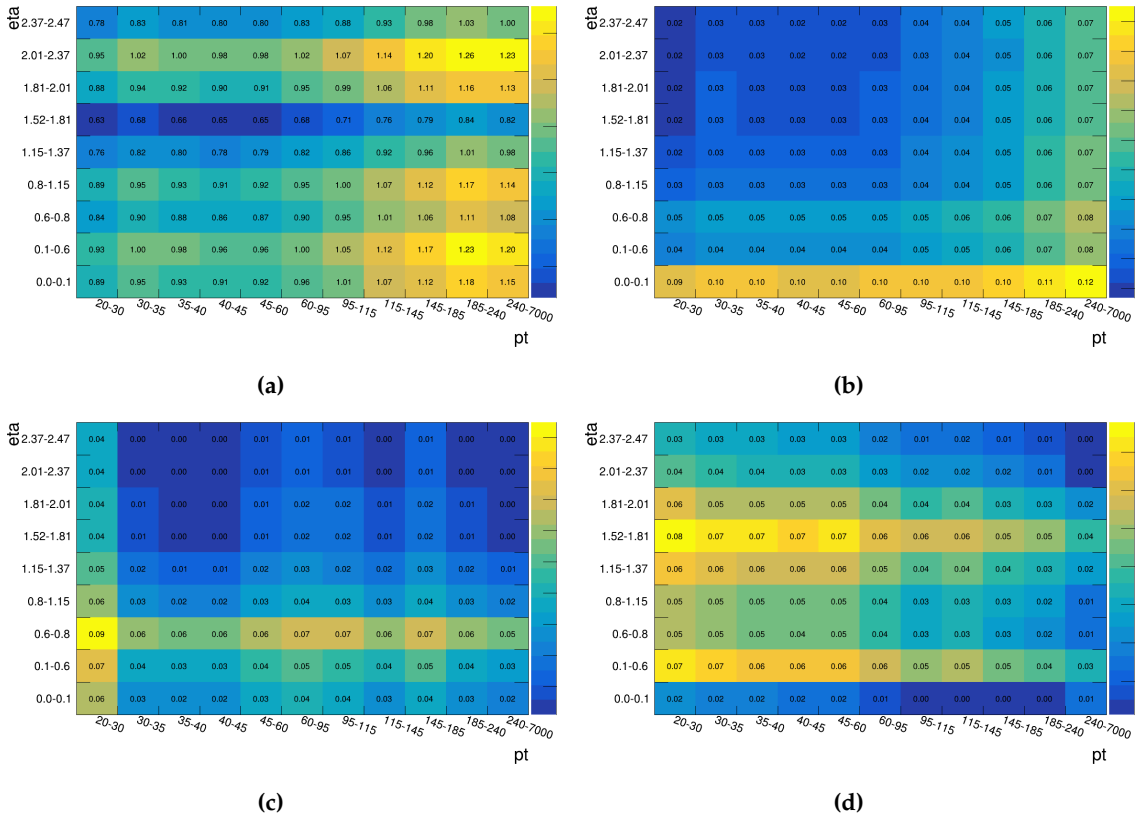

Figure B.5: Scale factor maps derived with Run 2 data taken in 2015-2018 and MC campaigns mc20a, mc20d and mc20e for electrons passing `LooseLH` identification and `Tight_VarRad` isolation working point. Fine binning with 1D×1D parameterization is used to derive these (a) scale factors for Data/MC (b) statistical uncertainties (c) systematic uncertainties from sideband subtraction (d) systematic uncertainties from FSR subtraction.

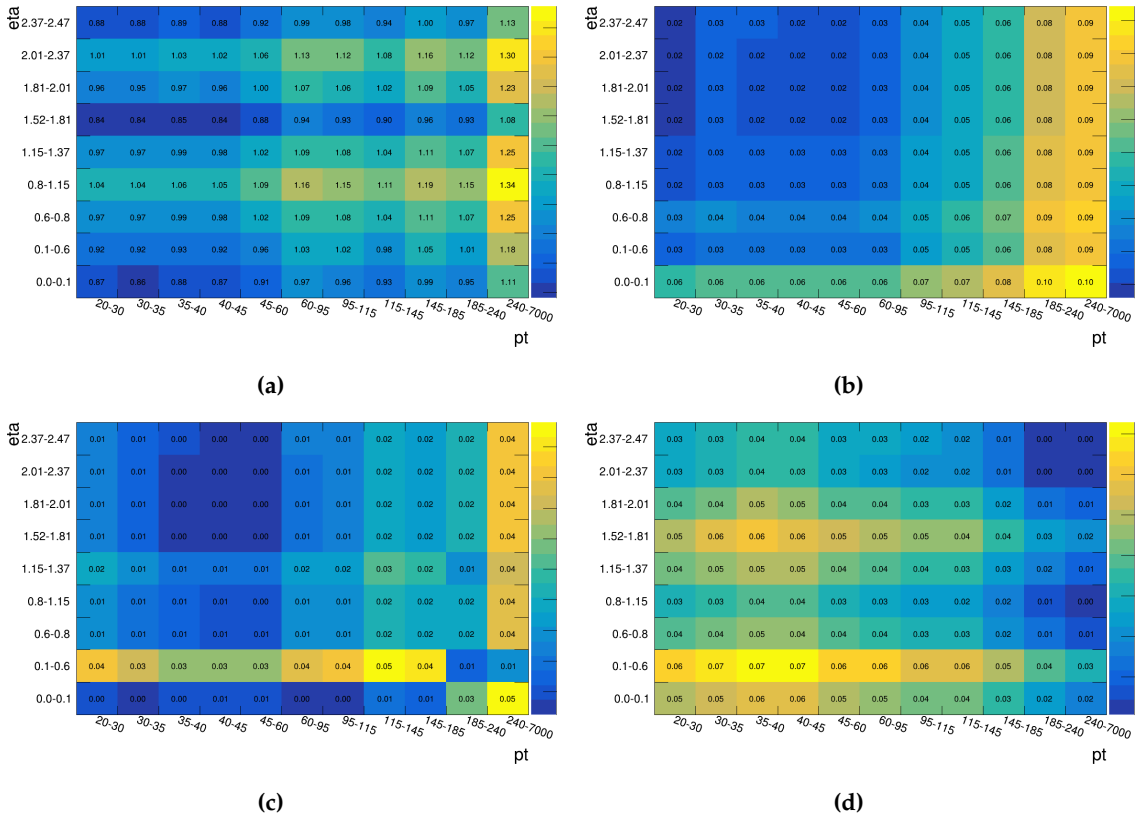

Figure B.6: Scale factor maps derived with Run 3 data taken in 2022-2023 and MC campaigns mc23a and mc23d for electrons passing `LooseLH` identification and `Tight_VarRad` isolation working point. Fine binning with 1D×1D parameterization is used to derive these (a) scale factors for Data/MC (b) statistical uncertainties (c) systematic uncertainties from sideband subtraction (d) systematic uncertainties from FSR subtraction.

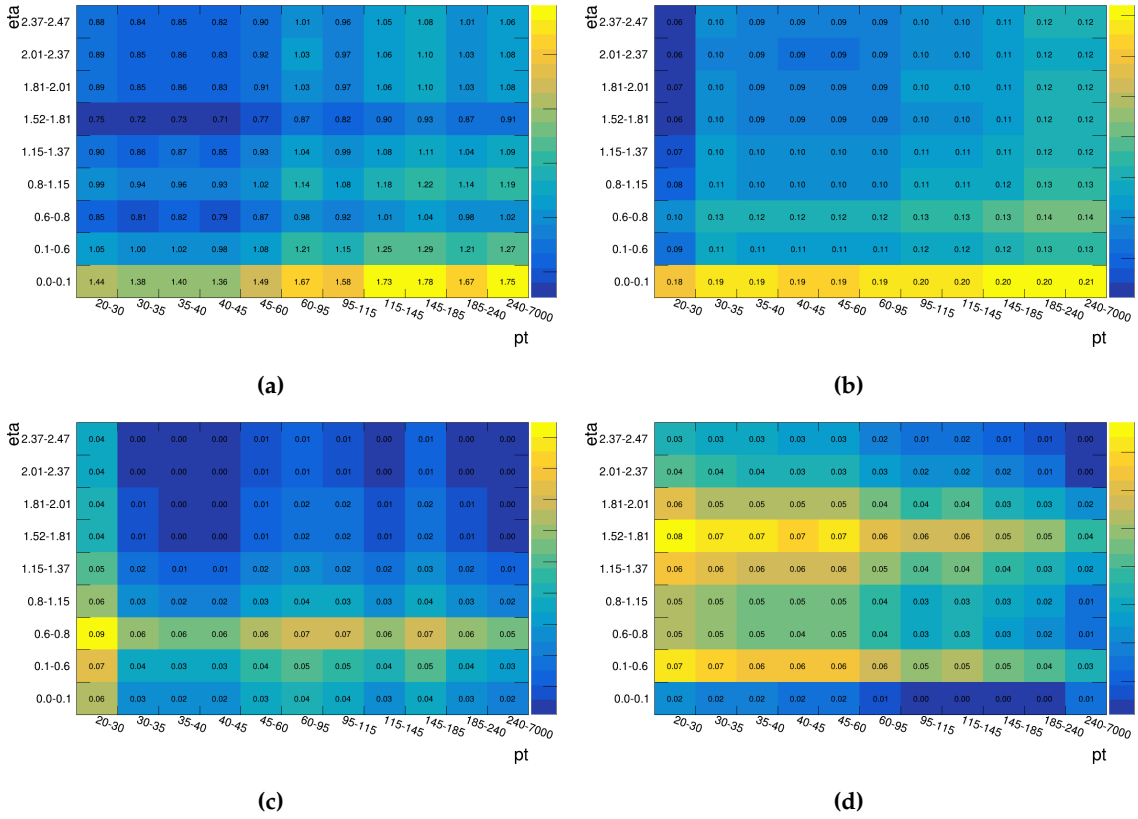

Figure B.7: Scale factor maps derived with Run 2 data taken in 2015-2018 and MC campaigns mc20a, mc20d and mc20e for electrons passing `LooseLH` identification and `Tight_VarRad` isolation working point along with ECIDS tool. Fine binning with 1D×1D parameterization is used to derive these (a) scale factors for Data/MC (b) statistical uncertainties (c) systematic uncertainties from sideband subtraction (d) systematic uncertainties from FSR subtraction.

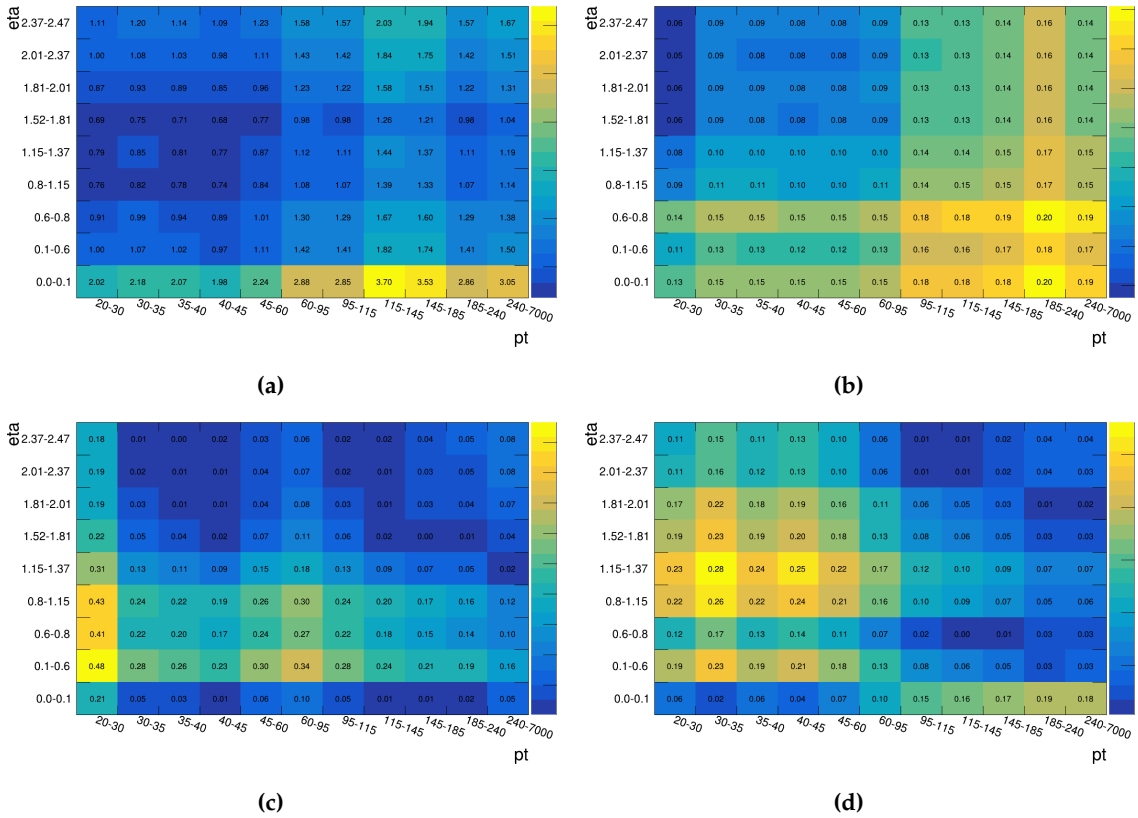

Figure B.8: Scale factor maps derived with RUn 2 data taken in 2015-2018 and MC campaigns mc20a, mc20d and mc20e for electrons passing `LooseDNN` identification with charge-flip rejection.. Fine binning with 1D×1D parameterization is used to derive these (a) scale factors for Data/MC (b) statistical uncertainties (c) systematic uncertainties from sideband subtraction (d) systematic uncertainties from FSR subtraction.

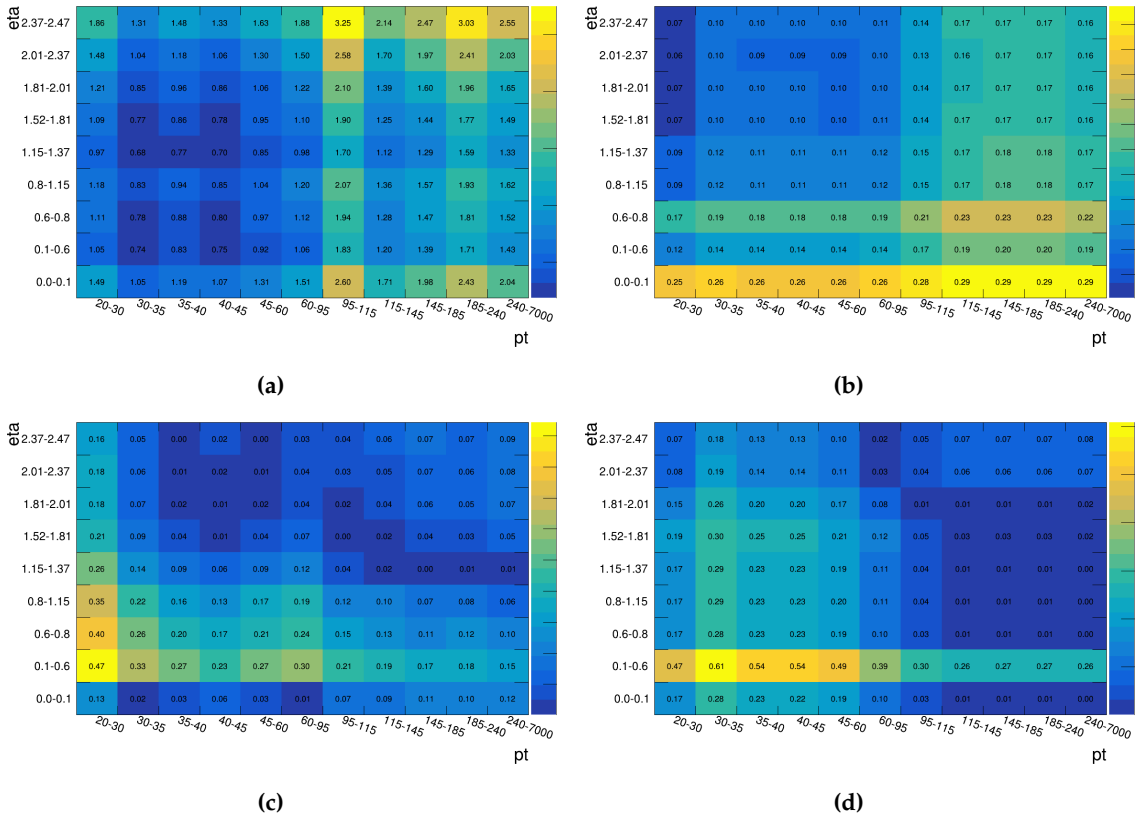

Figure B.9: Scale factor maps derived with Run 3 data taken in 2022-2023 and MC campaigns mc23a and mc23d for electrons passing `LooseDNN` identification with charge-flip rejection.. Fine binning with 1D×1D parameterization is used to derive these (a) scale factors for Data/MC (b) statistical uncertainties (c) systematic uncertainties from sideband subtraction (d) systematic uncertainties from FSR subtraction.

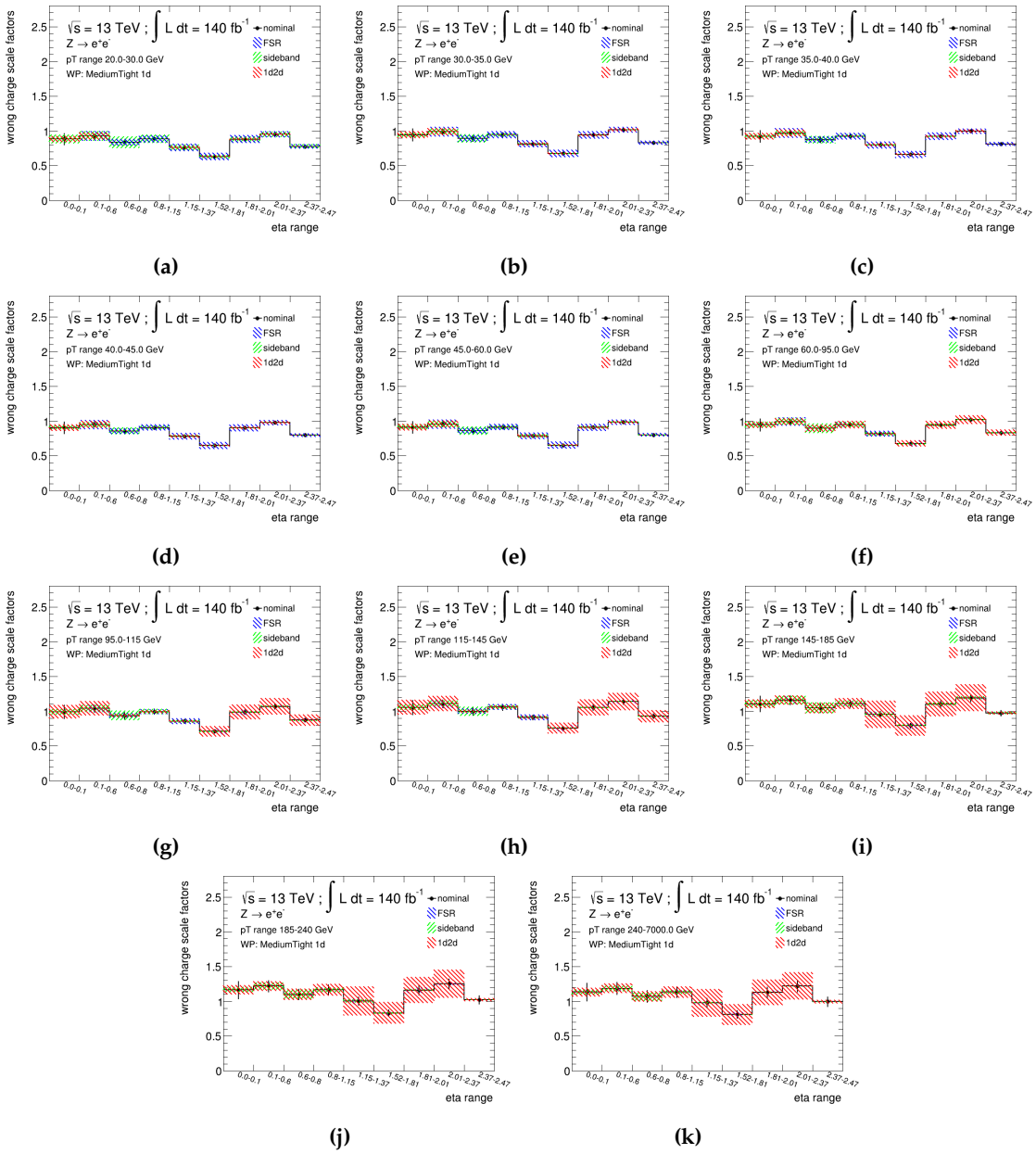

Figure B.10: Charge misID scale factors for incorrectly reconstructed charged electrons passing `MediumLH` identification and `Tight_VarRad` isolation working point. Scale factors are shown for full Run 2 data and corresponding systematic uncertainties from FSR, sideband subtraction and non closure from 1D×1D and 2D parameterization in various p_T slices calculated with the 1D×1D parameterization are also shown.

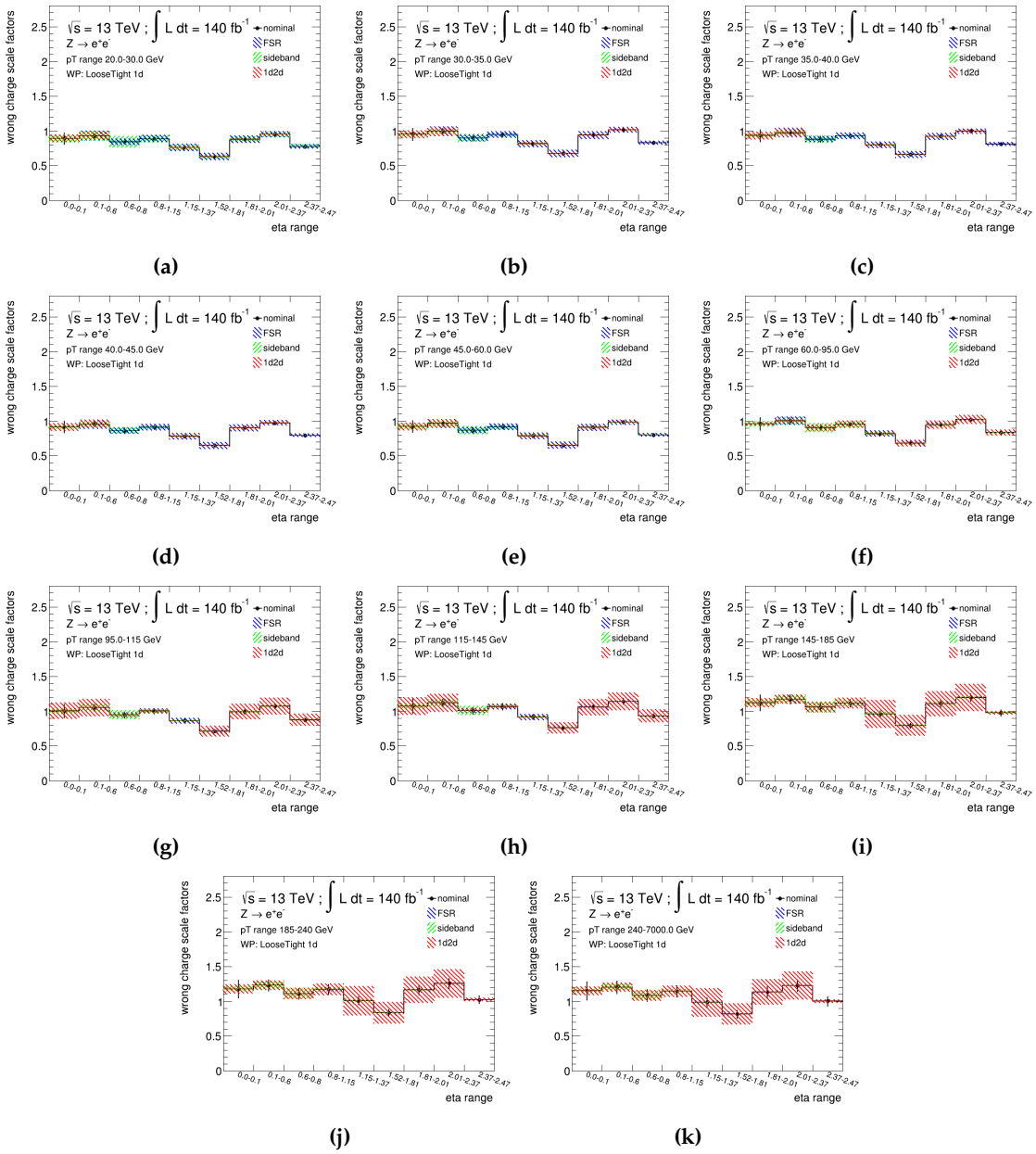

Figure B.11: Charge misID scale factors for incorrectly reconstructed charged electrons passing `LooseLH` identification and `Tight_VarRad` isolation working point . Scale factors are shown for full Run 2 data and corresponding systematic uncertainties from FSR, sideband subtraction and non closure from 1D×1D and 2D parameterization in various p_T slices calculated with the 1D×1D parameterization are also shown.